THE HONG KONG
POLYTECHNIC UNIVERSITY
香港理工大學
Pao Yue-kong Library
包玉剛圖書館

Copyright Undertaking

This thesis is protected by copyright, with all rights reserved.

By reading and using the thesis, the reader understands and agrees to the following terms:

1. The reader will abide by the rules and legal ordinances governing copyright regarding the use of the thesis.

2. The reader will use the thesis for the purpose of research or private study only and not for distribution or further reproduction or any other purpose.

3. The reader agrees to indemnify and hold the University harmless from and against any loss, damage, cost, liability or expenses arising from copyright infringement or unauthorized usage.

Pao Yue-kong Library, The Hong Kong Polytechnic University, Hung Hom, Kowloon, Hong Kong

http://www.lib.polyu.edu.hk

IMAGING AND DIAGNOSIS OF URBAN SUBSURFACE HAZARDS BY GROUND PENETRATING RADAR

XIANGHUAN LUO

PhD

The Hong Kong Polytechnic University

2020

The Hong Kong Polytechnic University

Department of Land Surveying and Geo-informatics

Imaging and Diagnosis of Urban Subsurface Hazards by Ground Penetrating Radar

Xianghuan Luo

A thesis submitted in partial fulfilment of the requirement for the degree of Doctor of Philosophy

August 2019

Certificate of Originality

I hereby declare that this thesis is my own work and that, to the best of my knowledge and belief, it reproduces no material previously published or written, nor material that has been accepted for the award of any other degree or diploma, except where due acknowledgement has been made in the text.

_____ (Signed)

_____ LUO Xianghuan _____ (Name of student)

I

Abstract

Due to the increasing city population, the demand for` water supplies, water discharge, energy and telecommunication, a city's underground is getting more complex (more utility types) and congested (higher density). However, without proper care, they are unavoidably ageing and create different sorts of problems, for example, ground subsidence caused by void formation initiated after a water leak from a pipe. Their conditions require an approach of proper imaging and health diagnosis for decision-making of rehabilitation or replacement scheme, as if the diagnostic process in a hospital would be conducted for human beings before any decision of surgery and medication. Without excavation, ground penetrating radar (GPR) is the most suitable means for imaging the ground truth in terms of (1) its 2D and 3D image representations close to ground truth, (2) efficiency of data capture, (3) fine resolution up to centimetre scale, and (4) its good match of depth ranging with the utilities' depths which are in the scale of meters. For such purpose, GPR depth/time slice (C-scan) at user-selected depths is the best representation. But to date, the process of constructing 3D C-scans is still subjective and mainly relies upon the operator's knowledge and experience. Biases from human judgements or survey setting are inevitable, and therefore doubts arise on the imaging and diagnostic purpose. The main achievement of this research is to establish a first of its kind, systematic and bias-free workflow for urban's underground diagnosis with GPR C-scans and pattern recognitions of B-scan radargrams based on forward and inverse methods. Also, the thesis contributed to the development of methods integrated with image processing algorithms for extracting spatial and temporal features (i.e. hazards) from GPR C-scans. The process imitates the decision-making process normally made by skilled professionals but in a semi-automatic and more robust fashion, especially when even the most skilled professionals would fall short of the ability to handle huge volume of GPR data.

This thesis contributed to the research and engineering/surveying community in the following four aspects imminently. Firstly, an object-oriented workflow for generalizing reliable C-scans was developed, with empirical thresholds/ranges of three identified and crucial parameters (profile spacing, slice thickness and interpolation algorithms). The workflow was validated after comparing C-scan images and reality through ground-truth of twenty-five carefully designed experiments conducted on concrete members, underground utilities/infrastructures and an archaeological site. Secondly, the GPR responses of air voids, the most important kind of hazard, were quantitatively analysed with five attachments (materials, size, thickness, etc.)

with numerical simulations and two experiments, one in the laboratory and one in the field. It was concluded that the ratios of void spread to the GPR footprints result in various GPR response patterns, and voids were only visible when the said ratio is larger than the factor of two to three. Thirdly, a workflow integrating the pyramid pattern recognition was developed to identify air voids from GPR data semi-automatically. The void recognition workflow was validated with a series of laboratory tests and site experiments. The true positive rate (i.e. identified voids do exist) of two validation-cases was sixty-five percent, and there was no omission (true negative and false negative) with the developed workflow. Lastly, with reliable C-scans and patterns of underground voids in the GPR data, the fourth aim achieved in this study was the development of a workflow to identify temporal changes from time-lapse GPR data with image change detection techniques. The workflow used K-means clustering to classify pixels into changed or unchanged. These four imminent contributions provide a gateway towards reliable and consistent imaging and diagnosis, and a basis of time-lapsed comparison with a well-established pattern recognition database. In short, this research establishes a health diagnostic approach for the urban underground. Human subjective interventions are reduced as much as possible in this developed approach. It is believed to trigger a start for establishing a full coverage health-record for underground utilities and associated hazards with GPR.

List of Publications

Journal Papers:

Luo, X. H., Lai, W. L., Chang, R. K., & Goodman, D. (2019). GPR imaging criteria. *Journal of Applied Geophysics, 165*, 37-48.

Luo, X. H., & Lai, W. L (2020). GPR pattern recognition of shallow subsurface air voids. *Tunnelling and Underground Space Technology*, *99*, 103355.

Luo, X. H. & Lai, W. L. (2020). Subsurface diagnosis with time-lapse GPR data, *IEEE Journal of Selected Topics in Applied Earth Observations and Remote Sensing*, 2151-1535.

Luo, X. H., Lai, W. L., & Giannopoulos, A. Forward modelling on GPR responses of subsurface air voids, *Tunnelling and Underground Space Technology*, under review

Conference proceedings:

Luo, X. H., Lai, W. L., & Chang, R. K., (2018) Development of a change-detection method on underground air void identification by time-lapse GPR 3D imaging. 17th International Conference on Ground Penetrating Radar (GPR). IEEE, 2018.

Acknowledgement

I would like to express my special appreciation and thanks to my chief supervisor Dr. Wallace Lai, for his continuous support for my PhD study. His patience, motivation, and professional knowledge led me through the whole journey of the research. Geophysics and GPR were once totally strange to me, Dr. Lai guides me from the fundamental concepts, organizing my research content, to writing this thesis. I could not have imagined having a better supervisor and mentor for my PhD study.

My gratefulness also goes to my co-supervisor Prof. Xiao-li Ding. He provided me insightful comments and encouragements when I was at the crossroads of research. His immense knowledge inspired me to widen my research from various perspectives.

I gratefully acknowledge Dr. Dean Goodman, who sets up the milestone of GPR imaging. With his help, I was "standing on the shoulders of giants". I also owe my thanks to Dr. Antonios Giannopoulos, who supervised me during my attachment program in Edinburgh, Britain, where I learned GPR numerical simulation in-depth. Their suggestions and advice make up the core of my research.

Many thanks to Mr. Ray Chang and Dr. Janet Sham, from whom I got precious supports. They taught me practical GPR processing, help me setting up experiments, and advise me when encountering confusions. Without they it would not be possible to conduct this research. Thanks go to Ms. Phoebe Wong, Ms. Bella Cheung, Mr. Fei Xie and Ms. Lydia Chiu who have proved themselves the loveliest groupmates ever. It was enjoyable to work with them. I am grateful to Dr. Bo Wu, the Board of Chair of my thesis examination, as well as Prof. Nicole Metje and Prof. Lung Sang Chan, the external examiners of this thesis, for their constructive comments and suggestions. Special gratitude goes to Dr. Craig Warren. He provided me constructive suggestions on making numerical simulations that closer to the reality. I am also grateful to Dr. Mick Atha, for his efforts in proofreading this thesis as well as my journal publications.

Last but not least, I would also like to thank my parents, for always believing in me and encouraging me during this challenging period. Thank my boyfriend for sticking by my side, even when I was sometimes irritable, and all my friends for accompanying me, cheering me up for enjoying my life.

Undertaking this PhD has been a truly life-changing experience, and it would not have been possible without the support and guidance from these people.

Table of Contents

List of Figures

XIII

List of Tables

Chapter 1 Introduction

1.1 Background

Modern cities are made up of a large number of infrastructural components, such as bridges, high-rise buildings, dense road networks, and complex underground utilities. The interweaving of old and new infrastructure dramatically facilitates the development of cities and brings significant benefits to society. However, the management of urban infrastructure is complicated, and the work of managing invisible underground utilities has proven to be especially demanding and costly. Without proper diagnosis and maintenance, ageing utilities can suffer from various modes of failures, bringing urban hazards such as land subsidence, the collapse of infrastructure, and flooding. They can cause not only financial loss but also causalities.

Conducting regular health checks for condition diagnosis on urban underground utilities is a relatively novel approach. Knowledge of medical imaging, geophysical and nondestructive survey techniques can provide sufficiently large-scale and detailed information without affecting the integrity of structures. Underground utilities and defects within them are invisible from the ground surface. Nondestructive testing (NDTs) or near surface geophysics (NSG) enables operators to see the unseen subsurface world without excavation. Among the multiple NDTs available, such as eddy-current, ultrasound, thermography, and visual inspection (CCTV), ground penetrating radar (GPR) has gained popularity for the following reasons: (1) high resolution; (2) offers effective data acquisition; and (3) sensitive to material properties (Lai et al., 2018a). GPR survey relies on the transmission and reflection of EM waves within a medium to detect and image the subsurface world. GPR has been used in numerous civil engineering applications: including locating small rebars in concrete (Bungey, 2004; Nojavan & Yuan, 2006); detecting underground utilities (Hao et al., 2012); reconstructing buried stratigraphy (Gerber et al., 2007); and discovering archaeological remains (Lai et al., 2018a; Nuzzo et al., 2002).

There is a large volume of published research demonstrating the efficiency and effectiveness of GPR surveys. In parallel with the continuous growth of urban areas, increasing demand for large-scale periodic subsurface surveys has also been witnessed. Unfortunately, although it is more effective than other NDTs, GPR is still not able to provide full coverage subsurface surveys, while GPR data interpretation is time-consuming and labour-intensive. GPR is an

expert-dependent technique because interpreting GPR signals requires the operator to have sufficient knowledge and experience in order to do so. Currently, 3D GPR representation is increasingly being adopted, because it can provide an intuitive visualization of the subsurface, which is much clearer than the 'messy' 2D wave signal data. But the technique of 3D GPR survey is still immature, and discrepancies are inevitable between 3D GPR images captured at different times in the same place but modelled by different operators using different equipment. Moreover, it is hard to test whether the 3D GPR images are reliable since excavation 'ground-truthing' is not always desirable.

Having briefly introduced the role of GPR in underground utility surveying, the thesis structure will be outlined next. This thesis is divided into four stages as detailed below.

Following a general introduction to the principles and application of GPR in underground utility detection (Chapter 2), in stage 1 (Chapter 3) the relationships between GPR responses and subsurface objects are quantitatively analysed. This initial research establishes a standardised and unbiased workflow for 3D GPR data processing, based upon the relationship between GPR responses and the characteristics of objects. The workflow is object-oriented and can provide guidances for obtaining unbiased and reliable 3D GPR representations. The invisible subsurface world can be reconstructed as semantic models. The research community and practitioners will benefit from the improvements in GPR imaging accuracy. In particular, if the sizes of target objects are known, the workflow specifies the suitable range for each imaging parameter, thus removing the need for multiple attempts at optimal imaging using different parameters.

In stage 2 (Chapter 4), the typical GPR responses of urban subsurface hazards are studied and summarized. Specifically, the mechanisms behind, the morphology of GPR radargram and C-scans of air voids are investigated. As land subsidence often occurs on roads, the effects of road structures on the GPR response of voids are quantitatively studied. By combining numerical simulations and real GPR data, a picture of air voids under roads is created. With prior knowledge of the appearance of air voids in GPR data, specific GPR responses in both 2D and 3D GPR representations can be targeted and detected. Stage 3 (Chapter 5) explores the possibilities of applying pattern recognition techniques to identify the GPR responses of urban subsurface defects automatically. Thanks to the development of computer visualisation techniques, a number of methods are available for automatically detecting particular patterns

within data. Operators are thus liberated from the large volume of work typically needed in GPR data interpretation.

In stage 4 (Chapter 6), armed with a standard workflow for 3D GPR imaging, a longitudinal and time-lapse "medical record" of the subsurface world can be reconstructed. By comparing 3D GPR images obtained at different times, changes happening in the subsurface world can be observed, and these changes may be related to potential defects in buried urban infrastructure. This research explores the possibility of applying change detection techniques to time-based GPR images produced for periodic "health checks". Any detected anomalies can then be further verified by pattern recognition techniques. Since only those areas showing change need to be assessed, and unchanged areas are omitted, the workload of the GPR survey can be significantly reduced.

In summary, this research establishes a diagnostic approach for subsurface defects in the urban areas using the spatial and temporal characteristics of GPR. It moves from quantifying GPR responses to subsurface targets to standardizing GPR data processing and image construction, and then towards applications of change detection using time-based GPR data. Human subjective interventions are eliminated as much as possible from the system. The diagnostic approach facilitates more effective GPR surveys, and makes full coverage GPR surveys feasible.

This thesis consists of six chapters, based upon the four objectives listed below. Chapter 1 gives justifications concerning the scope and aims of the research, and outlines the objectives and methodology of this research. Chapter 2 provides an overview of the fundamental principles of GPR as well as the various techniques applied. Chapter 3 discusses the outcome of objective 1, which is a standardized GPR imaging workflow, supported with empirical experiments. Chapter 4 explains the results of objective 2 in terms of a database of GPR responses or 'fingerprints' for some typical subsurface structures, with a focus on air voids under road structures. Chapter 5 describes the details of objective 3; namely, a workflow of semi-automatically identified GPR responses to subsurface voids is introduced and explained with validation experiments. Chapter 6 demonstrates the attempt of objective 4 through a workflow for change detection from time-lapse GPR data. Finally, chapter 7 summarizes the observations made during the research, and outlines the research significances as well the challenges of conducting GPR surveys for urban defect diagnosis.

1.2 Research objectives

As discussed in chapter 1.1, the research aims to establish a system for subsurface defects diagnosis with GPR. The diagnosis system should be time and cost efficient enough for city-scale survey. The research consists of four parts reflecting the following objectives:

(1) Modify GPR 2D process flow and build a 3D C-scan imaging workflow based on an understanding of object characteristics and signal/image processing principles;

(2) Establish and validate a GPR 'fingerprint' database and processing flow for common subsurface objects based on objective (1), through forward modelling and empirical experiments;

(3) Develop a workflow for semi-automatic pattern recognition of shallow subsurface voids based on the results of objectives 1 and 2;

(4) Develop a GPR-based change-detection diagnostic workflow for temporal diagnosis of subsurface changes.

1.3 Research methodology

1.3.1 Research resources

The successful operation of the research depends on the availableness of research resources. In this study, most of the laboratory tests are conducted in the underground utility survey laboratory in The Hong Kong Polytechnic University. In the laboratory, there is a 5 m long, 3 wide and 1m deep platform. Multiple utilities are buried in the platform, including freshwater pipes, salt water pipes, gas pipe and power cables are buried by soil. The indoor and controllable environment serves to imitate the subsurface environment of urban cities in the real world.

Site experiments are conducted in Hong Kong, in order to validate that the research approach is suitable for developed cities. Specific research areas are selected based on each research objective, as well as the project permission, since subsurface surveys always involve in excavations or traffic obstacles.

In terms of instrumentation, it involves GPR equipment in the laboratory, they are 250MHz sensor & software; GSSI with 400MHz, 900MHz, 1GHz, 1.6GHz and 2GHz frequencies antenna; IDS 200&600 MHz dual frequencies. Moreover, available software is comprehensive

that includes GPR processing software – Reflexw, GPRSlice and gprMax; mathematic software – MATLAB; as well as computer-aided design software – Autodesk and ArcGIS.

The sufficient research resources enable me to carry out both forward studies and validation studies, under various environments and multiple survey settings.

1.3.2 Combine forward and backward methods

With adequate research resources, this research is capable of both forward modelling and inverse modelling , and GPR simulation is used specifically as an integral part of the forward modelling. Because the complex subsurface world is not always accessible, it can be challenging to acquire GPR data on expected real-world situations. However, sufficiently comprehensive data are required in order to quantify the GPR responses under a range of conditions. Numerical simulation is adopted to construct models that can approximate real-world situations. Controlled experiments provide another type of forward modelling and are conducted in the laboratory or research sites to imitate the actual conditions as much as possible. The forward modelling is mainly involved in quantifying the relationship between GPR reflections and subsurface objects – the major component in the 1st and the 2nd objectives.

Inverse modelling is opposite to forward modelling, in that an inverse problem in science involves the process of calculating dependent factors from a set of observations that produced them. In this thesis, it aimed at quantifying the GPR response for each feature and then validating the research outputs. Having acquired GPR data, representative models that correlate the GPR observations with actual subsurface conditions are established. The subsurface environment can thus be depicted by analysing the GPR responses. The inverse modelling is used in validating the approaches, which refers to the 3rd and 4th objectives.

The research integrates both virtual numerical simulations and practical surveying observations. Forward and inverse modelling complement each other, as shown in Figure 1-1. In this way, the interaction between GPR and the subsurface world can be quantified.
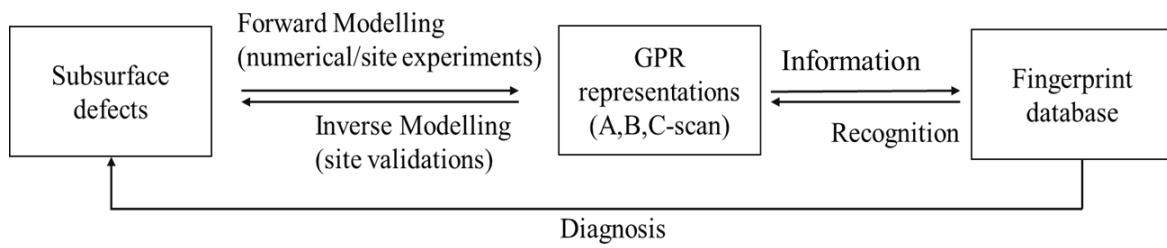
Figure 1-1 An illustration of the research methodology of this thesis

1.3.3 Workflows

Following the general research methodology (Figure 1-1), several workflows are established to achieve the research aim, which makes each workflow a protocol for an objective.

Workflows are tailored for survey data in city-scale. The image processing techniques, like the pattern recognition techniques and the change detection techniques, are explored and adapted to improve the efficiency of diagnosis. The selections of suitable algorithms for each technique are based on the review of the literature (to be discussed in Chapter 2). The workflows integrate the specific imaging processing techniques, automate the diagnosis with GPR from the data collection, to data processing and analysis.

Chapter 2 GPR reviews

Before striving to the research aim, its feasibility from the technical and theoretical perspectives need to be discussed in advance. This chapter reviews the fundamental theories and principles of GPR. Various applications of GPR survey, including the techniques applied in this thesis, are introduced in this chapter.

2.1 Electromagnetic waves

During a GPR survey, the radar signal – a pulse of the electromagnetic (EM) wave, is emitted from a transmitting antenna and travels downward through the host material until it reaches an object that has different electrical properties from the surrounding material. Part of the signal is then scattered by the object and is detected by a receiving antenna, while part of its energy continues to travel downwards. Figure 2-1 is a typical illustration of the common offset GPR survey.
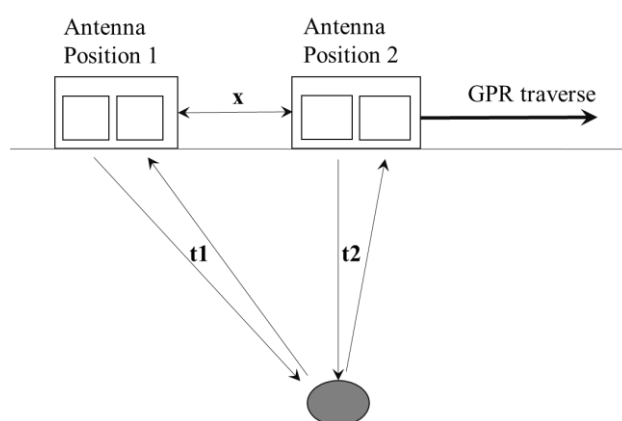
Figure 2-1 Hyperbolic reflection from common offset GPR, t_1 and t_2 are the GPR wave travel time at antenna position 1 and 2, respectively; while x is the moving distance of the antenna. (Lai et al., 2016a)

a. Wave properties

Maxwell's equations, as shown in Equations [2.1-2.4], mathematically describe EM physics and the constitutive relationships that quantify material properties (Annan, 2002; Annan, 2004; Jol, 2009).

$$\overline{\nabla} \times \overline{E} = -\frac{\partial \overline{B}}{\partial t} \qquad [2.1]$$

$$\overline{\nabla} \times \overline{H} = \overline{J} + \frac{\partial \overline{D}}{\partial t} \qquad\qquad\qquad [2.2]$$

$$\overline{\nabla} \cdot \overline{D} = q \qquad\qquad\qquad\qquad [2.3]$$

$$\overline{\nabla} \cdot \overline{B} = 0 \qquad\qquad\qquad\qquad [2.4]$$

In the above equations, $\overline{E}$ is the electric field strength vector; $\overline{B}$ is the magnetic flux density vector; $\overline{D}$ is the electric displacement vector; $\overline{H}$ is the magnetic field intensity; q is the electric charge density and $\overline{J}$ is the electric current density vector.

The wave propagation velocity, attenuation rate, and electromagnetic impedance are three crucial EM wave field properties. The electromagnetic impedance refers to the ratio between a medium's electric field and magnetic field, and it is determined by the medium's properties (Davis & Annan, 1989; Jol, 2009; Benedetto & Pajewski, 2015). At high frequencies, the electromagnetic fields propagate as waves with a relatively uniform travel velocity and attenuation rate through the medium. It is observed that there is always a tendency for permittivity to decrease with frequency and conductivity to increase with frequency (Lai et al., 2014). At low frequencies, the electromagnetic fields diffuse into the material. In this case, the wave is dispersed because its frequency components travel with different velocities and are attenuated at different rates based on their contrasting polarization mechanisms (Annan, 2004; Davis & Annan, 1989; Jol, 2009). Therefore, the actual frequency of the reflected GPR signal may be different from the antenna frequency: and hence should be measured. Few measurement methods are available for transforming the signal from the time domain to the frequency domain, among which Fourier series, Fourier transform, Laplace transform, Z transforms, and wavelet transform are widely used (Boashash, 2015; Broughton & Bryan). Wavelet transform is applied in this research for its convenience for data compression, the multi-resolution advantage for both high- and low-frequency signals, and especially suitable in the image analysis (Broughton & Bryan).

In terms of the permittivity, its response tends to manifest as a "plateau", and within the plateau's range, the wave velocity and attenuation rate do not disperse significantly across a range of GPR frequencies. It is because at low frequencies, wave properties depend on *2πf* (*f* is the frequency), which is indicative of diffusive field behaviour, while at high frequencies, the properties become frequency-independent (Jol, 2009). The transition from diffusion to propagation behaviour occurs when the electric currents change from conduction-dominant to displacement-current dominant behaviour, thus the "plateau" occur (Jol, 2009). The wave properties for simple media are most easily expressed if a sinusoidal time variation is assumed.

Besides, when using high-frequency GPR, electrical properties are more likely to be affected by the presence of free water in the pores and fractures of a medium, because water tends to absorb more energy as the frequency increases from 500MHz to 10 GHz (Davis & Annan, 1989). Beyond the plateau, GPR attenuation increases significantly and may result in a failure to detect deeply buried objects. As shown in Figure.2-2.c, the dielectric properties of a material are frequency dependent. At GPR frequencies of 10^6 through 10^9, wave behaviour is not dispersive (to be discussed in Chapter 2.1.b). Therefore, for urban underground survey and mapping, which needs to consider the plateau and the need for high resolution imaging, the frequencies applied usually range from 100-3000MHz. Figure 2-2 illustrates the GPR plateau.

a

b

c
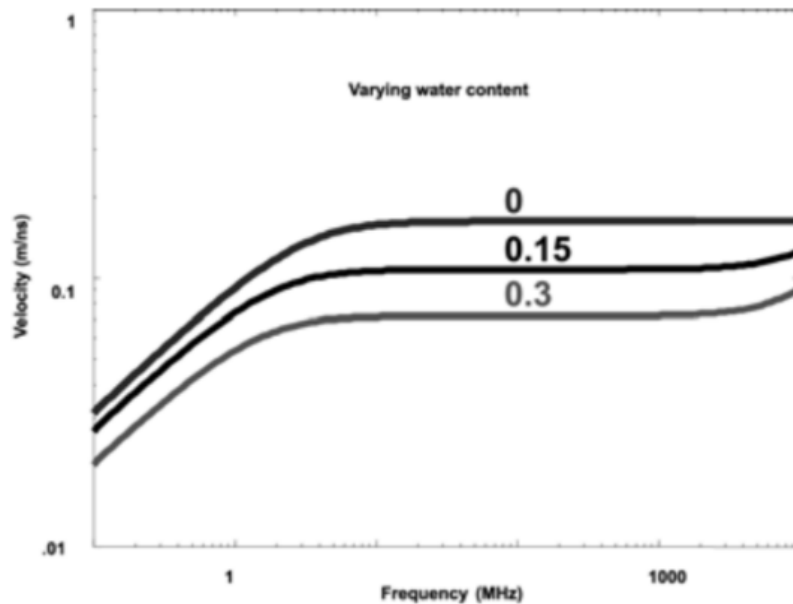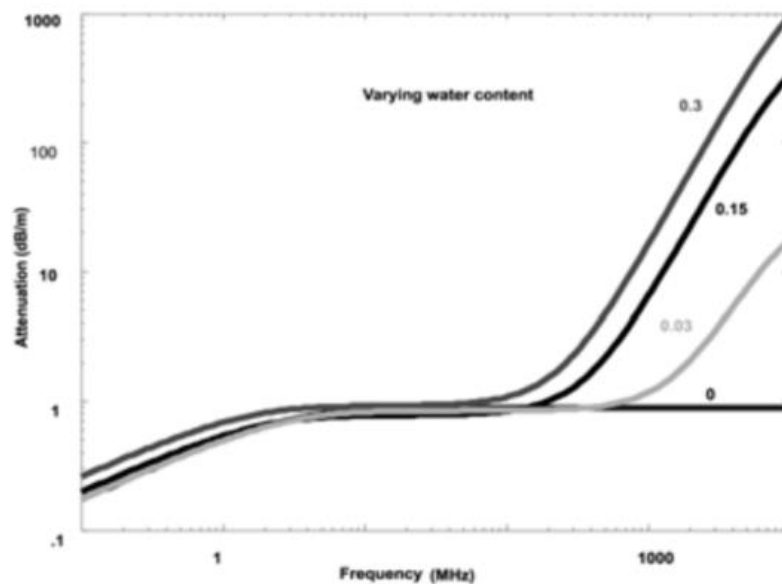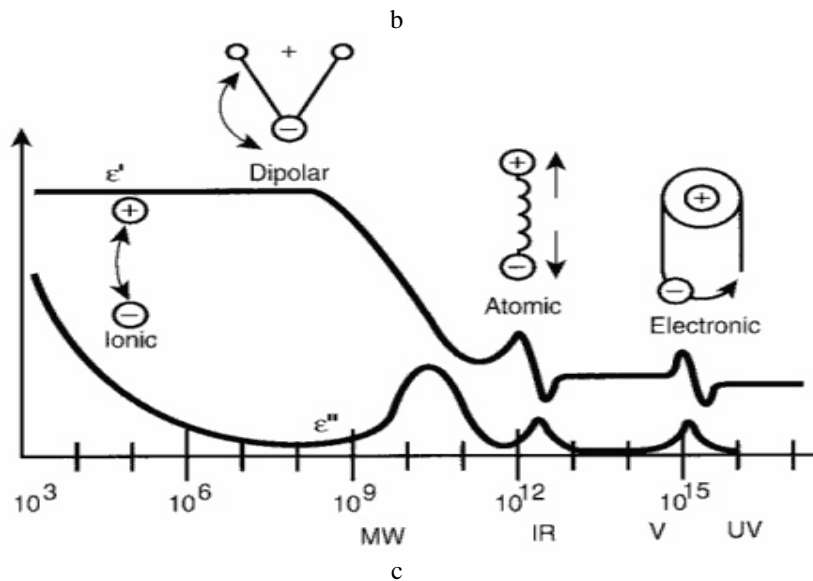
Figure 2-2 Illustration on GPR plateau of (a) wave velocity and (b) attenuation (c) dielectric permittivity spectrum over a wide range of frequencies, for real (top curve) and "imaginary" (bottom curve) components (Annan, 2004)

b. Interactions between GPR and materials

The EM wave fields consist of the coupled electric field (E) and magnetic (H) field. The electrical properties of a material are dominant factors controlling GPR responses, while magnetic properties have a relatively weaker influence. In studies of GPR applications, the focuses are upon the important EM wave field properties of phase velocity v, attenuation α, and electromagnetic impedance Z. The behaviour of these wave properties for a single material is determined by the relative dielectric permittivity, conductivity and magnetic permeability of the medium.

Snell's law (Equation [2.5]) describes the refraction and reflection of EM waves across different materials, and the reflection of EM waves is caused by materials that have different electrical properties. Furthermore, the travel velocity of EM waves is determined primarily by the permittivity of the material, as described in Equation [2.6]. The relationship between wave velocity and material properties is of crucial importance in GPR surveys. The real part of the permittivity (ε) of a material, which is mainly determined by its water content, is considered in EM wave velocity estimation in this research. The ratio of ε of a material to that of a vacuum, which is known as the relative permittivity or dielectric constant (K), is determined by the following equations:

$$\frac{\sin \theta_1}{v_1} = \frac{\sin \theta_2}{v_2}$$

[2.5]

10

$$v = \frac{c}{\sqrt{K}}$$
[2.6]

where θ_1 and θ_2 are respectively the angle of incidence and refraction, and c is the wave velocity in free space, which is approximately 0.2998m/ns.

The permittivity is in fact a complex value. It is a measure of the extent to which charge distribution can be distorted or polarized by an applied E field in a material, and it is frequency-dependent. The imaginary part is related to the resistivity, while the real part is the capacitive response. At different frequencies, polarization occurs at different scales: at very high frequencies, only subatomic particles can be polarized. At GPR frequencies, re-orientation of dipolar molecules is the largest contribution, hence the effect of water is important in changing the velocity of EM waves propagating in a material. The behaviour of the real part and the imaginary part is shown in Figure 2-2.c. Values are relatively constant, and the imaginary part is very small for GPR frequencies of 10^6 through 10^9, ensuring that the wave behaviour is as dispersive as other polarization mechanisms.

In the research of GPR application, the conductivity of a medium can be considered as a constant with units of Farads/m (Annan, 2004). Within a depth range less than 2m in cities, the soil texture is mostly sandy, giving low conductivity in general. Besides, attenuation of GPR waves at the frequency in urban applications is small, rather constant because it is within the plateau, as shown in Figure. 2-2. According to Ohm's law, conductivity and resistivity are related to one another, and the conductivity determines the attenuation rate of EM waves. Attenuation dictates how deep the EM waves can reach and be reflected. When EM waves penetrate through lossy material, the wave amplitude decreases gradually. The attenuation rate increases as both frequency and conductivity increase. The electrical properties of some widely used materials in urban infrastructure are shown in Table 2-1.

Table 2-1 Approximate Electromagnetic Properties of Various Materials (ASTM D6432-11, 2011)

Material	Relative Permittivity ε'	Wave velocities (m/ns)	Conductivity (mS/m)
Air	1	0.3	0
Fresh water	81	0.033	0.10 – 30
Sea water	70	0.033	400
Sand (dry)	4-6	0.15-0.12	0.0001 – 1
Sand (saturated)	25	0.055	0.1 – 1
Silt (saturated)	10	0.095	1 – 10
Clay (saturated)	8-12	0.106-0.087	100 – 1000
Dry sandy coastal land	10	0.095	2
Fresh water ice	4	0.15	0.1 – 10
Permafrost	4-8	0.15-0.106	0.01 – 10
Granite (dry)	5	0.134	0.00001
Concrete	5-10	0.134-0.095	
Asphalt	3-5	0.173-0.134	
Sea ice	4-12	0.15-0.087	
PVC, epoxy, polyesters vinyl, rubber	3	0.173	

c. Two-way travel time

By measuring the wave propagation time and the wave travel speed, the wave travel distance can be estimated. As shown in Figure 2-1, as an EM wave travels downwards and is reflected by an object, the travel distance of the EM wave is approximately two times the depth of the object. The travel distance is therefore called the two-way-travel time, and is described by Equation [2.7]:

$$d = \frac{vt}{2} \qquad [2.7]$$

where d is the depth of the buried reflector. v is wave velocity and t denotes the travel time.

The velocity estimation is one of the most important processing in GPR data interpretation, not only because it directly determines the depth of the detected objects, but also the wave velocity is a crucial factor in other processes like migration and inversion. Many factors, like homogeneousness of the host material; the selection of velocity expression model; the GPR profile orientation and the geometry of reflectors, in a GPR survey affect the accuracy of wave velocity estimation. Recently, many researches made progress in correcting and amending the influence of these factors. Namely but not the least, Sham & Lai (2016) and Lai et al. (2016b) took the object diameter into consideration when estimating wave velocity. Xie et al. (2018) introduced the effect of distance and angle between the GPR device and a linear object in the

wave velocity estimation. With these developments, the accuracy of the estimation of wave velocity can be improved significantly.

2.2 Finite difference time domain modelling of GPR

To establish a diagnostic system for subsurface defects, the relationship between GPR measurements and subsurface defects must be determined. The numerical simulation is an alternative way to model GPR reflections under a controlled environment. Over decades of development, there are numerous methods for computational electromagnetics, among which, methods of moment (MoM) (Harrington, 1993), finite element method (FEM), and finite-difference time-domain (FDTD) are the most popular (Davidson, 2010). Their characteristics and advantages are compared in Table 2-2.

Table 2-2 Comparison of a few numerical simulation methods

Method	Equation type	Domain	Radiation condition	Wide band	PEC only	Homogenous penetrable	Inhomogeneous penetrable
Method of Moment (MoM)	Integral	Frequency	Yes	Ok	Good	Good	Not optimal
Finite Element Method (FEM)	Differential	Frequency	No	Ok	Not optimal	Good	Good
FDTD	Differential	Time	No	Good	Not optimal	Good	Good

The MoM requires a calculation of only boundary values, rather than values throughout the space, it is significantly more efficient in terms of computational resources for problems with a small surface/volume ratio. Conceptually, it works by constructing a "mesh" over the modelled surface (Harrington, 1993). But MoM does not handle electromagnetic penetrable material well because it does not scale with frequency. The FEM is very expensive and hardly employed with home-built code. It is a preferred method for simulation of microwave devices (Davidson, 2010).

The FDTD is a versatile modelling technique that can be used to solve Maxwell's equations. Thus, it is a simple full-wave technique used to solve problems in electromagnetics. The FDTD

method employs finite differences as approximations for both the spatial and temporal derivatives that appear in Maxwell's equations; namely, Ampere's and Faraday's laws (Schneider, 2010), thus E (electric) and H (magnetic) fields are modelled directly, no conversions must be made – it is especially suitable for simulating GPR wave propagation. The FDTD links the nature of the movement of the electromagnetic field to the host media. The FDTD allows the user to specify the material at all points within the computational domain, so that it is appropriate in the subsurface modelling. However, FDTD also falls short of demand of very high computational power, i.e.: the computational domain can become excessively large because of fine grids. It is not possible to determine unique values for permittivity and permeability at a material interface, but this is not a severe issue in pattern recognition because the size of the grid for the database is not as large as a city-scale field survey. Also for FDTD, artificial boundaries are required to be inserted for defining the model domain in FDTD simulations. There are a few researches on absorbing boundaries providing mature solutions (Davidson, 2010; Giannopoulos, 2005).

Therefore, FDTD method is suitable for observing the GPR responses produced by various urban subsurface hazards. As discussed in Chapter 2.1 (Equation 2.1-2.4), Maxwell's equations are fundamental to the description of EM waves. By rewriting Equations [2.1-2.4], we have Equations [2.8-2.9]:

$$\mu \frac{\partial H_y}{\partial t} = \frac{\partial E_z}{\partial x} \qquad [2.8]$$

$$\epsilon \frac{\partial E_z}{\partial t} = \frac{\partial H_y}{\partial x} \qquad [2.9]$$

where H denotes the magnetic field in the y direction, and E is the electric field in x direction, t is a time step, μ is the relative permeability and ϵ is the relative permittivity.

The Taylor series of expansions of the function f(x) expanded about the point x_0 with an offset of $\pm\delta/2$ can be expressed as Equations [2.10-2.11].

$$f\left(x_0 + \frac{\delta}{2}\right) = f(x_0) + \frac{\delta}{2}f'(x_0) + \frac{1}{2!}\left(\frac{\delta}{2}\right)^2 f''(x_0) + \frac{1}{3!}\left(\frac{\delta}{2}\right)^3 f'''(x_0) + \cdots \qquad [2.10]$$

$$f\left(x_0 - \frac{\delta}{2}\right) = f(x_0) - \frac{\delta}{2}f'(x_0) + \frac{1}{2!}\left(\frac{\delta}{2}\right)^2 f''(x_0) - \frac{1}{3!}\left(\frac{\delta}{2}\right)^3 f'''(x_0) + \cdots \qquad [2.11]$$

If δ is sufficiently small, a reasonable approximation to the derivative may be obtained by neglecting the remainder of the equations. Thus, the central-difference approximation is given by Equation [2.12].

$$\frac{df(x)}{dx}\bigg|_{} \approx \frac{f\left(x_0 + \frac{\delta}{2}\right) - f\left(x_0 - \frac{\delta}{2}\right)}{\delta} \tag{2.12}$$

When the function is sampled at the neighbouring points $x_0 + \frac{\delta}{2}$ and $x_0 - \frac{\delta}{2}$, and if the limit δ is near zero, then the approximation becomes exact. The FDTD algorithm was first proposed by Yee (1966) and he employed second-order central differences as per [2.12]. The algorithm replaces all the derivatives in Ampere's and Faraday's laws with finite differences. It discretizes space and time so that the electrical and magnetic fields are staggered in both space and time. Then, by solving the resulting differential equation, the "update equations", which denote the unknown future fields, are obtained from the known past fields (Warren et al., 2016).

Therefore, the future electrical field can be modelled based upon past magnetic fields, and vice versa. By imagining a one-dimensional space where both E and H exist, the time domain space is discretized by a space step Δx and a time step Δt, as illustrated in Figure 2-3.
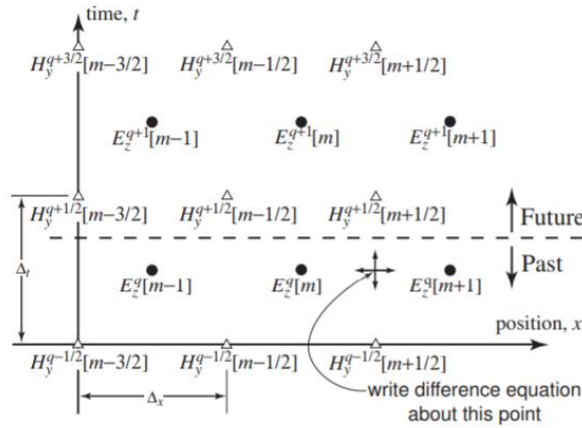
Figure 2-3 Illustration of one-dimensional EM field in FDTD modelling (Schneider, 2010). Remarks: The index m corresponds to the spatial step, effectively the spatial location, while the index q corresponds to the temporal step.

At the specific position $\left(\left(m + \frac{1}{2}\right)\Delta x, q\Delta t\right)$, indicated by the black arrow in Figure 2.3, the solution of Equations [2.8-2.9], [2.13-2.14] is obtained as follows.

$$\mu \frac{\partial H_y}{\partial t}\bigg|_{\left(m+\frac{1}{2}\right)\Delta x, q\Delta t} = \frac{\partial E_z}{\partial x}\bigg|_{\left(m+\frac{1}{2}\right)\Delta x, q\Delta t} \tag{2.13}$$

$$\epsilon \frac{\partial E_z}{\partial t}\bigg|_{\left(m+\frac{1}{2}\right)\Delta x, q\Delta t} = \frac{\partial H_y}{\partial x}\bigg|_{\left(m+\frac{1}{2}\right)\Delta x, q\Delta t} \tag{2.14}$$

When implementing the FDTD method, the temporal derivative on the left is replaced with a finite difference involving $E_z^{q+1}[m]$ and $E_z^q[m]$. Similarly, the right part of Equation [2.13] is

replaced by $H_y^{q+\frac{1}{2}}[m+\frac{1}{2}]$ and $H_y^{q+\frac{1}{2}}[m-\frac{1}{2}]$. Thus, the updated E and H are as shown in Equations [2.15] and [2.16].

$$H_y^{q+\frac{1}{2}}\left[m+\frac{1}{2}\right] = H_y^{q-\frac{1}{2}}\left[m-\frac{1}{2}\right] + \frac{\Delta t}{\mu \Delta x}(E_z^q[m+1] - E_z^q[m]) \qquad [2.15]$$

$$E_z^q[m+1] = E_z^q[m] + \frac{\Delta t}{\epsilon \Delta x}(H_y^{q+\frac{1}{2}}\left[m+\frac{1}{2}\right] - H_y^{q+\frac{1}{2}}\left[m-\frac{1}{2}\right]) \qquad [2.16]$$

The basic principles of FDTD modelling of EM waves are as detailed above. However, the FDTD method can be expanded to multi-dimension modelling, in terms of a single spatial dimension where the electrical and magnetic fields are offset a half spatial step from each other.

When performing the FDTD simulation, equations are discretized in both space and time in order to construct each FDTD cell. Hence the number of iterations determines the FDTD resolution of a given time window. It can be observed from the above equations that the step sizes in 3D – Δx, Δy, Δz and Δt – are correlative with each other. To ensure that the simulation runs stably, the CFL condition (as per Equation 2.17), named after the initials of Courant, Freidrichs and Lewy (Courant et al. 1928), has to be met:

$$\Delta t \leq \frac{1}{c\sqrt{\frac{1}{(\Delta x)^2} + \frac{1}{(\Delta y)^2} + \frac{1}{(\Delta z)^2}}} \qquad [2.17]$$

where c is the speed of light. Hence Δt is constrained by the values of Δx, Δy and Δz.

A rule-of-thumb is that the discretization step should be at least ten times smaller than the smallest wavelength of the propagating electromagnetic fields, otherwise unexpected dispersion may occur. Other factors, such as energy sources, field boundaries, and lossy materials have been well discussed in the literature (Hastings et al., 1995; Hastings et al., 1996; Schneider, 2010; Warren et al., 2016; Yee, 1966).

2.3 Remote sensing vs near-surface geophysics (NSG)/ non-destructive testing (NDT)

With either GPR measurements or numerical simulations, images can be constructed for further data processing and interpretation. Since imaging is the major means of representation (will be discussed in Chapter 2.4) in the diagnosis of the underground invisible void, image processing techniques are therefore the core of this study. In view of the similarity of the imaging processing approach, the experience of traditional remote sensing and near-surface geophysics can be referenced.

The principle of remote sensing is to acquire large volumes of information about an object or a phenomenon without making physical contact with it, supplemented and validated by on-site observations. From the perspective of civil engineers, geophysicist, remote sensing refers explicitly to sensing from aerial or terrestrial sensors, that the target of sensing is an observation on the Earth surface. Non-destructive testing (NDTs) is used for imaging the subsurface elements of urban infrastructure without the use of excavations. Even though their targets and scales of sensing are different, remote sensing, NSG (longer wavelength in the scale of m) and NDTs (shorter wavelength in the scale of few cm) share a common logic, in which they both acquire information about a target from a certain distance away rather than through direct contact. In both remote sensing and NSG/NDTs, variations in the target's characteristics, such as physical and chemical properties, geometry, position, and so on, would cause differences in the sensors' responses to it.

Before applying proper filters, the raw signals are disordered and hard to be interpreted. The effects of the phase shift, the signal attenuation along propagation, noises due to scattering in Mie type (wavelength comparable to the size of the general buried object), and coupling effect may hinder the signal generated by the target objects. The signal process applied in GPR – a kind of NDTs, are mainly inherited from the field of seismology. In seismology, as a ground-based NSG, low-frequency acoustic energy in long wavelength is applied and travels through the Earth's layers to re-construct reflected and refracted waveforms. Seismic waves exhibit high contrasts in acoustic impedance of materials. The propagation velocity of seismic waves depends on the density and elasticity of the medium (Cerveny, 2005). Similarly, GPR also images the wave reflected and refracted from the subsurface, but compared to various wavemodes in the seismic wave, it is a short wavelength electromagnetic wave with monotonic wavemode. Having said that, the signal processing and image reconstruction techniques applied in seismology are easily adopted in GPR survey.

When the received signals are processed and reconstructed into images, further image processing are required before meaningful information can be extracted. The image processing techniques used in remote sensing can be adapted and applied in GPR images. Based on their signal sources, remote sensing techniques can be classified into two groups: active remote sensing and passive remote sensing. Active remote sensing involves the emission of signals from a sensor and the reception of signals that are reflected back from the ground. In contrast, in passive remote sensing, the sensor, whether it is aerial or terrestrial, receives radiation

17

emitted from the planet. The radiation may come from both the reflection of sunlight and emissions from the Earth itself (Liu & Mason, 2013). On the other hand, based on the forms of the signal generator, techniques of remote sensing can be categorized into imagery-based or point-clouds based. GPR can be considered as an active form of remote sensing that is based on imagery. In GPR surveys, EM waves are emitted from a transmitting antenna and received by a receiving antenna. The main difference between GPR and other remote sensing techniques that are imagery-based is the media between the EM signal emitter and the target(s). Therefore, interpretation techniques that have been regularly applied in remote sensing that are based on imagery can be used to interpret GPR data. Table 2-2 illustrates the relationship between GPR and NSG/NDTs; remote sensing.

Table 2-3 Comparison among NSG, NDT and remote sensing

Methods	NSG	NDT		Remote sensing	
Technique	seismic	GPR	Others	Imagery	point cloud
Wavelength	long λ	short λ	short λ	multiple λ	short λ
Target	subsurface	subsurface	subsurface	surface	surface
Excitation	active /passive	active	active /passive	active /passive	active
Signal process	ray-based	ray-based	ray-based	\	point-based
Pixel-based image process	√	√	√	√	√

Remarks: Long λ refers to wavelength in meters level, while short λ means wavelength is centimetres or less.

In imagery-based remote sensing, recorded signals are transferred in order to construct images, which are then analysed to extract thematic information and to detect changes (Gong & Howarth, 1992; Jensen & Lulla, 1987). More specifically, the thematic information extracted includes land use, land cover classification, and features, while change detection refers to changes visible in periodically acquired images. Many well-developed methods and algorithms are available to classify pixels into semantic components. With constructed images from GPR data, which take the form of convolved EM wave signals due to scattering, , the image processing techniques from imagery-based remote sensing can be adapted to reconstruct the subsurface world from GPR images.

2.4 GPR imaging

Before applying imaging processing techniques of remote sensing GPR data, the interaction between GPR imaging and material properties is of primary importance. The interpretation on GPR representation/images is effective only when the images can fairly reveal the ground truth in a reasonable degree of accuracy.

The received GPR signals are sampled and constructed into meaningful representations. Typically, A, B, and C-scans are used for GPR data presentation in 1 to 3 dimensions, respectively. A C-scan, which is a representation of a 3D volume, images a horizontal section for a plane at a certain depth. A widely applied presentation method for C-scans is horizontal slicing, in which each image is called a depth slice. In contrast, A-scan and B-scan images are vertical sections and provide details of the reflected waveform's characteristics, including signal phase, amplitude, and estimated propagation velocity. These characteristics are affected by the properties of the host media, but through forward and inverse modelling, the subsurface world can be reconstructed. A series of adjacent GPR profiles have to be inspected in order to determine the position and size of a subsurface target. Today, 3D C-scans are increasingly popular as they assist in interpreting the subsurface in a straightforward and easily understandable manner. Furthermore, many more advanced forms of 3D GPR representations were developed recently; for instance, isosurfaces, semantic images based on energy or similarity, and feature enhancements (Böniger & Tronicke, 2010a; Böniger & Tronicke, 2010b; Leckebusch, 2003). The aforementioned representations are all derivate from full cover measurements in 3D and are aimed at supplying better interpretations of 3D GPR volumes. A sequence of high-quality C-scans with reasonably accurate 3-dimensional measurements is an essential foundation for correctly depicting the subsurface world.

2.4.1 Imaging criteria

a. GPR scattering

The scattering of light from electromagnetic waves contributes to the visible appearance of most objects. The ratio of wavelength to a reflector's radius determines its visibility. Electromagnetic waves can be modelled in three forms: Rayleigh scattering, Mie scattering, and optical scattering. Rayleigh scattering happens when the feature size is far smaller than the light wavelength, Mie scattering occurs if the object size is similar to the light wavelength, while optical scattering happens when the object size is much larger than the light wavelength

(Annan, 2004). Optical scattering yields optimal reflections while, on the contrary, targets are invisible in Rayleigh scattering. Figure 2-4. illustrates the scattering concepts.
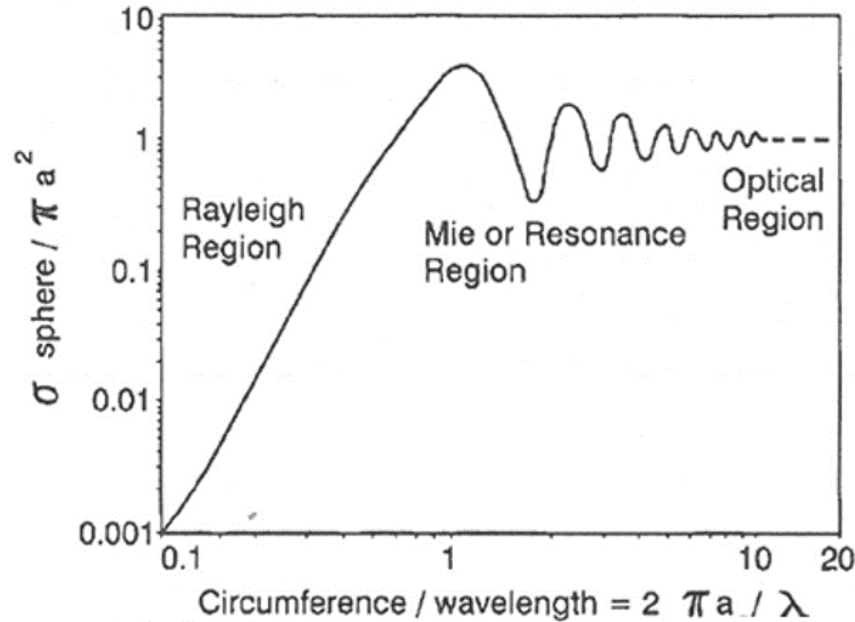
Figure 2-4 The illustration of scattering with object sizes a (Annan, 2004), σ is the ratio of GPR wavelength to the size of the scatterer, and λ denotes the wavelength.

This study focuses on civil engineering applications involving far-field measurements at higher frequencies, broadly in the 400MHz to 3GHz range. The smallest target within this field of application is a rebar in the concrete, whose radius can be as small as 5mm. According to Equation [2.18]:

$$\lambda = \frac{v}{f} = \frac{c}{f\sqrt{\varepsilon'}}$$

[2.18]

where λ is the GPR wavelength; c denotes the velocity of a GPR wave in free space, which is a constant of 0.2998 m/ns; f is the centre frequency; and ε' denotes the host material's real part of complex permittivity.

Optical reflection forms the basis of most GPR applications in civil engineering. Even the deepest targets are buried within the upper few metres of the subsurface and, if the soil is non-conductive, are detectable even at higher frequencies. Additionally, as the radar signal penetrates deeper, higher frequencies tend to be absorbed and hence the centre frequency is shifted to a lower region. In summary, a target object is "visible" to GPR only when optical reflection occurs.

b. GPR spatial resolution

Once an object is visible, the next question concerns how precisely it can be imaged. Where GPR imaging quality is concerned, spatial resolution and object resolution need to be considered.

GPR spatial resolution is determined by characteristics such as the radar signal, frequency, wavelength in materials, survey settings, and EM properties (Pérez-Gracia et al., 2010). Spatial resolution can be categorized into horizontal resolution and vertical resolution.

The horizontal resolution is defined as the capability of GPR to distinguish two adjacent targets on the same plane, while vertical resolution describes the GPR system's ability to separate two adjacent objects at different depths. When two targets are closely placed, long wavelengths will result in reflection superimposition. According to Nyquist's sampling equation, the resolution is considered to be ¼ of the wavelength, although in-field measurement a figure of ½ wavelength is more consistent with the actual measured field resolution in many cases (Al-Qadi & Lahouar, 2005; Pérez-Gracia et al., 2010).

Whether two adjacent objects at the same depth can be separated is mainly dependent on the footprint of the radar beam at a particular depth (Pérez-Gracia et al., 2009). Knowledge of the radiation pattern is therefore crucial for accurately estimating the GPR system's spatial resolution. Researchers have modelled GPR radiation patterns by measuring the main lobe and then providing various radiation patterns (Jiao et al., 2000; Lambot et al., 2004; Pérez-Gracia et al., 2009).

The shape of the radiation pattern significantly affects the footprint of a GPR beam. A narrower beamwidth with a smaller footprint provides better spatial resolution. established a simplified model of horizontal radar resolution, which was based upon the relationship between object size and radar resolution. The footprint is usually estimated as the First Fresnel Zone (FFZ). There are various equations used to calculate the Fresnel zone in the far-field (Leckebusch & Peikert, 2001; Leucci & Negri, 2006; Leucci et al., 2003). The estimation of spatial resolution is always rough as it involves many factors, such as the design of the antenna, frequency, beam angle and host medium properties. Among the available equations, Equation [2.19] is preferred for its computational efficiency and stable performance (Pérez-Gracia et al., 2008):

$$r = \sqrt{\left(\frac{v^2}{16f^2} + \frac{vz}{2f}\right)} \qquad\qquad [2.19]$$

where r is the radius of the FFZ, z denotes depth, f is the standard for dominant frequency, and v is the GPR wave velocity. Specifically, f refers to the centre frequency of the wavelet reflected from a specific object, which is normally smaller than the centre frequency suggested by the manufacturer (antenna point to air). The centre frequency is determined after performing the wavelet transform in the time-frequency domain (Lai et al. 2014).

c. Dielectric contrast and attenuation

Another critical aspect of slice quality is the object visibility; whether the target object can be distinguished from the background medium, which is governed by dielectric contrast (manifested as reflection coefficient) in Equation [2.20]:

$$R = \frac{\sqrt{\varepsilon_1} - \sqrt{\varepsilon_2}}{\sqrt{\varepsilon_1} + \sqrt{\varepsilon_2}} \qquad\qquad [2.20]$$

where R is the reflection coefficient across two vertical interfaces and ε denotes the dielectric constant/relative permittivity of the host medium.

Attenuation is another significant effect on a radar's wave amplitude. When a GPR signal penetrates a lossy medium, the amplitude decreases with depth. The attenuation rate depends on the electrical conductivity of the host medium. In order to make deeply buried objects visible, a range gain function is applied to the data to compensate for the effects of attenuation. The use of different types of gain functions, however, can result in various "artificial" reflection intensities being unintentionally added to the subsurface image and an increase of noise alongside the signal. Knowledge of the attenuation rate in the real environment can help reduce errors and more accurately delineate the subsurface. The received signal intensities are transformed into colours, and the scale used in the transformation process is very important because it describes the reflection contrast. A linear transform that presents a true intensity contrast involves limited operator interpretation, and it is suitable for a majority of GPR purposes, except in certain circumstances where signal exaggeration is required. The use of a non-linear colour transform would actually increase the degree of human intervention and complexity in the image creation process. In this study, a linear colour transform was applied in all cases.

2.4.2 Current developments in GPR imaging

Daniels et al. (1997) pointed out that the purpose of processing GPR data is to change its appearance, rather than change its interpretation. Before attempting to interpret the GPR data, it should be properly processed, so as to extract the useful information while filtering out irrelevant noise.

Having been through decades of development and application, the techniques of GPR signal processing are becoming increasingly mature. Jol (2009) and Annan (2004) summarized the typical flow for GPR signal processing, as shown in Figure 2-5. The workflow is widely accepted and implemented in the industry.
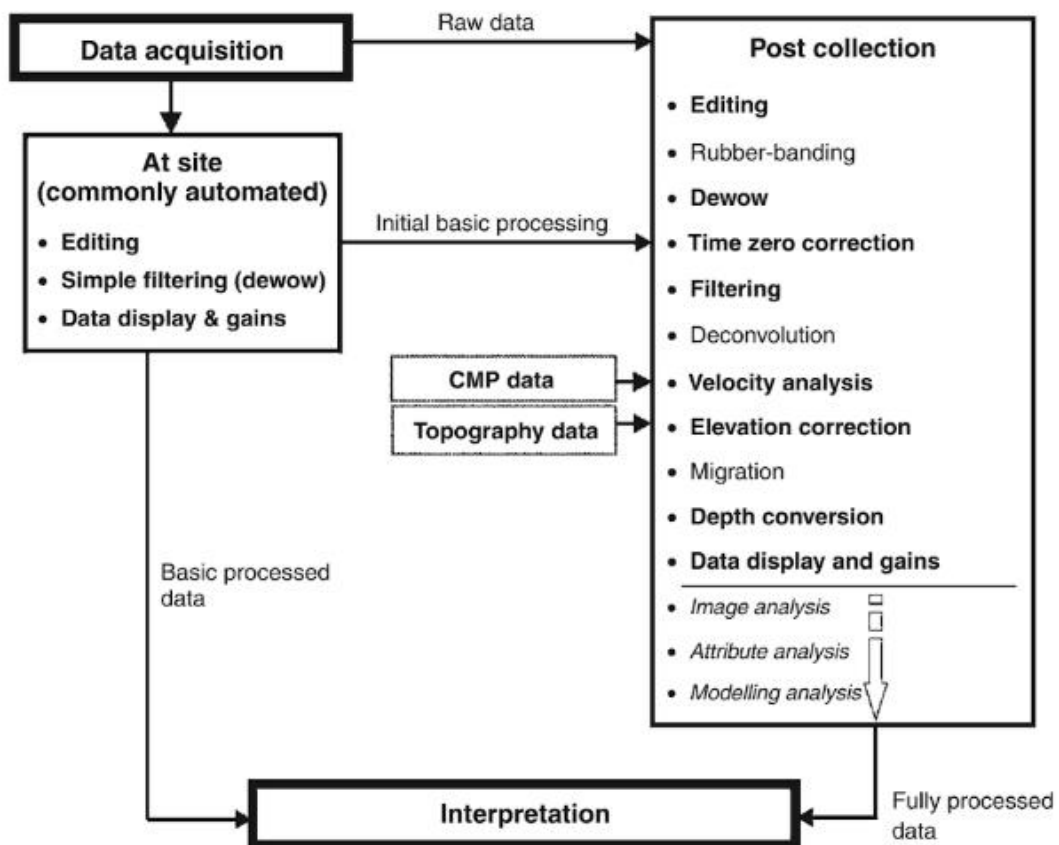
Figure 2-5 Typical processing sequence of 2D GPR data (Jol, 2009)

a. De-wow and adjust direct current shift

'De-wow' and 'adjust DC shift' refer to temporal filtering used to remove very low frequency and direct current components from the data. Very low frequency components of the data are associated with either inductive phenomena or possible limitations relating to the

instrumentation's dynamic range. Figure 2-6 present the effect of "de-wow": the later part of a GPR trace is shifted up in (a), and it is corrected to the middle with "de-wow" in (b).
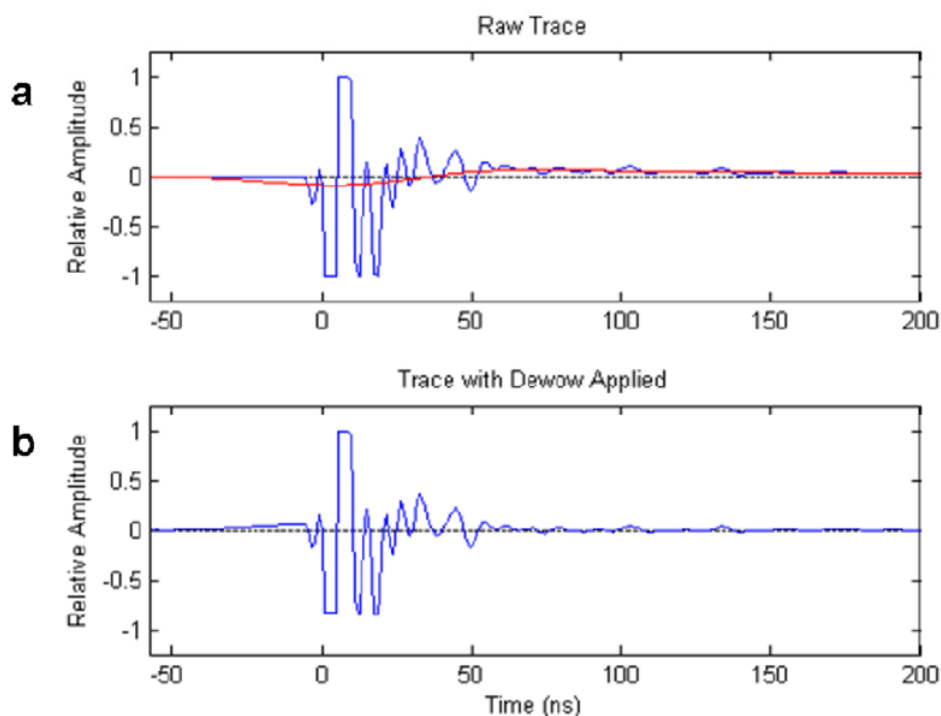
Figure 2-6 An example of the de-wow on a GPR trace (Rowell et al., 2010): (a) before and (b) after the de-wow.

b.   Time-varying gain

GPR signals are rapidly attenuated as the wave propagates into the subsurface. Reflection events from greater depths may be invisible or indiscernible. Equalizing amplitudes through the application of a radar time-dependent gain function compensates the rapid fall-off in radar signals over longer travel distances. This is referred to as "time varying gain" (Goodman & Piro, 2013), such as automatic gain control (AGC), which is a continuously adaptive gain, that is helpful when it is important to show all information irrespective of amplitude fidelity. The use of manual gain with user-defined gain function is another alternative. Exponential or linear gain imitates and amplifies the mathematic model of the attenuation curve of the data. Another widely used gain is manual y-gain, which allows operators to define multiple points with a desired amplitude along the time axis in each A-scan. Each type of gain relies on different adjustments against the attenuation in different situations.

c.   Filtering

Filtering can be applied before or after time gain as long as the effect of the gain is understood. Temporal filtering means filtering along the time axis of the dataset.

A bandpass filter is a 1D filter that works in the frequency domain. Waveforms are transformed into the frequency domain using Fast Fourier transforms (Daniels, 1996; Malagodi et al., 1996). Certain ranges of frequencies are retained while the rest is removed. As the signals are decomposed into their spectral components, the amplitudes of different frequencies can be adjusted by reducing or enhancing the desired frequencies (Goodman & Piro, 2013). High-pass and low-pass spatial filtering are two well-known types: the high-pass spatial filter retains dipping responses and removes flattened events, and vice versa for the low-pass filter. Median and mean filters are 2D filters used to smoothen noise spikes and can be applied in both the time or space domain.

Background removal is another form of 2D spatial filtering that removes repetitive responses in every trace. It eliminates constant and systematic clutter noise across the radargram. A popular background removal process involves calculating the average pulse across the entire radargram and then subtracting it from each individually recorded pulse (Bernabini et al., 1995; Malagodi et al., 1996)

d.   Time zero correction

The zero ns position ('time zero') changes depending upon the ground material. The definition of the first measured arrival as time zero has been much debated. When an antenna is placed on the ground surface, the direct wave is altered in shape and shifts later in time by up to several tenths of a nanosecond, due to the dielectric loading of the ground material in the near field of the antenna (Yelf, 2004). Time zero correction refers to moving the zero ns position of each trace in order to eliminate the lag from electronic zero to ground zero. GPR users are advised to estimate the time zero in each application through their own experiments gained from sites.

e.   Velocity analysis

As discussed in Chapter 2.1, the mathematical form of the hyperbolic reflection relates spatial position (x) to travel time (T). A handy aid to interpretation when estimating GPR wave velocity is to visually fit a model hyperbolic shape to the GPR data, using the two-way travel time as described by Equation [2-7]. developed an algorithm that takes the object radius into consideration when estimating the wave velocity.

f.   Elevation correction with topographic data

For surveys on undulating ground, GPR scans must be shifted based on elevation changes. Standard topographic adjustments require the velocity to be estimated from the radargrams, and then the scans can be shifted vertically to account for the change in topography (Tanaka et al., 2009). The tilt of the scan is estimated using a ground slope calculation based on measurement of the local topography of the GPR scan. This slope is used to project the ray signal emitted from the tilted antenna.

g.   Migration

Most GPR antennas emit a broad beam of radio energy into the ground, which results in hyperbolic reflections being recorded from round objects buried in the ground. Objects lying oblique to the antenna are still recorded because of the breadth of the beam angle. Migration regresses hyperbolic reflections back to point source reflections by adding up all the energy along the hyperbolas across the radargram, and places this energy at the apex of the hyperbola. The Kirchoff migration in the time domain and Stolt migration in the frequency domain are two popular migration algorithms that yield similar results in most cases. It should be noted that migration is only useful for circular objects.

h.   Envelop to erase phase information

The enveloping of the recorded radar signal is known as a Hilbert Transform. It is a mathematical transformative process that uses a Fourier transform. The negative reflections are swopped 90 degrees and processed with an inverse Fourier transform. The recorded pulse is then 'enveloped' to produce a reflection that resembles the geometry of a circular object. In this process, the phase information is lost.

i.   Depth conversion

After estimating time zero and the GPR wave velocity, the depth of an object can be calculated by measuring the two-way travel time. Note also that the estimated depth after migration and envelop appears deeper than that of the hyperbolic reflections. Depth must therefore be estimated before migration and envelop are performed.

Having been through above processes, the radargram is ready for interpretation and it can be used to construct 3D or 4D GPR representations. It should be noted that not all 2D processes are necessary, and data processing steps are selected using a 'fit-for-purpose' approach.

2.4.3 Demand for 3D to temporal GPR imaging

From a review of a large number of research studies conducted in recent decades (Lai et al., 2018a), it is evident that 3D C-scans were first utilized in the 1990s (Goodman et al., 1995).

The quality of C-scans is controlled by various factors. The first is the characteristics of the GPR signal, including its frequency and beamwidth, which determines it resolution. The second factor is the scattering of unwanted buried objects, as well as high conductivity in the host material leading to the a attenuation and absorption of the GPR signal. These are the major limitations posed by the interaction between both GPR antenna design and the material properties of the subsurface, thus not much improvement can be made.

On the other hand, the techniques used in data collection and processing also influence significantly the C-scan quality. While a 3D C-scan is constructed by a number of 2D B-scan measurements, denser measurements lead to a better image quality for revealing the subsurface reality. Discrete measurements require interpolation and resampling, resulting in very different imaging results arising from the different data collection methods and/or processing algorithms. The process of generating C-scans is still immature and yet to be standardized. The parameters used for the generation of slices are mainly based on the experience of operators, which leads to inevitable human bias in the imaging results (Millington & Cassidy, 2010). Because the choice of different parameter settings may result in completely different images, it is hard to determine whether the subsurface image is a proper representation of the underground reality. Therefore, in order to optimize the subsurface image and produce more accurate results, it is necessary to provide a standardized workflow for adjusting the parameters of C-scan processing. Also, time-lapse measurements, which look at subsurface changes by comparing C-scans at different times, are used to capture consistent and reliable images. Due to the variation of signals emitted by different antennas, it may be difficult to achieve consistent GPR measurements at different times.

The use of object-oriented C-scans is a supplementary approach since only semantic information about an object is provided. Instead of interpreting complex waveforms and digits,

a "health record" for buried infrastructure can be established from C-scan images using straightforward image processing, on the basis that the object condition is correctly described.

Nowadays, GPR 3D imaging has been widely applied in diverse fields of civil engineering: for example, in mapping underground utilities (Birken et al., 2002; Lai et al., 2017b; Metwaly, 2015; Ristic et al., 2009); measuring change of physical properties in materials (Kowalsky et al., 2005; Léger et al., 2014; Leucci et al., 2003); and inspecting structural conditions (Alani et al., 2013; Baker et al., 1997; Lai et al., 2013; Lai & Poon, 2012). More specifically, Nuzzo et al. (2002) imaged an archaeological site and pointed out that slice thickness was crucial as coarser slice thickness could lead to less accurate depth estimation, although they did not suggest a suitable range for slice thickness. Grasmueck et al. (2013) and Marchesini & Grasmueck (2015) imaged fractures and suggested that survey profile spacing should be no larger than ¼ wavelength – unrealistic for the civil engineering applications with higher frequencies, while suggested the use of 3 profiles for delineating an anomalous body – the size of the body is often unknown. A rule of thumb is that the denser the measurements, the better the image quality become, but the higher the survey workload is involved. Allroggen et al. (2015) stated that a dense profile spacing should be applied but only vaguely described other parameters used, while it was suggested that excessive data processing would introduce greater imaging variation. Topczewski et al. (2007) used linear interpolation to fill in gaps between profiles in order to better represent the object shape, while Barraca et al. (2016) applied rectangular interpolation with a radius equal to profile spacing. The interpolation methods they used were suitable for imaging specific objects, but there was no suggestion on a universal rule like (Jol, 2009). Cassidy et al. (2011) confirmed that practical experience plays a remarkable role in determining suitable values for imaging parameters. Some research has tended to skate over the process of 3D image production (Alani et al., 2013; Hugenschmidt & Kalogeropoulos, 2009; Porsani et al., 2012; Sagnard et al., 2016). Lualdi et al. (2003) pointed out that system resolution and antenna positioning accuracy are vital for high-quality 3D GPR imaging, while denser measurements ensure that image degradation is minimized. In order to balance the survey workload, an indication and image quality on the largest acceptable profile spacing is needed. For acquired data, Goodman et al. (1995) summarized the processing flow of 3D time-slice reconstruction from a series of radargrams (B-scans) and focused on 3 major steps: setting up the survey grid, cutting slices and interpolation. These steps are reflected in the above

mentioned researches in this paragraph, but a rigorous workflow, as used in 2D processing (Jol, 2009), is still missing.

In summary, the accuracy of 3D C-scans depends upon denser and more reliable 3D measurement points. GPR data acquisition is time consuming and labour intensive, and achieving full-resolution imaging might be unrealistic in practice. This study aims to establish a bridge connecting GPR resolution theory and survey practice, and strives to achieve a balance between acceptable imaging quality and survey workload for various imaging purposes. As the positioning accuracy is mainly determined by the system design, the post-processing stage cannot provide much image enhancement. The above literatures applied the slicing and the interpolation to construct 3D images – C-scans. However, the values used were case-specific, and no general rules were summarized in this field, which makes the C-scans generation expertise-based and also implies that biases are inevitable. With different values, the C-scans generated by the same set of GPR data can vary. These discrepancies also introduce bias into the interpretation afterwards. The industry of GPR surveys is in high demand for the comprehensive guideline on 3D imaging. Therefore, the first objective of this study is focused upon 3D reconstruction from acquired GPR data.

2.5 Pattern recognition techniques

When the GPR representations (A, B, and C-scans) have been prepared, further interpretation can be conducted. But even thanks to the development of antennas and control units, leading to largely reduced time of field surveys, city-wide GPR surveys are still tedious exercises. The complex subsurface environment distorts GPR responses, and the analysis of GPR patterns is therefore still mainly reliant upon human visual interpretation. If large-scale GPR surveys are conducted, it involves manual interpretation of thousands and more GPR profiles.

Pattern recognition is a prerequisite of intelligent approaches to classifying measurements. It is a concept that includes a broad range of methods that can integrate loosely related knowledge or techniques (Bishop, 2012; Tou & Gonzalez, 1974). Pattern recognition mainly consists of three processes: information reduction, information mapping, and information labelling. It is very often the case that a single technique cannot provide the optimal solution for a given pattern recognition problem (Schalkoff, 2007).

Recently, research has focused upon automatically interpreting GPR responses using pattern recognition techniques (Al-Nuaimy et al., 2000; Ayala-Cabrera et al., 2011; Gamba & Lossani,

2000; Ghasemi & Abrishamian, 2007; Pasolli et al., 2009; Xie et al., 2013). Applications of automatic recognition techniques mainly focus on the more typical kinds of GPR responses; namely, hyperbolas. The methods used in past research, such as the Hough transform (Simi et al., 2008), support-vector-machine (SVM) (Xie et al., 2013), and neural network (Gamba & Lossani, 2000), worked well in detecting hyperbola reflection. In contrast to hyperbolic reflections generated by point reflectors, reflections from voids have no fixed morphology, as the subsurface voids themselves come in various sizes and shapes. The subsurface defects may yield GPR reflections with various morphologies: geometry-based pattern recognition methods are not capable for depicting them. In terms of more intelligent machine learning methods, the recognition and distinction of these defects demand sufficient descriptions on how they present in GPR data, which means large amount of training data is required. Besides, it is difficult to have ground truths in GPR survey currently, and therefore supervised approaches listed in Table 2-4 are difficult to be implemented. A comparison table on various pattern recognition techniques is given as Table 2-3.

Table 2-4 Comparison of a few pattern recognition techniques

Approach	Method	Pros	Cons
Supervised	Support vector machine (SVM)	1) Can detect complex features; 2)Works on multiple tasks;	1)Require enough ground truths as a training set; 2)High demanding in hardware.
	Neural network		
	Random tree		
Unsupervised (Specific shape detection)	Hough transform	1)Less demanding in hardware; 2)Performs well in specific targets; 3)Require less or no training	1)Need clear definitions on the target; 2)Work on a single target.
	Laplacian		
	Canny		
	Pyramid		

2.6 Change detection in GPR images

The last objective of this study is to develop a workflow for temporal diagnosis with GPR images. The change detection techniques in image processing help to identify temporal anomalies from time-lapse data.

The change detection framework uses multi-temporal datasets to analyze the temporal effects of phenomena and quantify the changes observed (Hussain et al., 2013). Most change detection from images can be categorized from two perspectives: one is the classification body, which involves pixel-based change detection or object-based change detection; while another is the classification strategy, which uses supervised change detection or unsupervised change detection. An enormous number of methods were developed in the past decades, and the selection of an appropriate change detection method might be difficult in practice (Lu et al., 2004).

Pixel-based change detection methods work on every single pixel. Discrepancies among temporal datasets are identified by comparing the pixel values. Image mathematical methods, such as image differencing or rationing, are straightforward pixel-based methods. They require no object information but are very sensitive to speckle noise (Hussain et al., 2013). With the exception of reflection intensity, semantic meaning can be assigned to the pixel value. Some typical examples include image classification, normalized digital vegetation index (NDVI), and advanced machine learning methods – such as principal component analysis (PCA), artificial neural networks (ANN) or support vector machine (SVM). These latter methods label pixels with pre-defined class numbers (Canty, 2014; Gopal & Woodcock, 1996; Huang et al., 2008; Lillesand et al., 2014; Lunetta et al., 2006). Temporal changes are identified from pixels with the same label. These approaches can eliminate errors from tiny scatterings but introduce errors from the classification process itself. The quality of classification therefore depends on an accurate training dataset (Coppin et al., 2004). On the contrary, object-based change detection methods work on the extracted object. In some cases, pixels, which are cells recording radiation intensity, are not the most suitable unit for describing an object (Johansen et al., 2010). The very first step is grouping pixels into segments according to the target objects' characteristics, such as texture, shape, geometry, and spectral information (Blaschke, 2010). Thereafter, changes within the targeted segments are identified by comparing classified segments in the temporal dataset. Some well-known object-based detection methods include a comparison of

classified objects and multi-dataset detection of objects' change; these methods classify segments rather than pixels into either changed or unchanged groups (Singh, 1989). Compared with pixel-based methods, object-based methods place emphasis on specific objects, thus affects of other sources (equipment, untargeted objects, background environment) may be eliminated.

Whether pixel-based or object-based change detection methods are used, both can be either supervised or unsupervised. Supervised methods demand sufficient knowledge of the information given in images. Given the existence of a training dataset extracted by ground truthing, a model can then be established and applied to the whole image. The supervised methods are highly sensitive to the accuracy of the training dataset (Volpi et al., 2013). Normally, unsupervised methods iteratively optimize the results when discriminating between changed and unchanged. Since no preliminary definition is required for unsupervised methods, their reliability and accuracy are hard to ascertain (Bovolo & Bruzzone, 2007). A comparison table on various change detection methods is given as Table 2-5.

Table 2-5 Strength and weakness of each kind of change detection approach

Approach	Pixel-based	Object-based
Supervised	- Details in images are maintained - Sensitive to the training dataset - Sensitive to scattering and random errors	- Robust on scattering effects - Avoid errors from the sensor - May lose details
Unsupervised	- Require less preliminary knowledge on targets - Details in images are maintained - Less reliable	- Rely on accurate segmentation - Avoid errors from the sensor - May lose details

Appropriate customization is essential when adapting image change detection techniques to GPR 3D slices. A successful implementation was provided by Hong et al. (2017), which detected corrosion in reinforced concrete using the intensity change in GPR depth slices. The subsurface environment of the concrete specimens is relatively homogenous, that the variation in the reflection intensity can only come from the changes of material states in the specimen. In terms of the complex underground subsurface, it is hard to extract the information of target objects from the surrounding environment. Allroggen et al. (2015) and Lai et al. (2016c) observed the water seepage from temporal C-scans. But the scale of these two studies was small and the experimental environments were also homogenous – the methods used were not suitable for large scale diagnosis on the urban subsurface.

Temporal changes in GPR data are affected by various factors including moisture conditions, temperature, and equipment spectral range. Given that the resolution of GPR images can go up to centimetres, the mathematical pixel-based method may be ineffective in that range. However, object edges in GPR images are not sharply depicted because of the polarity of the material, which makes it difficult to extract the specific object with the correct shape. As discussed in Chapter 2.4, the information available in GPR images is too limited to do object-based change detection, mostly because of limitations due to scattering of the host media and an insufficiently high resolution. In summary, the unsupervised pixel-based change detection method is the most suitable approach for temporal GPR depth slicing.

Chapter 3 Standardization of GPR imaging processing

Chapter 2.4.3 introduced the current development of GPR imaging. There is mature knowledge on radargram processing, but there is not a protocol on the C-scan generation. The 3D images produced by different operators can vary from one another, and may lead to different interpretation An example is shown in Figure 3-1.
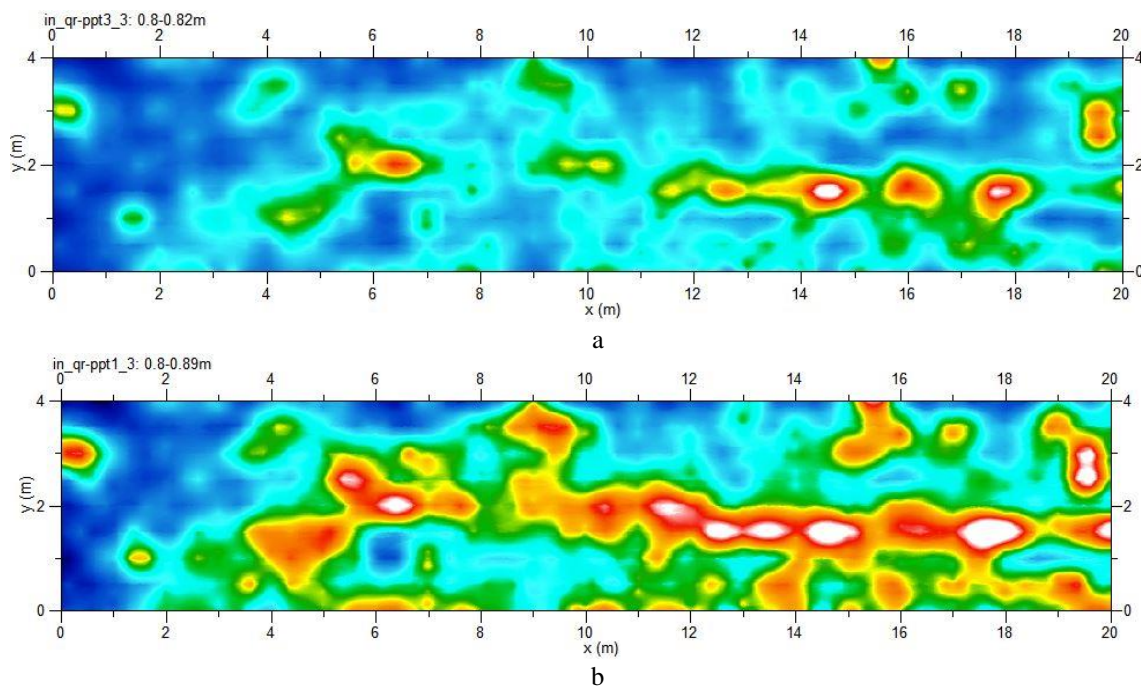
Figure 3-1 Illustrations on the variation of C-scans generated from the same set of GPR data showing a continuous drainage pipe. (a) the C-scan with a slice thickness (ST) as 0.02m; (b) the C-scan with a ST as 0.1m.

A drainage pipe is shown at the middle of Figure 3-1: it is doubtful whether the continuous pipe is disconnected or not although both images are from the same set of GPR data. This chapter introduces a standardized 3D GPR imaging flow, and supports it with well-established GPR theories reviewed in Chapter 2 and supported with 25 sets of empirical experiments conducted in various fields, e.g. concretes, underground utilities, subsurface voids.

3.1 Quantification of imaging parameters

It is impossible to have consistent and comparable imaging results without a unified workflow. There are various factors affecting the 3D imaging result, including (1) GPR capabilities (Chapter 2.3.1), (2) electromagnetic properties of target objects and surrounding materials (Chapter 2.3.5), and (3) the imaging processing methods (Chapter 2.4 and 2.5). For (1) and (2),

they are not controllable because the subsurface environment is not meant to be disturbed, and the GPR capability is determined by the electronics and antenna design which is out of control of surveyors/civil engineers. But for (3), the imaging processing is the post-processing procedure of data where improvements can be made after establishing steps and parameters in a workflow. It is also important that C-scans are merely intensity maps composed of grayscale values, which means that the physical properties of the buried objects like phase, reflection coefficients and spectral properties of GPR wave reflections contained in B-scans are lost an do not contribute to the building of the workflow. Therefore, some other known or controllable piece of information like types of target objects (Ch.3.1.1) profile spacing, slice thickness and interpolation (Ch. 3.1.2) are taken into account. Then, based on the most crucial object characteristics and GPR imaging parameters, the upper and lower limits for each parameter were defined in each case of application. A relationship between GPR imaging and object characteristics was investigated in order to construct an optimized combination for GPR imaging workflow.

3.1.1 Target objects categorization

With reference to GPR principles and application case studies, subsurface geometries and material properties are two major parameters affecting imaging. Basically, a subsurface object can be categorized into two main groups: continuous objects with linear shapes, or local objects with round or irregular shapes. The success of slice imaging depends on the dielectric contrast between the two materials being sufficient enough to record a reflection whose intensity can be imaged against the background noise level.

a. Continuous linear objects

Continuous reflections of linear objects occur at transects across a series of parallel radargrams. Underground utilities and rebars in concrete are two major kinds of buried linear objects. These linear objects are presented as continuous reflections in C-scan displays.

b. Local objects

Local objects are non-continuous structures, such as small voids or cracks, which appear in GPR radargrams as discrete reflections. The most crucial factor in identifying local objects from GPR C-scans is the object size.

3.1.2 3D C-scan parameters categorization

In line with the important characteristics of the objects discussed above, several crucial parameters in C-scan imaging are identified: the survey profile spacing, slice thickness, and interpolation.

a. Survey profile spacing (PS)

In GPR surveys, a denser GPR profile spacing can guarantee that all target objects will fall within the radar's footprint. But how dense is dense enough? It is not realistic or practicable to acquire infinitely dense GPR profiles. Normally, the spacing of GPR profiles is no larger than the anticipated object size or distance between adjacent objects ("ASTM D6432-11," 2011). However, in practice, there is always a need to balance between survey resolution and survey cost (Maas & Schmalzl, 2013). This study suggests a maximum threshold for profile spacing that can be applied while still providing a good enough resolution to identify subsurface objects. The relationship between profile spacing and object types is demonstrated in Figure 3-2(a).

b. Slice thickness (ST)

Depth slices show the radar reflection intensity over a certain thickness at a given depth. A single slice of a certain thickness presents a summed reflection within this depth range. Thicker slices produce more reflection energy, but this also introduces imprecision regarding object depth. For non-overlapping slices, the choice of the depth error is at least half the slice thickness. For slice thicknesses that are much smaller than object diameter, the object cannot be fully delineated in a single slice. The use of an appropriate slice thickness is therefore important in C-scan imaging quality. An illustration of slice thickness is shown in Figure 3-2(b).

c. Interpolation (IR)

Very often, survey profiles are not dense enough to map a full-resolution GPR image, even though full-resolution imaging has been shown to be superior (Grasmueck et al., 2005). Interpolations, such as inverse distance and kriging, are widely used to help with filling in gaps between survey grids. The selection of interpolation radius significantly affects C-scan resolution: a smaller radius preserves more true measurements while local extrema are maintained; in contrast, a larger radius creates data smoothing while details of smaller objects can be lost. How the interpolation radius affects the GPR imaging resolution is not yet codified, hence this study attempts to quantitatively analyse it. Two types of interpolation are discussed

here: one is bi-linear interpolation, which means taking both orthogonal directions of GPR profiles into computation; while the other is linear interpolation, which is applied to single direction GPR profiles and interpolation is made primarily perpendicular to the profile direction. A schematic illustration of interpolation is shown in Figure 3-2(c).
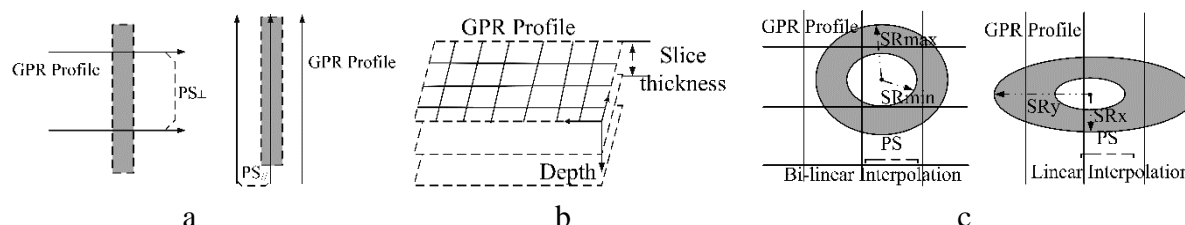
Figure 3-2 Illustrations of GPR imaging parameters. (a) GPR profile spacing with a linear object: profile may perpendicular or parallel to the object orientation; (b) illustration of slice thickness; (c) illustrations of profile spacing and radius of associated bilinear/linear interpolation, with SRmax and SR min representing maximum and minimum acceptable search radius, respectively, while SRy and SRx denotes long axis and short axis of elliptical search radius in linear interpolation, respectively.

3.1.3 Empirical experiments

Having identified these important factors in terms of both object characteristics and C-scan imaging parameters, four types of subsurface structures were designed:

A: concrete with rebar; B: underground utility; C: local objects; D: complex combination

For each experiment, imaging parameters were adjusted and the resulting image resolution and object reflection strength of C-scans were observed in order to determine appropriate ranges for each of the imaging parameters.

Before exploring the 3D C-scan process, basic 2D radargram processing was conducted. The velocity of the reflected radar waves was estimated by common offset velocity analysis (Sham & Lai, 2016), while the actual frequency reflected by the object was measured using a wavelet transform (Lai et al., 2014). Inspired by Annan (2004), the 2D processing was simplified to avoid introducing unnecessary artificial signal noise. A processing flow is proposed for typical 2D processing of common offset GPR data (Annan, 2004; Jol, 2009). Several necessary steps were chosen for this study, as follows: dewow to remove the DC shift in the waveform; static correction to adjust time-zero; range gain for consistent amplitude contrast; bandpass and background removal; and frequency domain phase shift migration with independent velocity.

After the 2D processing, the visibility of underground through GPR reflections of variety of target objects enhanced, because of amplifying the weak signals in larger depth and suppression of scattering noises. This workflow has been widely accepted and applied in the industry nowadays. When stacking B-scans into C-scans, the reflection intensity is transformed and presented as grey scale pixel images with linear colour transforms. The colour scale applied in each experiment was identical.

3.2 A 3D imaging workflow

Based on the experience of these empirical experiments, a workflow diagram is summarized in Figure 3-3. Three levels of C-scan imaging are identified and presented in sequence in the workflow diagram. The first, in the green box, is the profile spacing (PS) which affects the horizontal resolution of C-scans. The second, in the blue box, is slice thickness (ST), which determines the vertical resolution. Antenna frequency, object size and location depth all have effects on suitable thickness selection. The last level is the interpolation radius (purple box), which also has a crucial impact on the GPR C-scans' horizontal resolution.
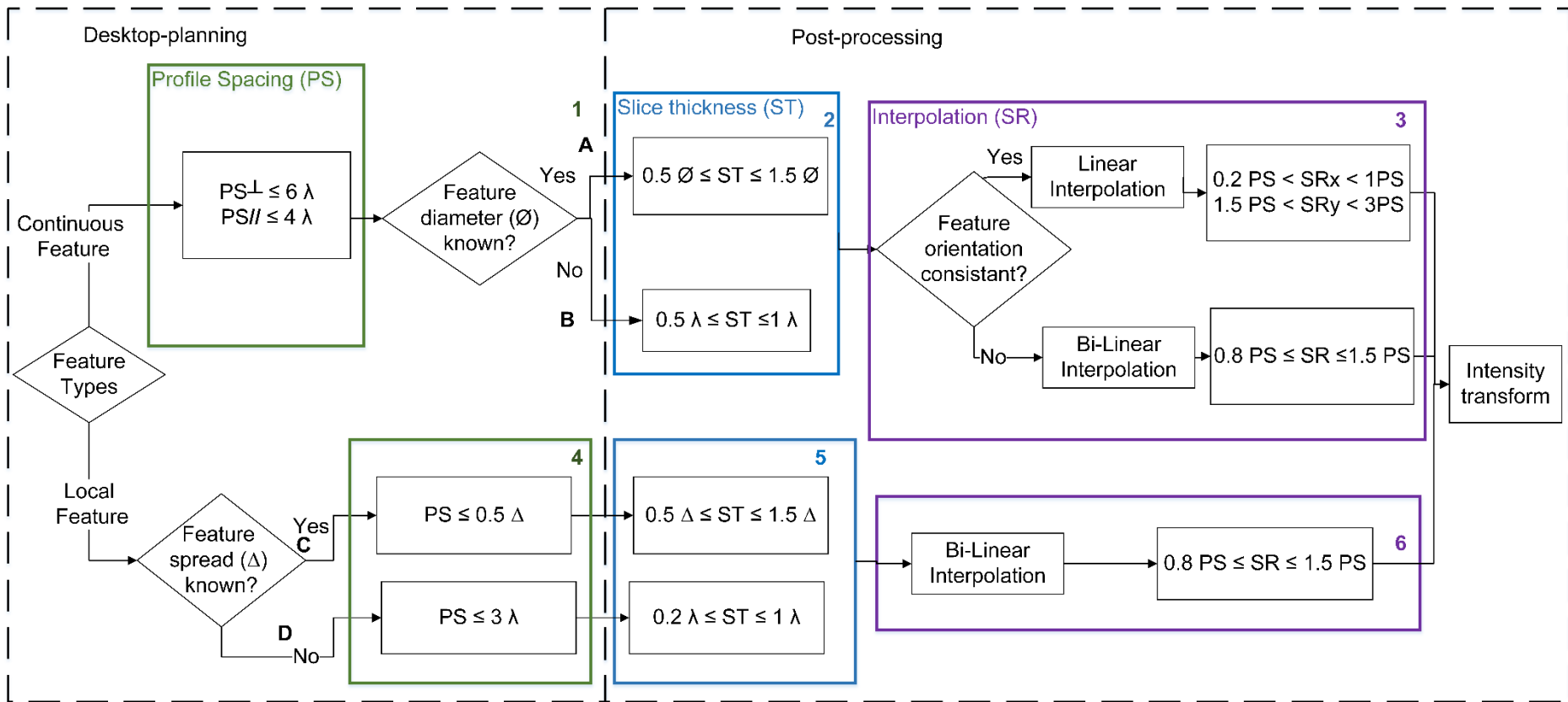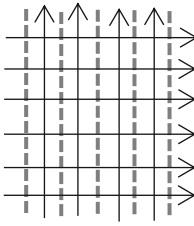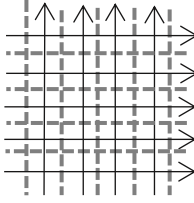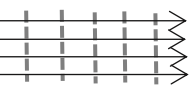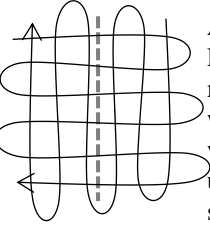
Figure 3-3 3D GPR imaging workflow based on empirical experiments. Remarks: (1) based on equation [2.18], where v can be determined by common offset velocity analysis (Sham & Lai, 2016), f can be determined by wavelet transform (Lai et al., 2014); (2) an object spread (Δ) denotes object's maximum spread along a traverse.

3.2.1 Representative Experiments

To illustrate the proposed workflow diagram, 7 representative experiments were selected: they represent the major targets that GPR can work on in the urban area. Detailed descriptions on these 7 representative experiments are provided in Table 3-1 and Table 3-2.

Table 3-1 Experimental Specification

Workflow Path	Case	Site Photo	Survey Grid (↑)	Site Specification
A (Concrete)	Concrete Wall (CW) GSSI 2GHz			The concrete wall is placed in PolyU, with 2 layers of rebars embedded. The wall is 1.5*1.5m large.
	Concrete Slab (CS) GSSI 2GHz			The concrete slab with 2 dense layers of rebars embed in is located in the Ferry terminal of Hong Kong, the slab was 3.7*3m large.
	Stepped Steel (SS) GSSI 2GHz			The specimen is placed in PolyU. Ten rebars stairs are embedded in the concrete block. Vertical/horizontal distance between each rebar is 0.2/0.1m.
B (Underground Utility)	Back Lane (BL) IDS 600 and 200MHz			A school lane in PolyU, a concrete made drain pipe with 0.22 diameter was buried underneath. The site area is 50*5m.
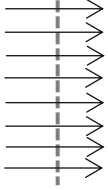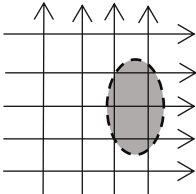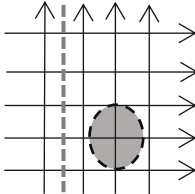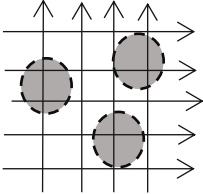
	Island South (IS) GSSI 400MHz			A pavement road section at Island South in Hong Kong. The road section was 200m long and 10m width. A rising main is buried below ground.
C (Local Feature)	Surface Void in laboratory (LV) IDS 600MHz			The void was placed in the utility laboratory in PolyU. The void is 0.8*0.6*0.15 in size, and surrounded by garden soil. The whole survey area is 4.5*3m.
D (Complex)	Cathedral (CA) IDS 600MHz			The cathedral is located in the Central District of Hong Kong. The site area is 8*5m size concrete floor.
	Archaeology Site (AR) GSSI 900MHz			The site is located in Tung Chung of Hong Kong, filled with dry soil. The survey area is 20*10m large.

Table 3-2 Measured and calculated variables in survey A to D

Survey	Case	GPR Specification				Imaging Parameters				Object Detail	
		f(GHz)	v(m/ns)	λ(m)	FFZ(m)	PS(m)	ST(m)	IR(m)	FS(m)	Depth(m)	FD(m)
A	CW	1.9	0.128	0.067	0.06	0.1	0.02	0.08	0.2	0.065	0.02
	CS	2.2	0.128	0.05	0.056	0.1	0.02	0.08	0.2	0.15	0.02
	SS	2.2(2nd)	0.128	0.058	0.055	0.1	0.008	0.07	0.1	0.085	0.01
		2.6(5th)	0.106	0.04	0.095	0.1	0.015	0.07	0.1	0.135	0.01
B	BL	0.210	0.105	0.48	0.43	0.5	0.301	0.4	\	0.62	0.2
		0.496	0.0815	0.163	0.24	0.5	0.245	0.4	\	0.62	0.2
	IR	0.710	0.101	0.208	0.108	1	0.2	0.7	\	0.55	0.2
C	LV	0.481	0.104	0.207	0.104	0.3	0.1	0.21	\	0.1	0.6
D	CA	0.680	0.098	0.14	0.09	0.5	0.116	0.3	\	0.3	0.5
	AR	0.780	0.139	0.178	0.216	0.5	0.1	1	\	0.5	\

Remarks: f is the frequency measured with Lai et al. (2014); υ is the measured velocity estimated by Sham & Lai (2016), λ and FFZ are the calculated wavelength (υ/f) and the calculated radar footprint, respectively; PS, ST IR, FS, D, FD are profile spacing, slice thickness, interpolation radius, object spacing, object depth and object diameter, respectively.

3.2.2 Continuous Objects (Survey A/B)

The shapes and orientations of profiles to object alignment are of vital importance when mapping continuous objects.

a. Profile spacing for the continuous object (Box 1 in Figure 3-3)

Different profile spacing settings were tested for imaging the concrete wall (CW) and concrete slab (SW), in order to investigate the minimum requirements for GPR profile spacing, as shown in Figure 3-4. It is widely accepted that the denser the GPR profiles acquired, the higher the GPR imaging resolution achieved, but there is no lower boundary on profile spacing. In principle, the profile spacing should be smaller than half the rebar spacing so that both the gaps and rebars can be mapped. In all civil engineering applications, three profiles for one object can guarantee high-quality C-scans. When working in larger survey areas, data collection of such dense profiles is time consuming and labour intensive. Then a trade-off would be to reduce the number of profiles and sacrifice a higher resolution, while ensuring that the target can be still mapped.

Figure 3-3(a) and (c) show the imaging result when profile spacing is equal to rebar spacing, which allows each rebar to be distinguished clearly. When the profile spacing is twice that of the rebar spacing, obvious artificial errors occurred: each rebar was interpolated to be straight, as shown in the red circled areas in Figure 3-3(b) and (e). Although the general areas with a stronger intensity were still mapped, they were shifted in position. In principle, at least two reflectors are needed for the definition of one linear shaped rebar. Although there were insufficient GPR profiles acquired, the general subsurface scene could nevertheless be imaged by interpolation without loss of imaging clarity.

	\	PS = 1FS	PS = 2 FS
Concrete Slab	\	a	b
	PS = 0.5 FS	PS = 1FS	PS = 2 FS
Concrete Wall	c	d	e
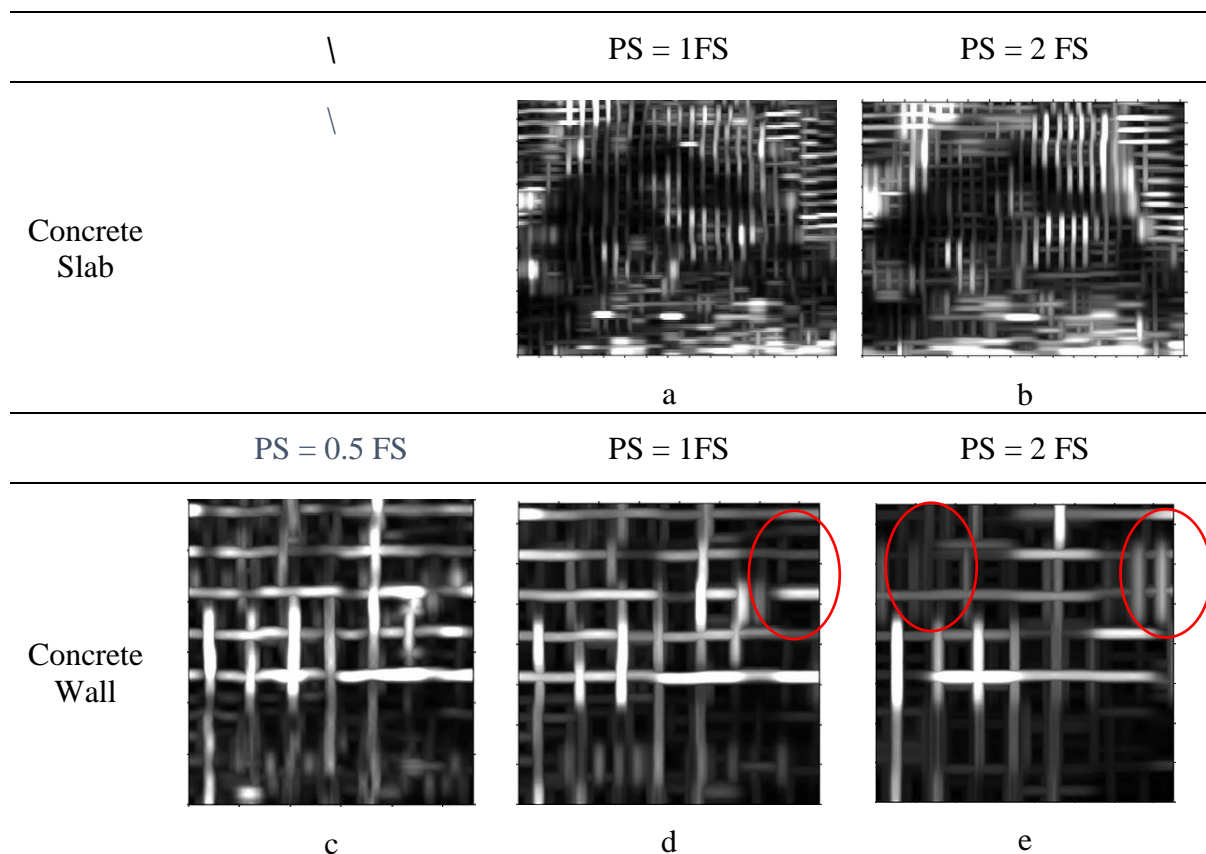
Figure 3-4 C-scans of concrete with different PS. (a) and (b) are C-scans of the concrete slab with the profile spacing equals 1 or 2 times the object spacing; (c-)(e) are C-scans of the concrete wall with profile spacing equals 0.5, 1 or 2 times the object spacing.

However, normally known and consistent object spacing only exists in concrete and rebar mapping. In this case, the rebar diameter is normally far smaller than the rebar spacing, and rebar spacing – 0.1 to 0.2 m – is often significantly larger than multiple times the radar wavelength. When object size and object spacing are both unknown (i.e. Path B in Figure 3-3), which is rare in most cases, the radar's wavelength is then the only factor taken into consideration when computing the GPR horizontal resolution, based on the principle of radar footprint. As discussed in Chapter 2.4.1, the profile spacing should be ¼ of the wavelength. In Path A experiments (CS and CW), the wavelengths of the 1.9-2.2GHz radars were 0.05-0.06m. Even though it is smaller than the rebar spacing, it was still acceptable for imaging such linear objects. In addition, diameters of linear objects are very often small (i.e. diameters of rebar and utility), compared to their lengths. Applying diameter as a reference to define the survey profile spacing may not feasible. Thus, the GPR wavelength is applied to determine the suitable range of profile spacing.

The road section in Island South (IS) was an ideal example for validating the imaging performance of different profile spacings for mapping single linear shaped objects, as shown in Figure 3-5. When mapping continuous underground utilities within larger areas, even fewer dense profiles can be used.
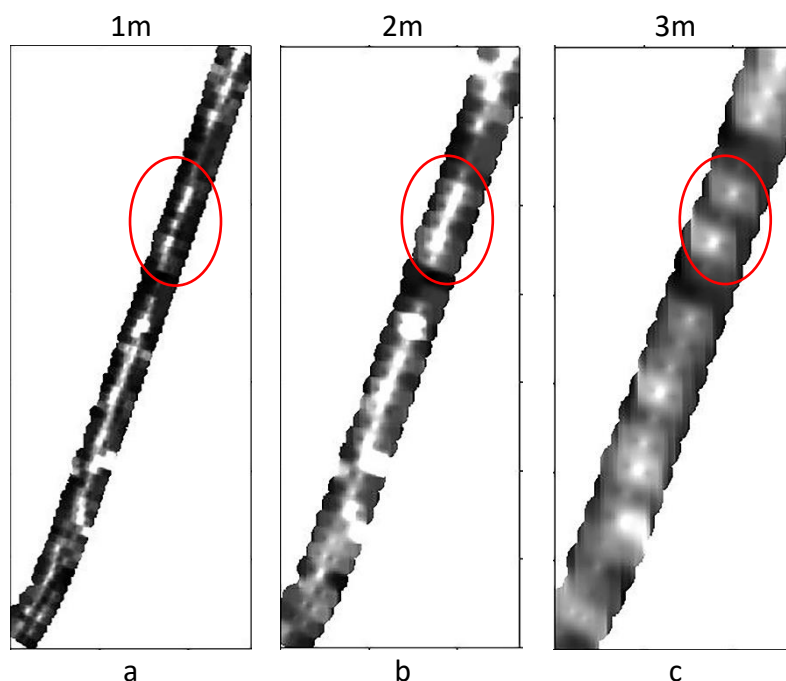
Figure 3-5 C-scans of Island Road with different profiles spacing. (a) 1m, (b) 2m, and (c) 3m profile spacing.

When comparing the 3 generated results shown in Figure 3-5, there is clearly an upper limit to profile spacing. According to Table 3-2, the 1-3m profile spacing of the IS case study is significantly larger than the object (the pipe) diameter, and much larger still than the radar footprint, and even though the position of the pipe was located, its size was exaggerated. However, the discontinuities in the pipe (circled in red in the 1m C-scans), which were confirmed to be caused by leakage or defects, were connected in the 2m C-scans. The post-image computation resulted in an inaccurate visualization of the subsurface situation.

Besides, as the angle between the profiles and a linear object has a significant impact upon GPR response, the choice of suitable thresholds should be discussed from two aspects: the best and worst situation (Xie et al., 2018). In the best case, profiles are perpendicular to a linear object and a larger profile spacing is acceptable. In terms of the worst case, profiles are parallel with a linear object, which means that the response of the GPR will not be obvious enough and a smaller profile spacing is required. If the survey grid is orthogonal, or the angle between the

GPR profiles and the linear object is an acute one, then the suitable range of profile spacing will fall within those of the best and worst cases.

In summary, a suggestion for the selection of a suitable profile spacing is as shown in Rule (a).

$$\begin{cases} PS_{\perp} \leq 6\lambda, & feature\ spacing\ unknown\ or\ inconsistant \\ PS_{//} \leq 4\lambda, & feature\ spacing\ unknown\ or\ inconsistant \end{cases} \quad (a)$$

b. Slice thickness for continuous objects (Box 2 in Figure 3-3)

The stepped steel (SS) specimen was used to illustrate and describe the factors affecting slice thickness selection (Figure 3-6), and a consistent greyscale was maintained for these C-scans. For the stepped steel, the background material is concrete, which is relatively more homogenous compared to a typical underground environment, and the steel bars were evenly distributed.

As shown in Table 3-1, rebars were buried with increasing depth, and the 2nd and the 5th rebars were selected to show the different imaging performance resulting from the variation of the imaging parameters at different depths. It is obvious that the apparent size of the imaged steel rebars was larger with larger slice thicknesses, but slices with a thickness smaller than 1 rebar diameter produced better imaging results, and the size of the imaged rebar is closer to that of reality. In particular, in deeper locations (column (a)) where the GPR signal is significantly attenuated, an excessively small slice thickness results in the mapping of insufficient energy to present a solid object. Conversely, an excessively large slice cannot provide an accurate representation of the object's depth, due to the lack of vertical resolution. In shallower areas (column (b)), the exaggeration of mapped rebar size was less significant than that in the deeper area. The footprint of the GPR antenna increases with depth, but also causes the horizontal resolution to decrease with depth. These two observations illustrate the principle that GPR horizontal resolution depends upon the ratio of object size and radar footprint.
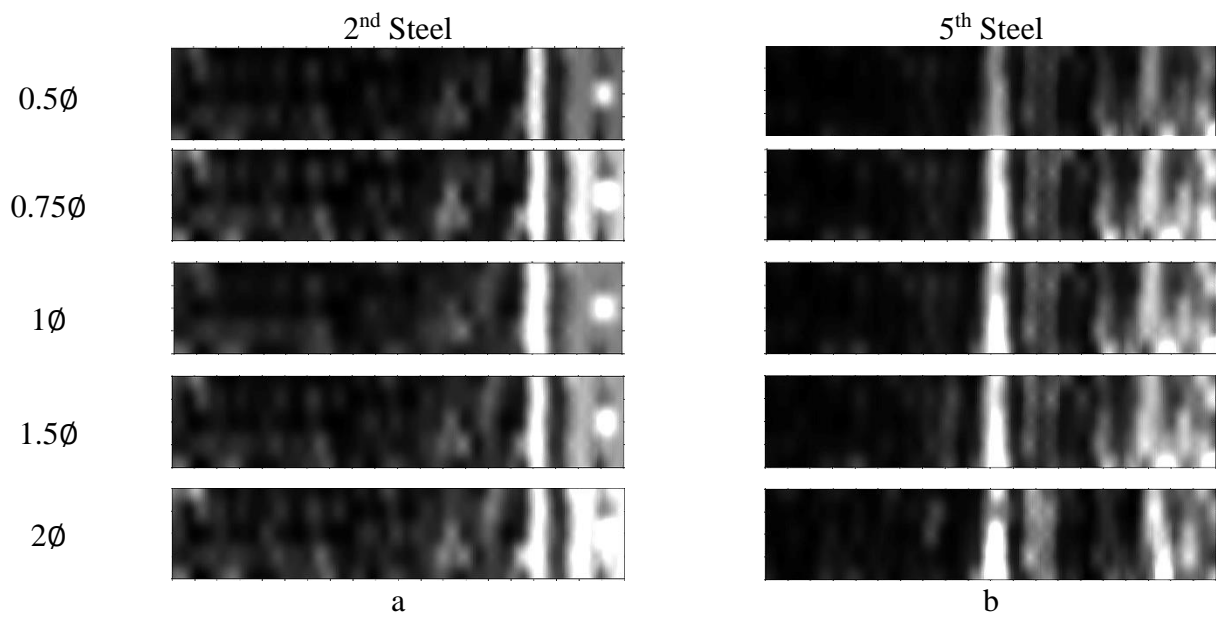
Figure 3-6 C-scans of the steel bar with different slice thicknesses. (a) column: 2nd deep steel bar and (b) column: 5th deep steel bar

Another crucial factor affecting GPR resolution is the radar wavelength. The case of mapping underground utilities in the back lane at PolyU provides a good example for illustrating the choice of an appropriate slice thickness for a known object size and radar wavelength. With the exception of the 2 known utilities buried at the site, there was limited knowledge of the subsurface environment of the entire road (as Table 3-1). The GPR data were collected with positioning provided by an auto-tracked robotic total station. Figure 3-7 illustrates the different C-scan imaging performance with changing slice thickness.

0.5 λ		
0.7 λ		
1λ		
2λ		
	a	b
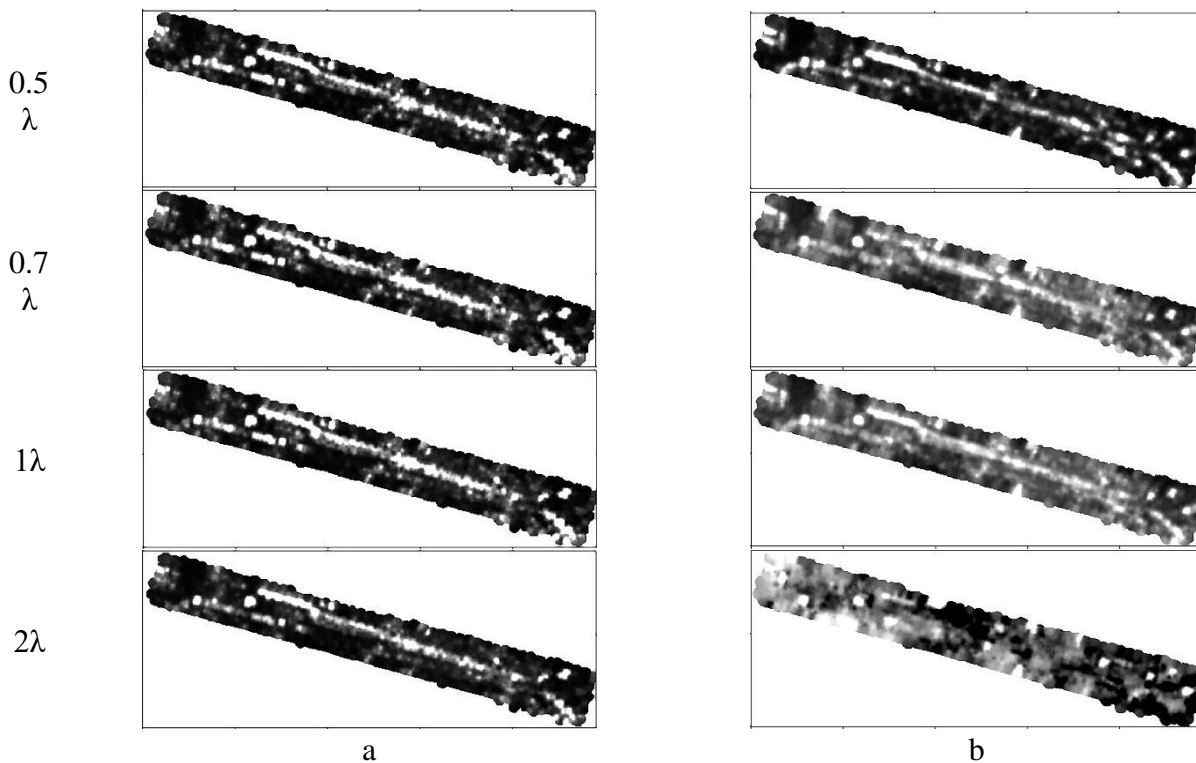
Figure 3-7 C-scans of PolyU back lane of 490MHz from 600MHz antenna (a) and 210MHz from 200MHz antenna (b), with thickness from 0.5λ to 2λ.

As the antenna footprint depends on its frequency (wavelength), the effect of changing the slice thickness produced different results in C-scans obtained from the two frequencies. As illustrated in Figure 3-7, various thickness settings produce similar results when using a higher frequency (600MHz) antenna. With the 200MHz antenna, the image of the utility gradually faded out when the slice thickness was smaller than 1 wavelength. According to Table 3-2, the number of 1λ of 210MHz GPR data was 2 times the estimated pipe diameter, but even 2λ of 600MHz data was much smaller than the pipe's diameter. The imaging results correlate well with Figure 3-7, thus confirming that the slice thickness should not be in the same order of dimension of the object size.

Drawing conclusions from these experiments, a guideline for suitable slice thickness is presented below as Rule (b).

$$\begin{cases} 0.5\emptyset \leq ST \leq 1.5\emptyset, \ feature \ size \ known \\ 0.2\lambda \leq ST \leq 1\lambda, \ feature \ size \ unknown \end{cases} \tag{b}$$

c.   Interpolation for the continuous object (Box 3 in Figure 3-3)

Another observation is that the effects of the interpolation radius on the horizontal resolution is also affected by the interpolation radius applied. In GPR 3D surveys, local interpolation

methods are widely applied to fill up the gap not covered by the survey traverse. When maintaining other parameters and only changing the interpolation radius, significantly different imaging results can be obtained (Figure 3-8). When the interpolation search radius was larger than 2 times the profile spacing, 2 steel bars almost merged into one in the C-scan image. In cases such as the mapping of steel rebars in concrete, attention should be paid to the horizontal distance between 2 targets when defining the interpolation radius, and it should be no larger than the distance between 2 adjacent objects.
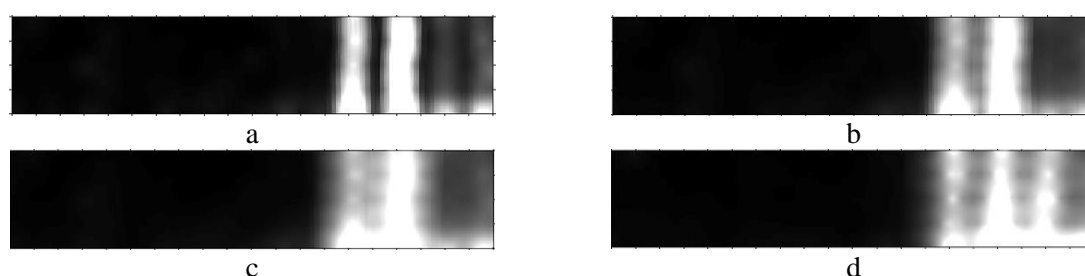
Figure 3-8 C-scans of upper steel bar with different interpolation radiuses (a-d show profile spacings of 0.6, 1, 1.5, and 2 times PS respectively).

The orientation of the GPR profiles has a remarkable impact on the accuracy of the GPR velocity estimation. A profile that is perpendicular to a linear object's orientation provides the most accurate measurements (Xie et al., 2018). If the alignment of a linear object is known, then collecting data perpendicular to it is recommended. For surveys collected in both directions, decoupling cross grid profiles can enhance imaging of linear objects.

The concrete wall (CW) was used as an example to demonstrate the decoupling of cross profiles with linear interpolation. The performance of different search ranges in linear interpolation is shown in Figure 3-9. GPR C-scans are formed by discrete measurements. When the interpolation radius was relatively small – smaller than the profile spacing, artificial gaps were introduced into the linear-shape objects, which made the objects present as disconnect dots. Specifically, the shorter axis refers to the radius perpendicular to profile orientation, while the longer axis represents the radius in line with the profile orientation.
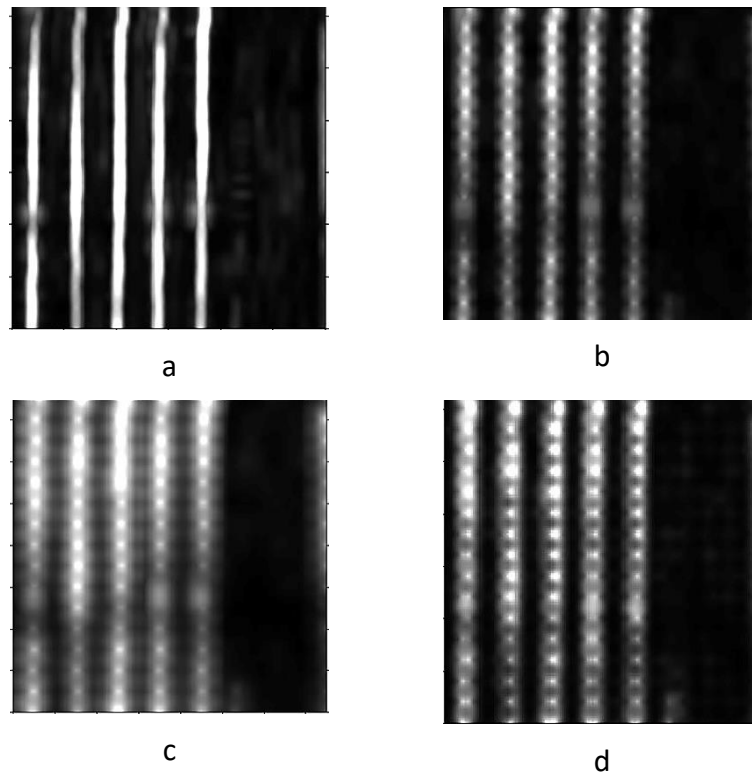
Figure 3-9 C-scans of concrete wall with different interpolation radiuses. ((a)-(d) are $0.2PS_x2PS_y$; $0.6PS_x1PS_y$; $1PS_x2PS_y$ and $1PS_{xy}$ times profile spacing respectively).

Therefore, a guideline for selecting a suitable interpolation radius when mapping linear objects is as shown in Rule (c):

$$\begin{cases} 0.2PS \leq SRx \leq 1PS, & profile\ perpendicular\ to\ feature\ orientation \\ 1.5PS \leq SRy \leq 3PS, & profile\ perpendicular\ to\ feature\ orientation \\ 0.8PS \leq SRxy \leq 1.5PS, & mis-oriented\ profiles \end{cases} \quad (c)$$

3.2.3 Local Object (Path C/D)

Since there is no concern over "connectivity" between GPR survey profiles when imaging local objects, more attention should be paid to estimating the correct size of the object. In view of this desired imaging objective, the emphasis is put on defining rules for interpolation.

 a. **Bilinear interpolation for local objects (Box 6 in Figure 3-3)**

The surface voids created in PolyU's utility laboratory were used to illustrate how local objects can be imaged with GPR. In this case, bi-linear interpolation was applied to allocate an even weighting to measurements in all directions. Figure 3-10 compares the C-scans of surfacesubshallow voids with different interpolation settings. The effect of interpolation radius

on object size was studied using the case of surfacesubshallow voids. For a local object which is not necessary in regular shape, the diameter is not a proper parameter in describing their size instead. Maximum object spread along a GPR traverse is applied to represent the object size.

Whenthe void spread along the traverse is not estimated, it is desirable to apply interpolation with a radius of 0.7-1 times the profile spacing. As demonstrated in Figure 3-10, the imaged voids were closer to their actual spread when a radius equal to half the profile spacing was used, with the achievable horizontal resolution maintained as much as possible. In contrast, the void became increasingly smoothed when the radius reached 1 profile spacing or larger. A proposed rule for imaging local objects is shown as Rule (d).
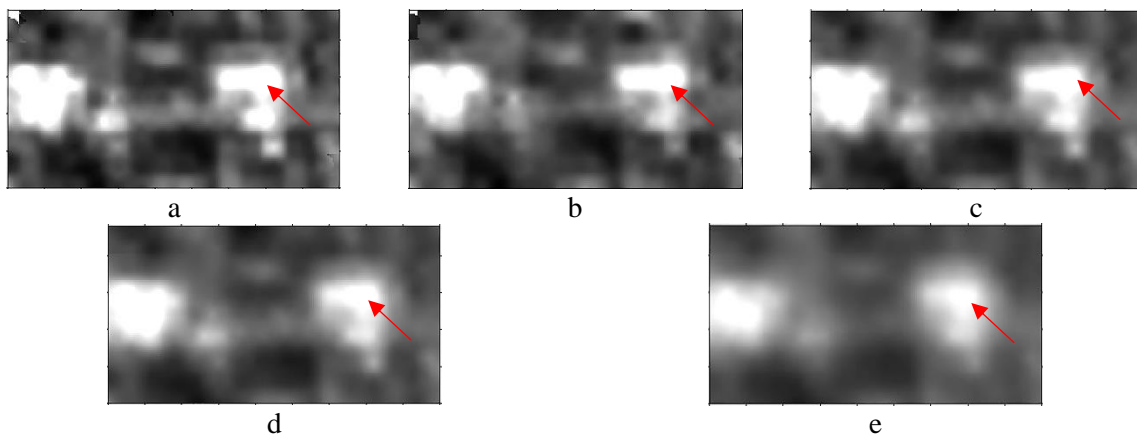
Figure 3-10 C-scans of voids with different interpolation. (a)-(e) are set at 0.5, 0.7, 1,1.5, and 2 times profile spacing, respectively. The red arrow points to the location of a void.

$$\begin{cases} PS < 0.5\Delta \\ PS \leq 3\lambda \end{cases} \rightarrow \begin{cases} 0.5\Delta \leq ST \leq 1.5\Delta \\ 0.2\lambda \leq ST \leq 1\lambda \end{cases} \rightarrow 0.8PS \leq SRxy \leq 1.5PS \ (bilinear \ interpolation)$$

(d)

In addition, owing to the development of auto-track positioning technology — GPR armed with GPS or tracked total-station providing real-time positioning—when mapping large areas, GPR survey can be conducted without the need to follow pre-planned grids. If it is difficult to carry out GPR survey in two orthogonal directions, or no prior knowledge of the object is available, then bilinear or even multi-directional interpolation is recommended to avoid the introduction of artificial reflections. Positioning errors, whether occurring in a grid-guided survey or auto-positioning survey, are systemic errors that are hard to rectify in post-processing.

b. Decouple interpolation for local objects (Box 456 in Figure 3-3)

For more complex situations, for instance, involving the coexistence of linear and local objects about which little is known (survey D), the bottom workflow in the flowchart is proposed. The experimental work at St. John's Cathedral (CA) was used to validate this path. In this case, the GPR survey was conducted in both directions, and linear interpolation aimed at decoupling the two orientation profiles was utilized. Figure 3-11 presents the C-scans resulting from the cathedral survey, with different combinations of the short or long axis of interpolation radius. As there was a linear shaped object on the right of the survey area, it is obvious that a circular shaped interpolation radius performs better in this case.

a   b   c
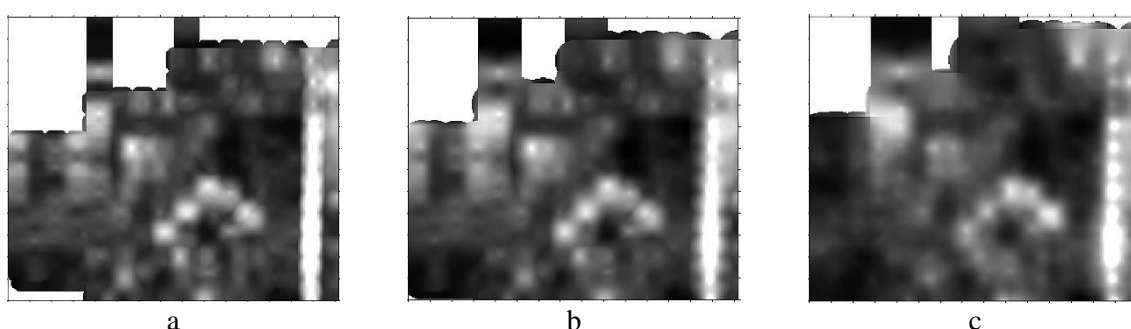
Figure 3-11 C-scans of the Cathedral. (a)-(c) are C-scans at same depth of Cathedral underground with interpolation being $0.8PS_x1.5PS_y$, $1PS_x1.5PS_y$, and $1.5PS_{xy}$ times profile spacing, respectively.

A higher frequency and smaller profile spacing were used at the archaeological site and smaller objects were delineated with higher resolution C-scan images. In this case, although decoupling of two directional profiles and image mathematics were applied, adjacent objects were still distinguishable. When comparing the C-scans of 1xy and 1x2y, the imaging result are very similar, as shown in Figure 3-12. If the depiction of object linearity is not a priority, then the decoupling of GPR profiles of different orientations might not yield a significant improvement in the imaging of local objects. Instead, the size of the interpolation radius has a far more obvious effect on C-scan generation. When the interpolation radius falls within the 0.8-1.5 profile spacing, the generated C-scans do not show a significant difference, which correlates well with rule (d).
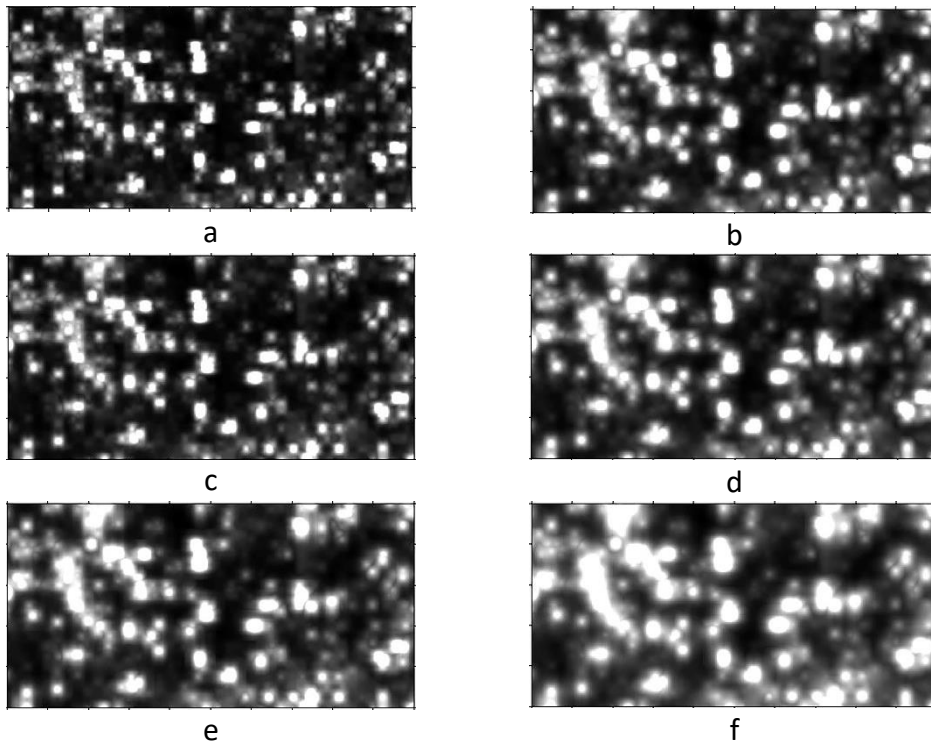
Figure 3-12 C-scans of the archaeological site with different interpolation radiuses ((a)-(f) is 0.6xy, 0.8x2y, 1xy, 1x2y, 1.5xy and 2xy times profile spacing, respectively).

3.3 Discussion on GPR 3D imaging

According to the findings and generalized rules, the process of GPR 3D imaging is object-oriented and the parameters of the process are interrelated. Generally speaking, there is no absolute rule of thumb; instead a thoughtful process, which integrates the physics of GPR imaging with survey operation experience, is required.

3.3.1 Objective-oriented process

The creation of GPR C-scans can be subjective, as the process is a "black box" that interprets and visualizes recorded GPR signals and converts them into semantic images. As a consequence, it is also an objective-oriented process and there are lower and upper range limits for each imaging parameter. Also, the tolerance on the value of each parameter depends on the object being investigated and the intended end user of the survey results. There are also trade-offs between "detecting the object: locating the object's position" and "mapping the object: depicting the object, including its shape and size". The lower limit of a suitable range provides the best imaging results, with the object's geometry being depicted closest to the physical reality. The upper limit of a suitable range does not necessarily result in significantly degraded images, and in some surveys, a degree of image degradation is acceptable. For instance, in the

concrete slab case shown in Figure 3-3, with the help of perpendicular GPR profiles and linear interpolation (box 3 in Figure 3-3), even when a larger profile spacing is utilized, the buried rebar can still be imaged, along with some errors. This was possible due to the idea that only two points are needed to define a line. But if the survey is targeted at the detection of corrosion in a concrete slab, it is not necessary to have each rebar clearly imaged, and a larger profile spacing and lower image quality, reflecting the upper limit of a suitable range, can be applied. In conclusion, some tolerance shall be allowed when defining the suitable range for each parameter, in order to maintain a fit-for-purpose survey while at the same time, the images are still reliable and unbiased.

3.3.2 Interrelated parameters

Though many researchers suggest denser survey profiles, it was observed that when mapping linear objects such as rebar, a coarser profile spacing can still be acceptable. Based on equation (1), when mapping shallower areas, the profile spacing should not be larger than 3 times the radar footprint or wavelength. In this way, the time and cost required to conduct the GPR survey can be significantly reduced (box 1 in Figure 3-3).

In terms of slice thickness, the empirical experiment on rebar in concrete confirmed that the depth accuracy for C-scans is half the slice thickness, and it must be kept in mind that a thinner slice thickness reduces depth resolution errors. In addition, in many civil engineering applications, such as imaging concrete with higher frequency antennas when the targeted reflection intensities are strong, a larger or smaller slice thickness does not necessarily perform well. On the contrary, when working with lower frequency GPR in situations where the object size is comparable to the wavelength, a large slice thickness would result in a blurred image of the object, while an excessively small slice thickness would have insufficient reflection intensity to depict the object. Therefore, it is believed that slice thickness should be determined according to the ratio of known object size to radar footprint. With reference to Table 3-2, the slice thickness of all representative cases was smaller than the radar wavelength, and the most satisfactory results were recorded when the slice thickness was similar to the object's diameter (box 2 in Figure 3-3). Based on these empirical experiments, a slice thickness of at least half a wavelength is suggested when the object diameter is unknown.

Another important imaging parameter is interpolation. If the alignment of a linear object is consistent, then a spindly elongated shaped radius with linear interpolation is suggested, so as

to add weighting to measurements on profiles perpendicular to the object alignment. It is indicated in Goodman (2017) that applying linear interpolation and decoupling cross profiles can provide better images when depicting linear shaped objects. However, if the object alignments are misoriented, or one is mapping a local object, a larger search radius is helpful for eliminating anomalies. However, an excessively large search radius may result in undue image smoothing, while many unnecessary scatterers could be imaged if the radius is too small. Hence, it may be difficult to maintain a balance between retaining true measurements while smoothing tiny local speckles.

3.4 Summary and contribution

In conclusion, the standardized workflow provides a yardstick to systematically standardize the 3D GPR imaging workflow by identifying (1) feature types, (2) profile spacing, (3) slice thickness and interpolation as three key perspectives of GPR 3D imaging after validation of 25 field experiments. The standard workflow also provides a basis for fingerprint database, void's pattern recognition/identifications and change detection presented in the next three chapters.

Chapter 4 Fingerprint database and void pattern simulation
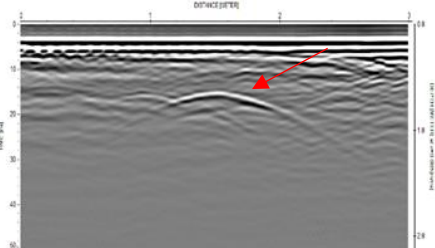
As reported in Chapter.3, a systematic production of C-scans can provide a general overview of the subsurface environment. But during the process of C-scan production, wave characteristics associated with buried features like phase, reflection coefficients and spectral properties of GPR wave reflections are lost. This makes C-scan a screening tool of buried features of interest rather than a tool for interpretations of alignment of utilities and urban subsurface hazards, especially dangerous air voids causing road subsidence. Therefore, for the purpose of interpretation, a fingerprint database with validated GPR responses on a particular type of features presented in this chapter is required, paving the way for pattern recognition in Chapter. 5
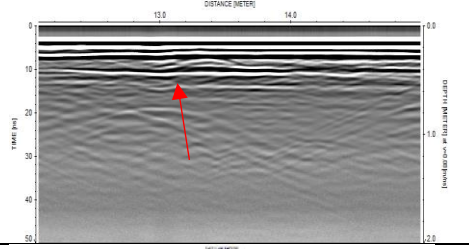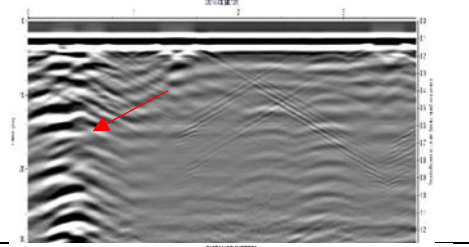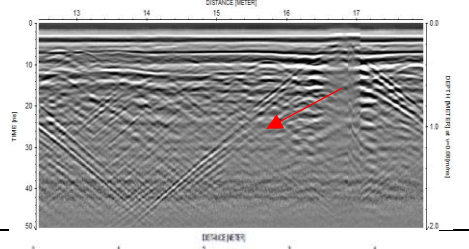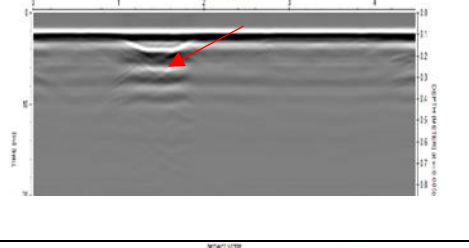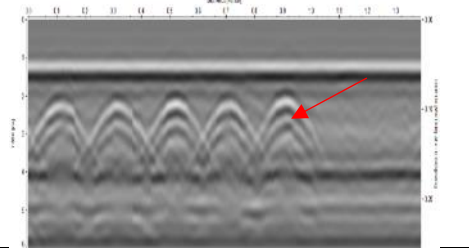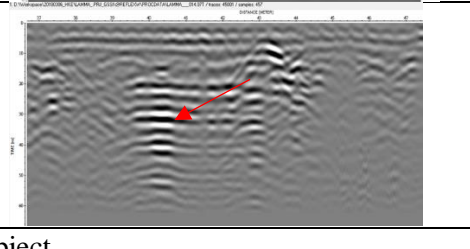
4.1 Fingerprints of GPR responses of typical subsurface structures

Each urban subsurface defects may yield specific GPR responses. GPR responses are affected by multiple factors, including dielectric contrast of two materials, background scattering, the geometry of reflectors. In practice, the GPR reflections from one kind of object are never the same, as the real underground world is very complicated. Therefore, the feature of GPR responses should be characterized.

In order to distinguish defects from a healthy subsurface structure, the GPR responses of "visible" underground structure should be depicted in advance. Typical subsurface structures that can be imaged by GPR, include underground utilities (metallic or non-metallic); subsurface layers (concrete backwall, road pavement/subgrade interface); metallic manhole cover; air void; reinforced concrete; and buried concrete raft/slab/plinth. Table 4-1 summarizes the descriptions and present the B-scans of these typical healthy structures.

Table 4-1 GPR responses of typical subsurface structures

Structure type	Descriptions	Examples
Underground utilities (non-metallic)	When GPR antenna is traversed across an object hyperbolic /parabolic reflection appear in the radargram. If the GPR traverses are perpendicular to the utility alignment, the hyperbolic /parabolic response is the steepest. When the reflection is	

	not interfered by other reflectors or scatterers, the first arrival reflection of a metallic utility is in phase with the direct wave, while that of a non-metallic utility is out of phase with the direct wave. Certain decaying reverberations are expected.	
Layer (e.g. concrete backwall, subgrade interface)	A continuous layer response is present along the radargram.	
Metallic Manhole cover	Strong reflections without attenuation start from the time/ground zero to the bottom of the time window.	
Manhole wall or buried vertical structure	Strong and flat reflections beyond time zero with reflections extended linearly at the two edges of the flat reflection to the sideway.	
Air void	Voids present differently due to the ratio of the void size to the radar footprint. Details on it will be discussed in next subchapter. In C-scans, an air void is present as local anomalies with high reflection intensity	
Reinforced concrete	Strong hyperbolic reflections at shallow subsurface with regular spacing and similar cover depth.	
Buried concrete raft/slab/plinth	It looks similar to large size air-filled void, except the reverberation patterns are more regular to repeat itself in depth.	

Remarks: the red arrows point to the corresponding object.

When the radar wave encounters a defect, the wave travel speed and reflection amplitude or even phase changes, and the GPR responses differently. Taking water leakage as an example, Lai et al. (2016c) found that along with water content increase in hosting material, the amplitude of GPR reflections are firstly reduced than return back to the original level when the material is saturated. showed that if water leakage happens, the wave travel speed is reduced locally at the location where the hosting material is wet.

The hyperbolic reflections from a rebar may be broken or vanish when the rebar is corroded (Bungey, 2004; De Souza et al., 2004; Nojavan & Yuan, 2006). Cracks within concrete structures can be observed with a GPR survey by identifying anomalies (Orlando & Slob, 2009; Panisova et al., 2016; Solla et al., 2014; Vidal et al., 2004).

Some subsurface objects appear quite similar in GPR radargrams. For example, it may be difficult to distinguish air voids from a buried concrete slab, because reverberation appear in both cases. Also, feature with round-shape would generate hyperbola reflection, no matter it is a cross section of underground utilities or a ball-like air void. The manhole that is visible from both surface and GPR data can be used as a reference. Widely GPR application in the various subsurface structure is reviewed and summarized in and Lai et al. (2018a). Pattern recognition techniques can help identifying specific GPR responses from GPR data.

4.2 Standard road structure

In metropolises like Hong Kong, there are multiple facilities buried underneath; they are power, water, drainage, sewerage, lighting or communication and so on (Farley et al., 2001; Lai et al., 2017a; Lai et al., 2016c). Subsurface pipe leakage causes underground wash-out, leaving an air void when water is drained and finally resulting in road collapse when the damaged area can no longer support the heavy load of the pavement structure and its traffic. Over time, countless numbers of air voids develop beneath a city's road network, which threatens the safety of the citizens' lives and property.

Bituminous road and reinforced concrete paved roads are the two most commonly seen pavement structures in Hong Kong. The Highway Department of Hong Kong establishes guidelines on typical road pavement constructions, as shown in Figure 4-1.
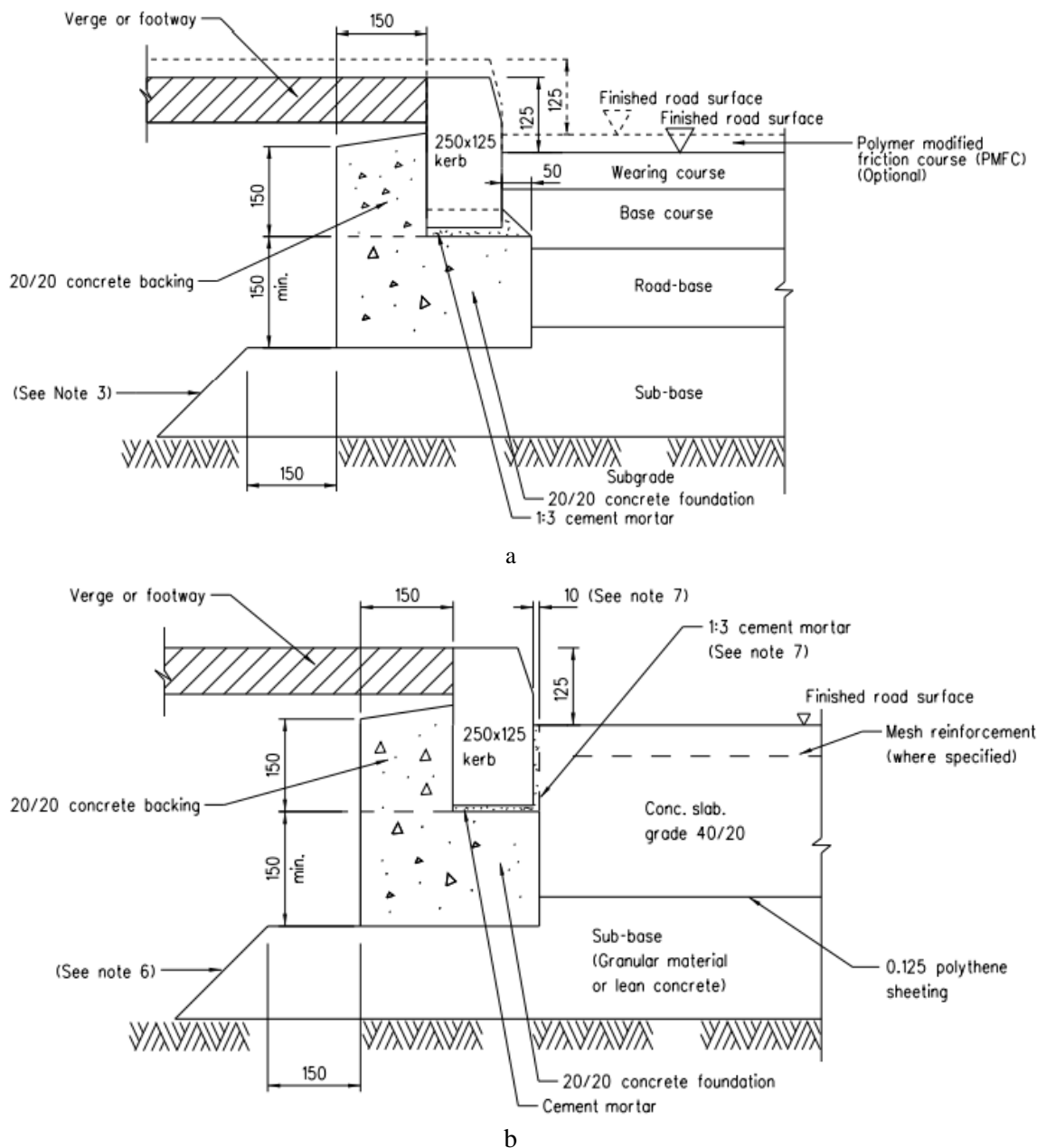
Figure 4-1 Guidelines on typical road structures: (a) is a section of bituminous road and (b) is for concrete roads from Highways Department of HKSAR Government (HyD, 2017a, 2017b)

The structure of the bituminous pavements is comparatively homogeneous. Typical bituminous pavements consist of five layers: 0.04m thick wearing course, 0.065m thick base course, approximately 0.4m thick granular road base, and sub-base and soil subgrade. The above three layers are constructed by bitumen but with aggregates in different sizes: the aggregate size increases along with the vertical depth, ranging from 0.02m to 0.04m. Large aggregate sizes may lead to higher porosity and more blank space among aggregates, but the dielectric properties of each layer shall be very similar.

58

Normally a concrete pavement consists of three layers: 0.3m thick concrete slab where mesh reinforcements are integrated, 0.05m thick sub-base filled by granular material or lean concrete, and subgrade with soils. The maximum spacing of joint reinforcement is 0.3*0.45m in longitude and latitude, respectively, with a top cover around 0.06m thick. Air voids are usually found in the subgrade layer where most underground utilities are buried. Because the joint-mesh reinforcement would generate strong reflection in a GPR survey, distortions on the GPR response of voids in subgrade are expected. In order to model the situation of the voids under roads, the structure of roads must be coherent with the reality. There are standards that suggesting the ranges of several typical materials ("ASTM D6432," 2011; UUS-SPEC, 2019). The complex refractive index model (CRIM) was applied to determine the permittivity of each road layers.

The CRIM as in Equation [4.1], which model the air and water content are considered, is proved reliable in higher frequency(around 1GHz) (Chan & Knight, 2001; Lai et al., 2006). are considered

$$\sqrt{\varepsilon'_c} = S_w \phi \sqrt{\varepsilon'_w} + (1 - S_w)\phi\sqrt{\varepsilon'_a} + (1 - \phi)\sqrt{\varepsilon'_s} \qquad 4.1$$

where ε'_c, ε'_w, ε'_a and ε'_s are real permittivity of the composite, water, air and soil particle, respectively. S_w is the degree of water saturation and ϕ is porosity.

There are two assumptions made in the FDTD simulation in this thesis. Firstly, important material properties: conductivity, relative permeability, and magnetic loss are assumed from values provided in literature ("ASTM D6432," 2011; Cullity & Graham, 2008; NDT.net, 2011), while relative the permittivity was estimated as 11 with the wave velocity (0.09m/ns) of the laboratory data with Equation [2.6]. Permittivity and conductivity of some common materials are defined in Table 4-2. Although aggregate sizes and porosities of each layer are slightly different because percentages of air or water within the layer vary, these effects shall not be significant on the permittivity and conductivity values for material with low water content, such as bitumen and concrete road models. The estimations with CRIM agree with the assumption (Table 4-2).

The second assumption is the rectangular shape of the void. Even though actual air voids are more likely to be irregular. The GPR model in this thesis makes use of voids in rectangular

shape because the elliptical or spherical shapes are not allowed in the simulation software gprMax. Rectangular voids with various length and height were then modelled, with which the sharp border of the voids caused by the collapse of inner material are imitated, as shown in Figure 4-2. Table 4-2 presents the parameters used in the FDTD simulation.

a   b
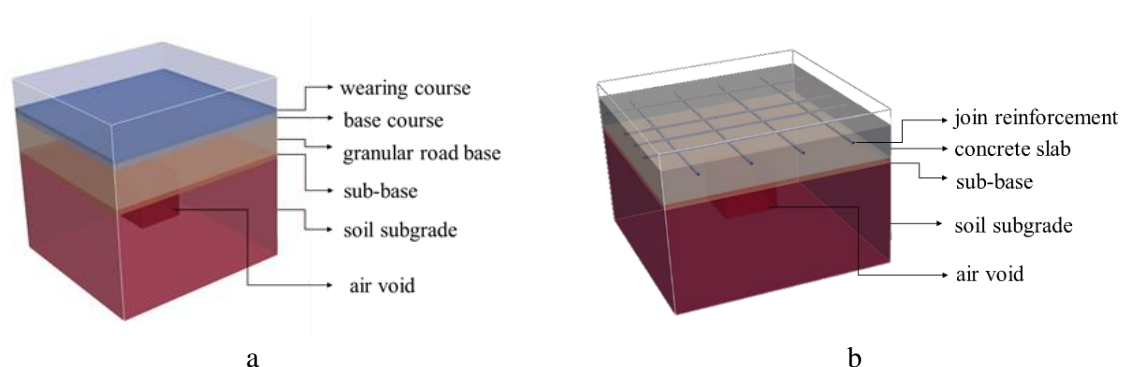
Figure 4-2 Simulation model of two typical road structures: (a) is a bituminous road model, and (b) is a concrete road model

Table 4-2 Parameters of the road models with the FDTD simulation

	Layer	Relative Permittivity	Conductivity	Relative Magnetic Permeability	Magnetic loss	Step size
Bituminous	Wearing course	8	0.05	1	0	
	Base course	9	0.08	1	0	
	Road base	9	0.1	1	0	0.008
	Sub-base	10	0.1	1	0	
	Soil subgrade	9	0.2	1	0	
Concrete	Concrete slab	6	0.001	1	0	
	Sub-base	9	0.1	1	0	0.008
	Soil subgrade	9	0.2	1	0	

4.3 GPR responses of air voids

Air voids are one of the most threatening subsurface defects in urban areas. The strong permittivity contrast between soil-surrounding a void and the air in the void leads to strong GPR reflections. Many researches investigated GPR responses of voids. Xu et al. (2010) used GPR to detect several common subsurface voids, and found cracks - realised as small voids -
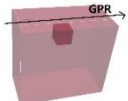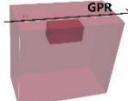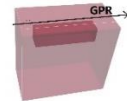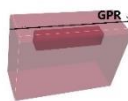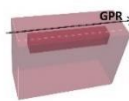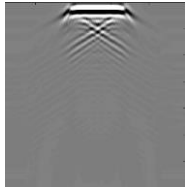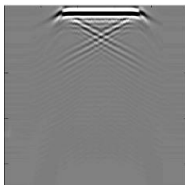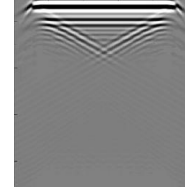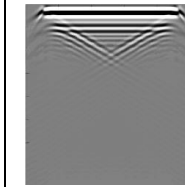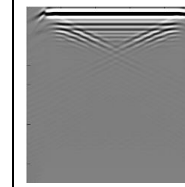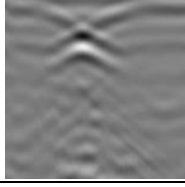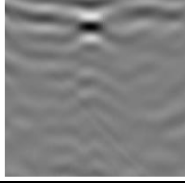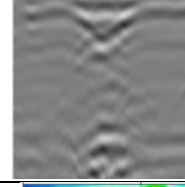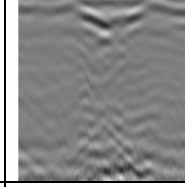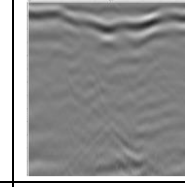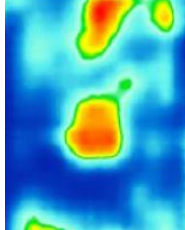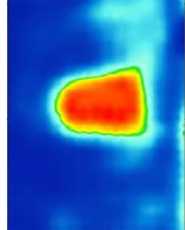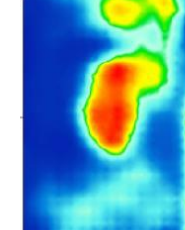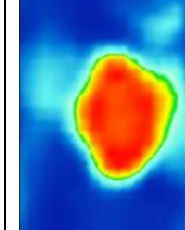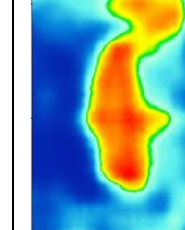
yield hyperbola responses. Lai et al. (2017a) validated the reverberation pattern of voids with three case studies. Casas et al. (1996) illustrated that if the void was very small compared to GPR wavelength, diffracting hyperbolas occur in GPR radargram, while on the contrary, bigger voids generated an irregular signal with chaotic reflections and decrease of the received frequency. Kofman et al. (2006) simulated GPR responses with gprMax and indicated that reverberations happened only when the void size was very large compared to GPR wavelength. It is believed that the strong reflections with reduced frequency are caused by the reverberation of EM wave with air voids (Kofman, 1994).

All these researchers demonstrated that an air void generates special representations in GPR data. The ratio of the void size to the GPR wavelength yields a significant impact on GPR responses how voids with different geometry (size, depth, etc.) present in this way in GPR data is still questionable. There are few types of numerical simulations of the propagation of GPR wave, i.e., ray-tracing techniques and FDTD approach. The former is adopted in GPRSIM, while the latter is used in gprMax and reflexw. As discussed in Chapter 2.2, the FDTD is more suitable for simulating the propagation of the GPR wave, and therefore gprMax is selected in this study. In addition in gprMax, heterogeneous EM properties in each Yee cell can be distributed randomly for simulation of GPR wave propagation in mixing materials, while the inhomogeneous materials can only be represented by the effective dielectric properties in reflexw.

Subsurface voids with varying horizontal spread were created in the Underground Utility laboratory of the Hong Kong Polytechnic University (PolyU) (Wu, 2015). The tank was filled with soil. GPR profiles were collected with an IDS 600MHz system using a 0.1m profile spacing within an orthogonal grid, and C-scans of each void were generated. Meanwhile, gprMax simulations were conducted, imitating the laboratory environment; such that voids of varying horizontal and vertical size were located at a shallow depth (0.1m) within a soil environment. The EM parameters of the model of the laboratory were estimated by the inverse method with the laboratory data: the relative permittivity of the model was estimated as 11 by the wave velocity (0.09m/ns) using Equation [2.6]. The conductivity and the permeability of the model were adopted from the built-in example of the software gprMax. The step size of the simulations was 0.008 – matching the CFL (Equation 2.17) condition but sacrifice certain resolution for the sake of computational efficiency.

Simulated signals were transmitted and received by a 600MHz common offset antenna unit with a 0.15m antenna offset, according to the specification of the IDS 600MHz antenna. The laboratory experiments and simulations produced similar GPR responses. Four typical void patterns were identified in the B-scan data – hyperbola, cross, bowl shape, and reverberation - and these patterns appeared in succession as the void's spread grew, as can be seen in the 5th-6th rows in Table 4-3. In this way, the pattern templates were created in a relatively homogenous environment, free from any interference from other scattering events. In terms of C-scan in the 7th row, voids present as local reflections with high intensity.

Table 4-3 Forward modellings of surface voids with different horizontal spreads in lab

Void spread (VS)	0.4m	0.6m	0.75m	0.1m	1.25m
Simulation model					
FFZ (900MHz)	0.09m				
Ratio of VS-FFZ	4	6	8	10	12
FDTD simulation (B-scan)					
Laboratory experiment (B-scan)					
Laboratory experiment (C-scan)					
Pattern	cross	cross	bowl	bowl	plain reverbration

It is noticeable in Table 4-3, that in parallel with the increase of void horizontal spread, the hyperbolic reflections from the void's edges also become more widely separated. When two hyperbolas overlap, cross patterns occur. Whether two signals can be distinguished depends on

GPR spatial resolution, while GPR horizontal resolution is determined by the footprint of a GPR beam. A narrower beamwidth with a smaller footprint provides a better spatial resolution. There is preliminary research that established a simplified model on horizontal radar resolution, with the relationship between object size and radar resolution (Annan & Cosway, 1992). Equation [2.19] which calculate the FFZ is applied in this study to estimate the radar footprint.

Because the footprint is dominated by wavelength and depth, and the void pattern is wavelength dependent, the footprint is calculated as 0.09m to eliminate the influence of void depth. It is observed that, when the void spread is smaller than r, the GPR response is a point reflection – hyperbola. When the void spread increase to 2-5 times r, a cross pattern occurs in the radargram. The bowl shape pattern presents when the void spread is larger than six times r. When the void spread is significantly larger than the GPR footprint, reflections of two edges of the voids are completely separated, and a plain bottom is presented between the edges. This kind of pattern is named plain reverberation in this study.

However, discrepancies between the simulated B-scans and collected data are observed. The void tops – the upper boundary between the air and the soil – are clearly shown in the simulated B-scan (5th row), but are invisible in the laboratory B-scans (6th row). In the numerical modelling, the effects of the surrounding material were eliminated by subtracting the signal of the surrounding material, as shown in Equation [4.2]. The patterns shown in the 5th row of Table 4-3 present the GPR reflection generated by air-voids only, including the reflection from the upper air-soil boundary. On the contrary, in the laboratory experiments, air voids were dug from the surface of the soils. The phase of the upper boundaries of voids was overlapped with the phase of the ground wave. Since basic B-scan processing – including the background removal – were applied to the laboratory data, the reflections of the void tops were removed. Besides, Mie type scattering in the laboratory B-scans contributes to discrepancies between the numerical simulations and the collected B-scans. Whether these GPR reflection patterns can represent the reality need more justification.

$$reflection\ of\ voids \\ = signal\ of\ model\ with\ void - signal\ of\ model\ without\ void \qquad 4.2$$

4.4 Forward modelling on GPR responses of air voids under the road surface

Ground collapses usually happen on the road surface: busy roads are always suffering heavy loading, and if there are large air voids beneath, the road structure hardly survives. However, in the real world, the subsurface is not as homogeneous as that of the laboratory and previous models. It may be too simplistic to have simple and regular void patterns as the ones presented in Table 4-3. Hence, forward simulations on the voids under road structure were further studied. Two frequencies were modelled in this study: 200MHz and 600MHz, considering the required survey depth is generally less than 3m.

4.4.1 A site experiment on void under road structure

A site experiment was conducted on Shek Mun, Hong Kong to investigate how air voids present themselves in GPR representations (B-scans and C-scans). As shown in Figure 4-3(a), the survey site consists of two parts: a section of concrete paved road and another section of block paved road. The concrete road was strengthened by 0.1m*0.2m mesh rebars (Lai et al., 2018b). In total, six fit balls with various spread were buried at different depths beneath the road sections (Figure 4-3(b)). There are two utilities located across the survey site: a PVC pipe (ø: 0.1m) and a ductile iron (D.I) pipe, (ø: 0.2m) for observing its interference on the signals of the voids.

a   b
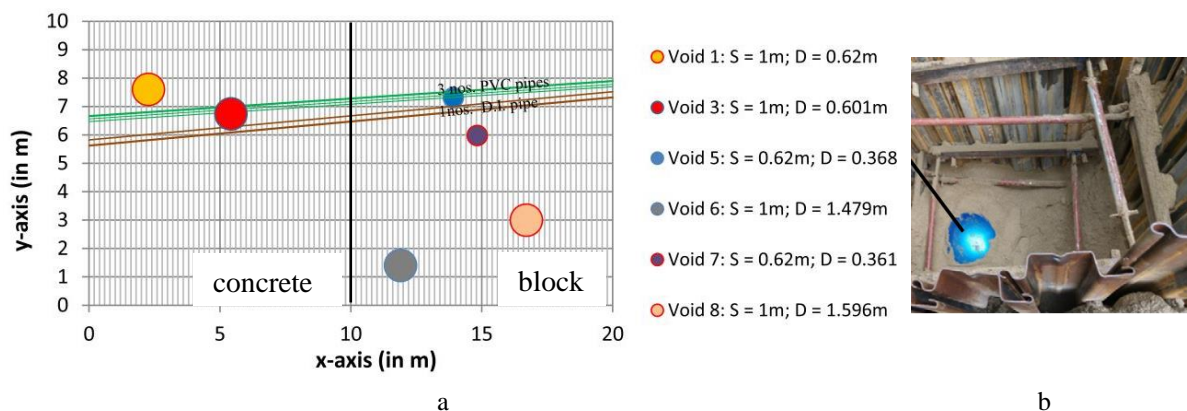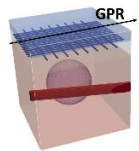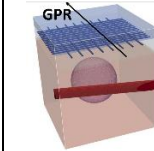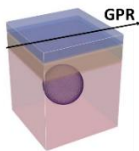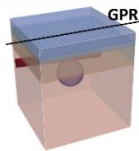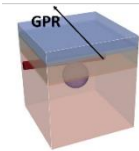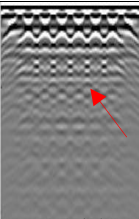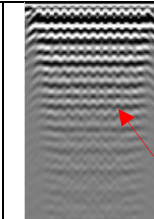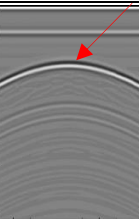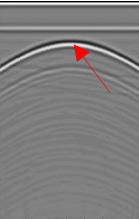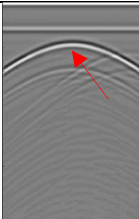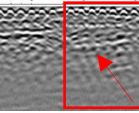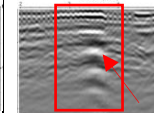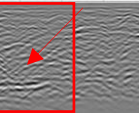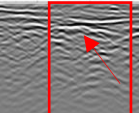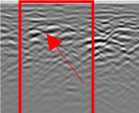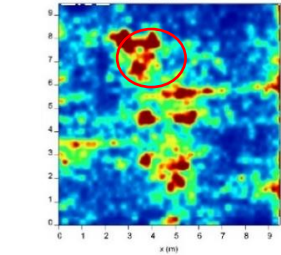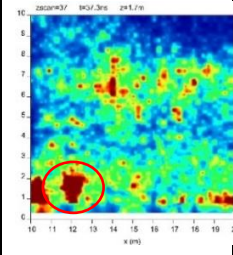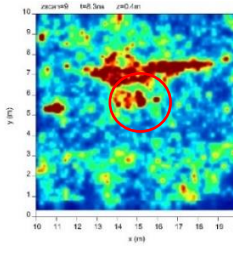
Figure 4-3 Illustration of the site and buried balloons in Shek Mum: (a) is the concept drawing of the site, while (b) is a photo of the buried fit ball.

GPR B-scans were collected by a dual-frequency (600/200 MHz) IDS model, following an orthogonal grid with a 0.25m PS. GPR B-scans were processed according to Jol (2009) and Figure 3-3 to generate C-scans. Three representative fit-balls were selected for further analysis:

64

void 1, void 6 and void 7. Specifically, void 1 was buried under the mesh rebar, void 7 was close to the D.I pipe, and Void 6 was buried in a deeper area (1.479m). The spacing of the mesh rebar in the concrete paved road section was 0.1m. Considering the subsurface voids is often caused by pipe leakage, the effect from the utility nearby on the detection of voids could also be observed.

The underground environment was inhomogeneous and complex at the site, because the survey area was backfilled with the excavated soil, which resulted in disordered GPR reflections compared with the laboratory case (Lai et al., 2018b). FDTD simulations were also carried out to model the GPR radargram of the voids that are free from any other scattering, apart from the road structure and utilities. Simulated models were designed according to the fit balls buried in the site. Fit balls were not buried very deep, therefore only GPR data of 600MHz were applied in this study for the sake of resolution the fit balls. Basic signal processing, like filters and gains were applied to the radargrams. The radargram and C-scans are displayed in Table 4-4.

Table 4-4 Forward modellings on air voids with different horizontal spreads in the site

Balloon	Void 1	Void 6	Void 7
Simulation Model			
FFZ (600MHz)	0.24 m	0.37m	0.19m
Ratio of VS-FFZ	4.2	3	3
FDTD simulation (B-scan)			
Site experiment (B-scan)			
Site experiment (C-scan)			
Pattern	Strong reverberation	hyperbola	hyperbola

Remarks: The dimensions of the FDTD simulations in the 5th row are the same as the red rectangles in the corresponding 6th row: 1.5m long * 1.5m deep. The C-scans in the 7th row present the survey area that was 9m*9m large. Red arrows point to the location of voids.

Table 4-4 is divided into three parts according to the void spreads. Part 1 simulation (the 2nd to 4th row) illustrates the simulation model and simulated GPR B-scans via the calculated FFZ. Part 2 experiments (the 5th to 6th row) presents the B-scans and C-scans after the experiments. Part 3 pattern interpretation (the last row) suggests the type of void patterns are all plain reverberations. The fit balls appear as regular spheres, while the flattened hyperbolic patterns were expected in the B-scans. B-scans of Void 1, both experimental and simulated B-scans, show that the GPR responses were broken into sections by tails of rebar reflections. Besides, it can be observed from both simulated and experimental B-scans that the strong reverberations of GPR responses from void 1 were more obvious than that of the other two voids. The resonant

GPR response generated by voids under the reinforcement last through longer time/depth – coincide with the observation in Table 4-3 and Lai et al. (2017a): that the strong reverberations of GPR reflection of voids decay in the time window. The GPR responses of void 7 presented as flatten hyperbola in both the experimental and simulated B-scans. The interference from the nearby utility was clearly visible in the experimental and simulated B-scans. However, the simulated GPR responses of void 6 located shallower than that in the experimental B-scans. It was possible that the buried depth of the fit ball 6 (void 6) may move in reality after backfill of the upper soils. In contrast to the void 1 in the concrete paved road, the strong reverberation of GPR reflections was not visible in the B-scans of void 6 and void 7 in the bitumen paved road. In terms of C-scans in the 7th row, all three voids appear as local and high reflections, which is coherent to the result of the laboratory experiment.

Besides, the simulation and experiment agreed that the interferences of the road layers were not significant in both experimental and simulated B-scans. Specifically, void 6 and void 7 appear as a continuous and plain pattern. However, in many cases, flat subsurface layers and utilities parallel to the GPR traverse also generate plain GPR reflections. The means to distinguish voids with large spread and utilities is to observe the horizontal length of the plain pattern generated by voids is restricted by the spread of voids which are much shorter in general.

Similar to the reasoning of discrepancies between simulated and experimental B-scans in Table 4-3, the experiment data (B-scans in 6th row and C-scans in 7th) suffer heavy scattering. Mie type scattering, which caused by the reflector's size similar to the GPR wavelength, happened in the complicated and inhomogeneous subsurface world which contribute to the said discrepancies.

4.4.2 GPR response simulations on voids under roads
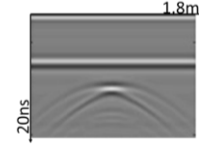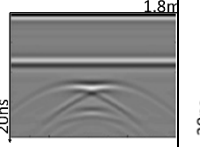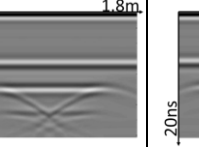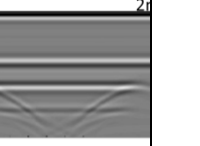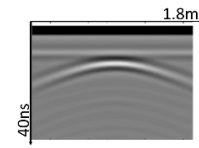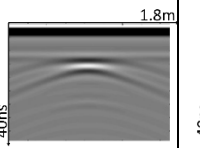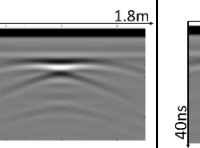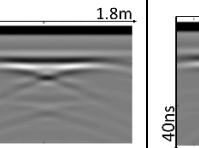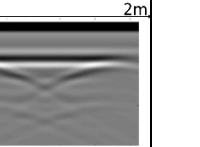
The observations of laboratory experiment and lab simulation are in agreement about the effects of void size on the GPR reflections, while those of the Shek Mun site experiment and the simulation are in line on the effect of the road structure on the GPR reflections. Unfortunately, it is not feasible to dig or bury a number of voids under the road structure in practice, then FDTD simulation can be used to study the combined effect of the void size and the road structure. Based on the typical road structures, GPR B-scans of air voids with different spreads and depths were modelled with the FDTD simulation. The void embedded in models

varies in the horizontal spread – range from 0.2m to 1.8m – while maintaining the 0.5m vertical size.

a. GPR response simulations on voids under bituminous roads

The FDTD simulated GPR reflections of the void under a bituminous road are similar to those of the laboratory environment: similar patterns with particular shapes are presented. The aggregate clusters generate scatterings, but they are not as strong as that of the air void, as shown in Table 4-5.

Table 4-5 Forward modellings on air voids with different horizontal spreads in the bituminous road

Void spread	0.3m	0.5m	0.8m	1.2m	1.8m
FFZ (600MHz)	0.24m				
Ratio of VS-FFZ	1	2	3	5	8
600MHz					
Pattern (600MHz)	hyperbola	cross	cross	bowl	bowl
FFZ (200MHz)	0.51m				
Ratio of VS-FFZ	1	1	1	2	4
200MHz					
Pattern (200MHz)	hyperbola	hyperbola	cross	cross	cross
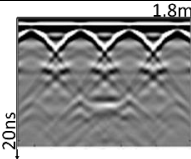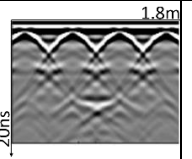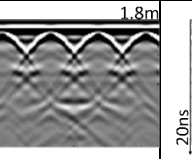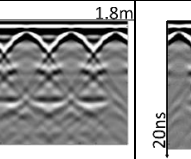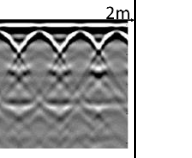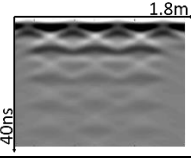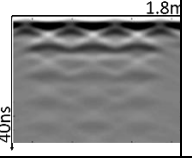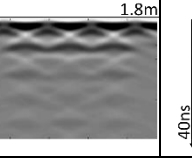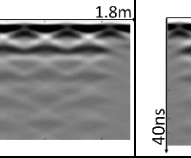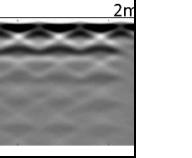
The calculated radar footprint, in this case, were 0.24m and 0.51m for the 600MHz and 200MHz antenna, respectively. These footprints are significantly larger than that of the shallow void experiments conducted in the laboratory. According to the laboratory results based on the shallow voids, a shallow void with spread larger than 0.8m would generate a plain reverberation pattern if the 600MHz signal was applied. But in the bituminous road simulation, the same 0.8m large void generated a cross pattern responses. The vertical location - depth - of voids were different in these two simulations. Thus the GPR footprints, which increase along with the penetrating depth, in two simulations were different. Therefore, it was proven that the GPR responses were related to the ratio of the GPR footprint to the void spread. When the

600MHz signal was applied, a cross shape pattern is expected if the void spread was between 0.4m to 1m, and the simulation results were coherent with this hypothesis. Voids with 1.2m and 1.8m horizontal spread generated bowl shape responses in the 600MHz B-scans. It is consistent with a laboratory experiment that: when the void spread is around 6 times larger than the GPR footprint, a bowl shape pattern was generated.

b. GPR response simulations on voids under concrete roads

The simulations of the GPR response of air voids under the concrete pavements are displayed in Table 4-6. Apparently, the GPR reflection of voids was significantly distorted by concrete rebar on top of it, which is coherent with that of the Shek Mun experiment and simulation in Table 4-4. The reflections from the rebar interfere with the reflection from the edge of air void beneath. In B-scans of 600MHz, the GPR reflections of the top of the void, which is presented as the middle of the GPR pattern, were delayed to a lower time/depth. Then the pattern of the void was more like the bowl shape pattern: closer to time zero at the edges and farther away from time zero in the middle.

Table 4-6 Forward modellings on air voids with different horizontal spreads in the concrete road

Void spread	0.3m	0.5m	0.8m	1.2m	1.8m
FFZ (600MHz)	0.20m				
Ratio of VS-FFZ	1	2	4	6	9
600MHz					
Pattern (600MHz)	hyperbola	cross	cross	undefined	undefined
FFZ (200MHz)	0.44m				
Ratio of VS-FFZ	1	1	2	3	4
200MHz					
Pattern (200MHz)	invisible	invisible	invisible	invisible	invisible
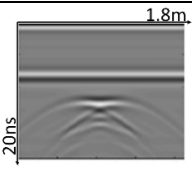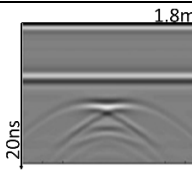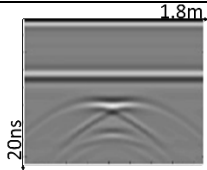
As the void spread increases, GPR reflections of void edges keep separating. But the interference with the rebar responses was too strong that interfere the edge reflections of the

voids, such that the shape of the void responses was seriously distorted compared to the pattern in the modelling of bituminous roads. Although the cross shape and bottom shape patterns were still distinguishable, they were not as clear as that presented in Table 4-3 and Table 4-5. This observation accords with the relationship between GPR footprints and void spread. Also as shown in the B-scans of 600MHz, when the void spread was larger than the spacing of the reinforced rebars, the void reflections become discontinuous, and the original flat shapes as expected in the modelling of bituminous roads are no longer distinguishable. On the other hand, the reverberations of the GPR reflections in the larger depth were much more significant than that in the bituminous road. It also coincided with the observation of the Shek Mun site experiment reported in Table 4-4.

c. GPR response simulations on voids with various thickness

'How thick is the void?' is an usual question for void detection. To further investigate whether voids with various thicknesses would generate a different response in the GPR survey, forward simulations were conducted on the bituminous road model, because the host materials in the bitumen road were relatively homogenous. The horizontal void spread was maintained as 0.5m, and the vertical size of voids was changed from 0.3m to 0.5m. The simulated B-scans are displayed in Table 4-7.

Table 4-7 Forward modellings on air voids with different vertical size in the bituminous road

Void thickness	0.3m	0.4m	0.5m
600MHz			
Pattern (600MHz)	cross	cross	cross

The discrepancy among the GPR responses of voids with different vertical sizes was not apparent. The three simulations in Table 4-7 all showed a cross-shape pattern. But it was visible that, along with the increase of the thickness, the distance between the reflection of the void top and that of the void bottom increased as well. At a depth of the void top, the radar footprint was smaller and yielded a cross pattern. Then, at the void bottom, radar footprint was larger than the responses of two void edges which cannot be separated and thus, result in a hyperbola pattern. These observations are very similar to the reverberation patterns reported in the above

sections. The distinction between the effects of vertical void size and reverberation seems not feasible. Therefore, we do not suggest to estimate vertical void size according to GPR B-scans.

4.5 Discussion on forward simulation and experiments of GPR responses from voids

Through carefully designed empirical experiments and FDTD numerical simulations, the study quantitatively investigates the GPR responses of underground air void with various sizes. Air voids in a relatively homogenous laboratory were used to observe the GPR response and compared with GPR response that is free from scattering. It was found that along with the different ratios of void spread to radar footprint; different patterns would present, and these patterns can be applied as fingerprints for air void identification. A site experiment was conducted to investigate the effect of the road structure on the GPR response of voids. It was found that GPR responses of voids under road structures were highly distorted by the rebars. And air voids under reinforcements present with stronger reverberation. Then two types of road structures: bituminous road and a concrete road were modelled to observe the impacts of void geometry to the GPR signals. In general, the GPR responses can be categorized into four patterns: hyperbola, cross, bowl, and plain reverberation. With knowledge of the GPR response of air voids, the efficiency of void identification can be improved, and the void with its size can be depicted from the GPR data.

The forward modelling from both experiments and FDTD simulations illustrated that subsurface air voids would generate specific GPR responses. The factors that determine how GPR responses look like were quantified.

4.5.1 Two characteristics

1) Horizontal spreads of voids determine the patterns of GPR responses

Comparing the three simulations – in-laboratory, in-site, and modelled roads, it can be concluded that when the void spread along GPR traverse is very small, for instance, less than the radar footprint; the hyperbola shape reflection is generated because of the air void acting similar to a point reflector. When the void spread increases to 4-6 times the GPR footprint, the GPR response of the air void appears as a cross shape pattern, because the reflection of two edges of the air void is neither coincided nor totally separated. As the void spread increases to more than 6-8 times of the radar footprint, the reflection of two void edges are completely

separated, and the middle of the void gradually shows up, so a bowl shape pattern appears. If the void spread along the GPR traverse is very large, plain and persistent reverberation pattern occur. An illustration of the relationship between void spreads and radar footprint is shown in Figure 4-4. It suggests the appearance of void in B-scan depends on not its physical spread but also the radar footprint which is controlled by three factors: (1) void depth; (2) antenna frequency and (3) wave velocity.
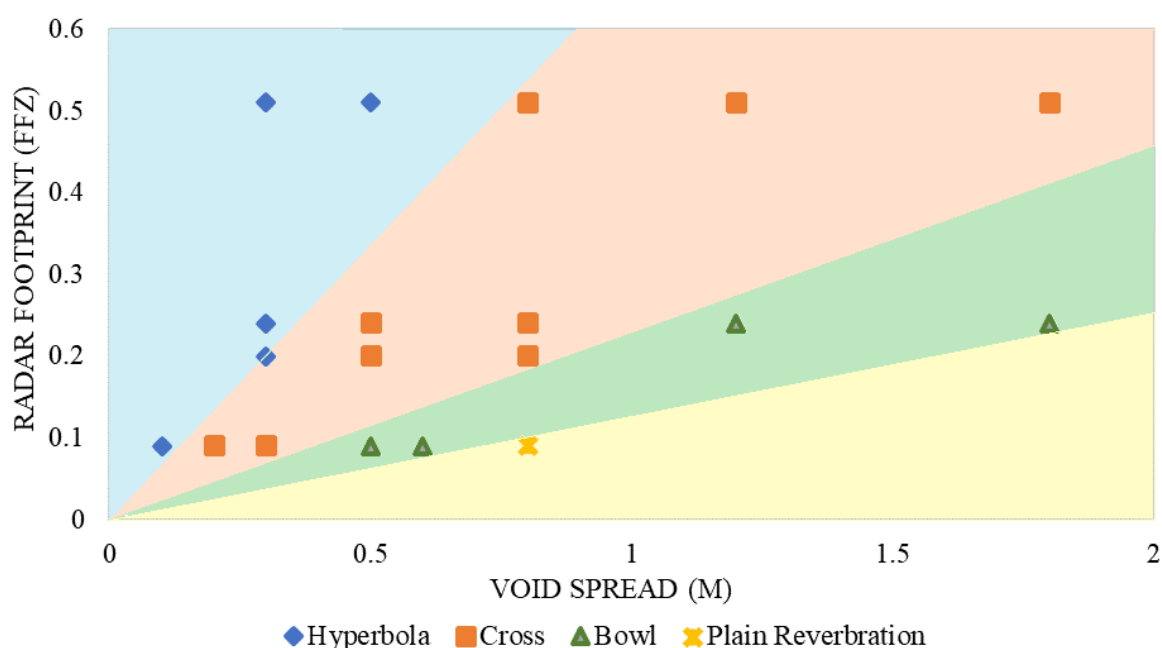
Figure 4-4 A summary of simulations on the relationship between void spreads and radar footprint

2) The road structure influences the GPR reflections of voids

DBoth site experiment and FDTD simulations illustrated that the mesh rebar in the concrete pave road distorted the GPR reflections severely. The shape of GPR reflections of voids was broken by the reflection of the mesh rebar. The typical patterns, like hyperbola, cross, bowl and plain reverberation in the rebar-free environment as in bituminous road, were hardly distinguishable. It is because the GPR wave could not penetrate the metallic rebars, yielding a non-void reverberation ringing between the antenna and rebars. Thus the voids were presented as the discontinuous yet heavy reverberation in the B-scans of the concrete road. In contrast, the reverberation did not exist in the bituminous road because of the absence of rebars. Besides, the different road layers did not manifest a significant impact on the GPR reflections as the dielectric properties of each road layers were similar as predicted by the CRIM calculation.

4.5.2 Two limitations

3) Heavy scattering in the subsurface

Discrepancies are inevitable between experiments and simulations, as shown in Table 3 of the Shek Mun experiment. In practice, the underground environment could be much more complicated. Mie scattering caused by unexpected targets with a size comparable to GPR wavelength is often observed in real practices. On the other hand, the simulation models are assumed to be relatively homogeneous. In the roads surveys, there are many underground utilities buried underneath, which also generate GPR responses and distort the response of air voids. Without convincing real data with ground truth results, it is difficult to prove the validity or practical applications of these simulations with confidence. Yet, they form an indispensable basis for building forward models in more complicated scenarios, and then pattern recognition for decision-making of void or no-void during any void survey.

4) The geometry of voids and the source of excitation

Firstly for the geometry of voids, the shape and geometry are hardly known. In this study, only regular shape, or more explicitly the spheres and rectangles of voids (with the surface roughness of the void-soil interface) were considered for the sake of computation efficiency and simplicity. Secondly for the source of wave excitation, the energy in FDTD was excited from a point source, while in reality, the GPR signal was emitted from the antenna (with certain width).

4.6 Summary and contribution

This chapter defines the effects of void size on the GPR B-scans. These typical patterns can serve as a guideline for operators to detect the invisible and shallow subsurface voids. Through recognizing anomalies through C-scans generated by the established workflow in Chapter. 3, and categorizing GPR response in this chapter, preliminary judgments on the void existence and void size can be defined from the GPR radargram. Then a database of void patterns was constructed for the pattern recognition to be reported in the next chapter.

Chapter 5 The void identification with pattern recognition

When the preliminary knowledge on how the targets look like in the GPR data are available, targets can be located and described with intelligent pattern recognition techniques, and hence the efficiency and effectiveness of void identification. Currently, GPR data are mainly analysed with visual interpretation. For the large-scale survey, it may take days before a result can be obtained. A semi-automatic workflow is introduced for diagnosis of subsurface void in this Chapter. Having reviewed the application of pattern recognition in GPR surveys (Chapter 2.4.1), the pyramid method was adopted. The workflow integrates the pyramid pattern recognition method and Otsu's image segmentation commonly adopted in remote sensing. A laboratory and a site experiment are applied to validate the workflow.

5.1 A semi-automatic workflow for the diagnosis of air voids

A workflow that integrates pattern recognition technique, is developed in this sub-chapter for semi-automatically diagnosis of subsurface air voids.

The workflow imitates the human judgment process and integrates a pyramid pattern recognition technique in order to search for GPR responses generated by air-filled voids. Two validation experiments were conducted and produced promising results. Known voids were successfully identified, although some errors existed. The developed workflow includes 3 stages: 1) roughly locate the void and estimate void size from a C-scan; 2) inspect the corresponding B-scans across the suspected void location and estimate the void size based on the typical patterns developed in Chapter 4; and 3) cross-validate the results of the two previous stages, and select the most convincing void size and void material, while giving priority to the C-scan image. The detailed workflow is shown below in Figure 5-1:
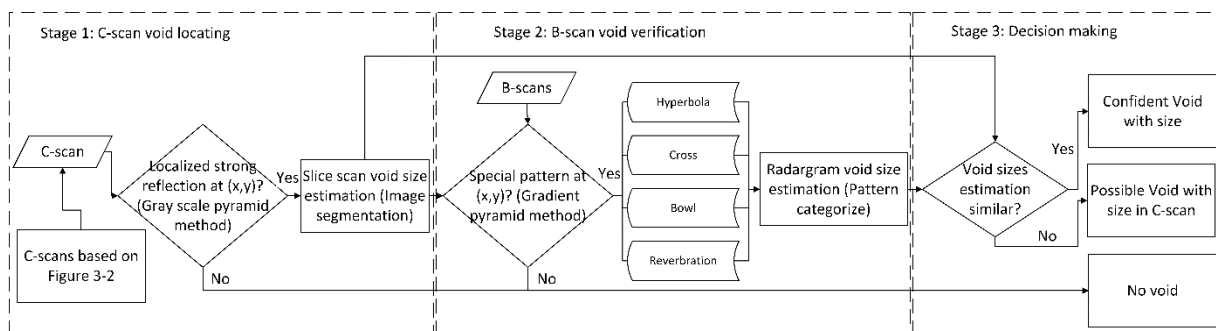
Figure 5-1 A 3-stage pattern recognition for void identification

Stage 1: Void locating from C-scans.

C-scans provide a general but intuitive view of the subsurface. Given that the dielectric properties of air and the garden soil host medium are different, the GPR reflection intensity of voids, which the C-scan is mapped, is often strong enough to be visible. It is therefore relatively straightforward to establish the approximate position of air voids within a survey area. Furthermore, any suspected voids in C-scans can be extracted using the image segmentation method. The size of the void is estimated by multiplying the scale of the pixel size to the ground distance and by counting the number of pixels.

Stage 2: Void verification by B-scans.

C-scans only provide information based on the normalized reflection intensity. Many kinds of local reflectors may generate similar patterns in C-scans if they have similar dielectric properties. A further verification using B-scans is therefore essential. Given that B-scans display the full GPR waveform, and subsurface voids generate reverberation-like responses, confidence can be enhanced by examining whether a localized response occurs in the suspected void's position. Since different void characteristics, such as sizes and materials, may yield various reflection patterns, a void's description can be estimated.

Stage 3: Decision making.

In this stage, two sets of results (from C-scan and B-scan) are presented and compared. A void is most likely to exist when it is identifiable in both C-scans and B-scans. In addition, further evidence is provided if the void size estimations in the 2 previous steps are similar. In this case, C-scans and B-scans both support the same decision and hence the highest identification confidence is given to the void. On the contrary, if no void pattern is found in B-scans that corresponds to the location of a suspected void in C-scans, then the anomaly may result from another kind of reflector. If a void is found in both C-scans and B-scans, but the sizes estimated by the two steps are significantly different, then the size estimated from the C-scan is adopted. This is because C-scans offer an overall perspective view of the survey area, while B-scan estimation relies entirely upon the void's spread along the profile section.

According to the designed workflow, it is critically important to define whether a specific void pattern is identifiable in the data. The pyramid method is applied in this stage in order to conduct automatic pattern recognition. In alignment with the workflow, as a decision-support program, integrating automatic void recognition from both C-scan and B-scan data, was developed with LabVIEW. LabVIEW is "a system design platform and development

environment for a visual programming language from National Instruments" ("LabVIEW –
See it. Solve it.s," 2018).

5.1.1 Automatic pattern recognition using the pyramid method

As discussed in Table 2-3, due to its developmental maturity and computational efficiency, a
much simpler pyramid-based pattern matching approach is explored in this study. The flexible
template of pyramid-based matching is also more suitable for the detection of subsurface voids
of various shapes. This study was therefore aimed at developing a semi-automatic subsurface
air void identification workflow using pyramid pattern recognition.

In stage 1 and stage 2 of the workflow, pattern recognition is conducted in both C-scans and
B-scans using the pyramid-based pattern recognition method. The pyramid-based method is
integrated within the LabVIEW system. It was observed that the greyscale pyramid method
performs best for void identification in C-scans, while the gradient pyramid is more suitable
for B-scan pattern recognition, through experiments validation. Pattern recognition includes 2
phases: the learning phase and the matching phase.

(1) Phase 1: learning phase

Firstly, the pixels of both data images and template images are re-sampled to construct the
pyramid. The resolutions of both data images and templates are reduced to 4 lower-resolution
levels using Gaussian pyramids. In any single Gaussian pyramid, the original image is
continually convolved and sub-sampled in one-octave steps with a Gaussian kernel, then the
resulting image of this process is a low-pass filtered copy of the original image (Adelson et al.,
1984; MacLean & Tsotsos, 2008). The image size in one level higher is a quarter to the image
in one level lower. This process is repeated 4 times to obtain a sequence of smoothened images,
which constitute the representation model built in the learning phase (Figure 5-2). The pixel
values of the data pyramid and the template pyramid are the essential image information. Two
kinds of image information can be used to compute pixel values: grayscale values representing
GPR reflection intensities, and gradients that describe the pattern geometry and edge
information. In C-scans (stage 1), the grayscale values, which means the intensity in C-scans,
is applied, while in B-scans, the gradient, or the derivative of intensity is used (stage 2). A
description of the pattern with the essential image information, including the region of interest,
is then constructed. Next, in the matching phase, the algorithm searches for specific patterns
within a data image.
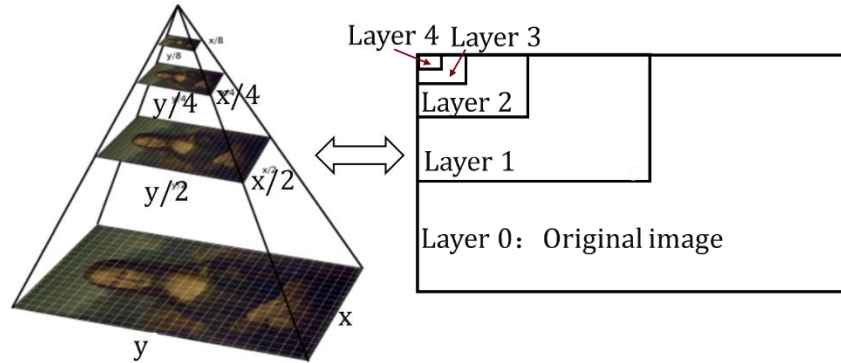
Figure 5-2 the illustration of image pyramid. x is the image width while y is the image length.

(2) Phase 2: matching phase in Figure 5-3

The algorithm conducts pattern similarity computation with a coarse-to-fine approach, whereby the search starts from the highest pyramid level – level 4 which has the lowest resolution. Since the pyramid representations are built for both template images and data images during the matching stage, the template image in this level is moved around the whole data image of the same level, then the degree of similarity between the data level and the template level is then estimated. The similarity is repeatedly computed along with the movement, until the desired score – the matching score (to be discussed in Chapter 5.3) is achieved. If in this level, the similarity of the whole data image is lower than the matching score, the whole process is repeated in the lower level which has a higher resolution, until the searching process is finished at all five levels. This process is illustrated in Figure 5-3The process is demonstrated in Figure 5-3.

When searching for rotated matches, a coarser angle is preliminarily adopted, and then the rotation is refined with smaller angle step sizes ("NI Vision - Pattern Matching Techniques," 2018; Pavlidis, 2013). Since templates are analysed across all pyramid levels, the approach is scale and angle invariant.
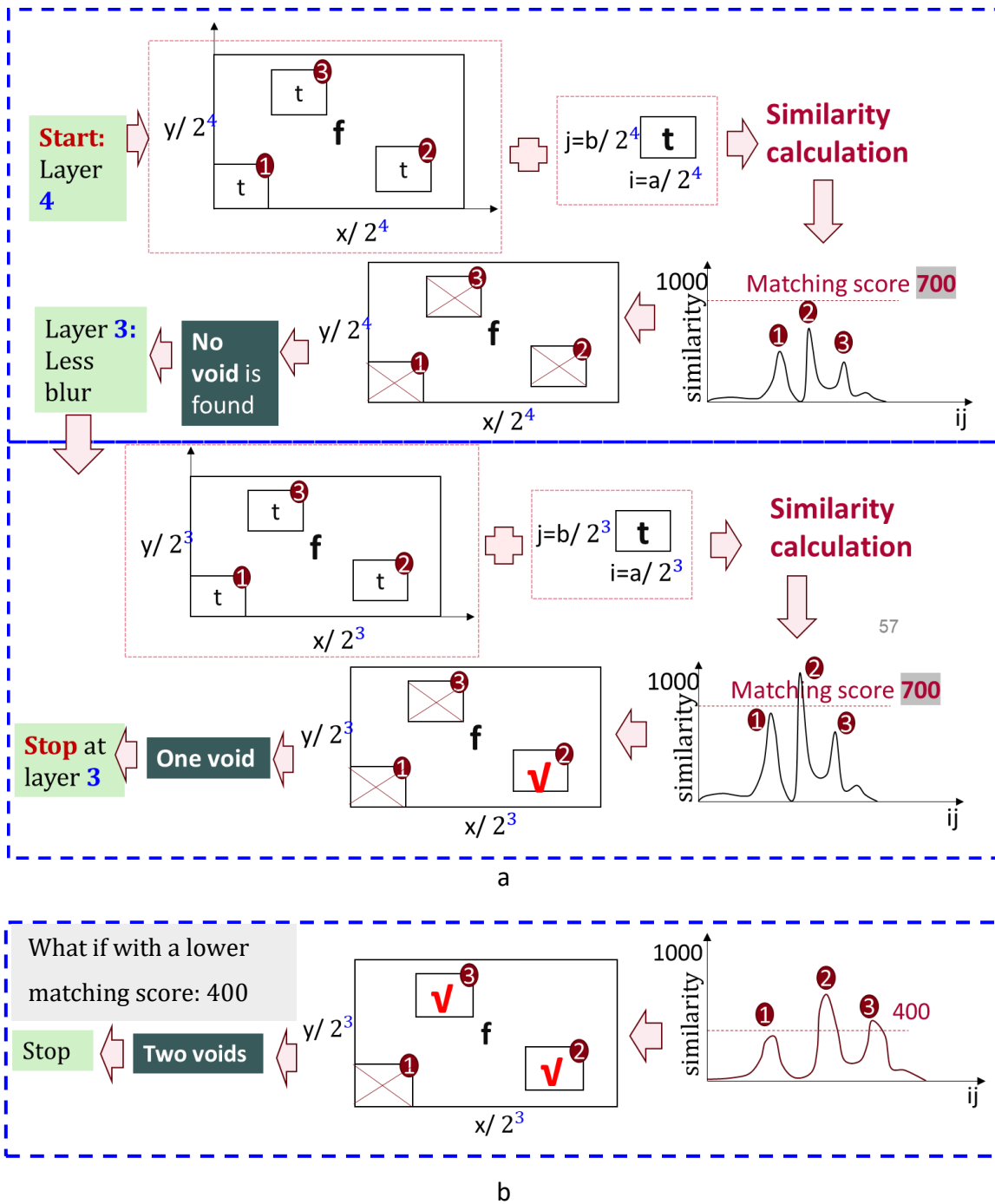
Figure 5-3 Coarse to fine approach for matching template pyramid with data pyramid. (a) is an example of the matching process that starts from level 4, with a matching score as 700. (b) is an example illustrating that more areas are considered as voids when a lower matching score is applied. Remarks: t is the template image with size as (a, b), f is the data image with size (x, y), at certain level, the image size is decreased to (i, j),

(3) The calculation of the similarity

In the matching phase, the similarity between the data and the template is calculated. But then image information used in stage 1: C-scans and stage 2: B-scans are different.

• In stage 1 of the workflow: C-scans, where the greyscale is considered as the image information, the normalized cross-correlation (NCC) is calculated to establish the similarity between the template and data images, as shown in Equation [5.1]:

$$C = \frac{1}{n}\sum_{x,y}\frac{1}{\sigma_f\sigma_t}\left(f(x,y)-\overline{f}\right)\left(t(x,y)-\overline{t}\right)$$

[5.1]

where C is the similarity, n is the number of pixels in the template image $t(x,y)$; $\overline{f}$ and $\overline{t}$ the average pixel values of the data image $f(x,y)$ and template image $t(x,y)$; σ_f and σ_t are the standard deviation of f and t.

It should be noted that the correlation is computed based on a template image that should be smaller than the data image.. Therefore, the greyscale pyramid method places emphasis upon the distribution of normalized pixel grey values. It is helpful when the pattern presents as a specific greyscale shade but has no particular shape or sharp edges. As a consequence, the greyscale pyramid is sensitive to change of brightness. As discussed in the previous section, air voids present as regions with locally high reflection intensity, which occurs due to the comparatively significant reflection contrast between an air void and the host material, and, thus the greyscale pyramid method is more suitable for C-scan detection.

• In stage 2 of the workflow: B-scans, the gradient is used as the image information, vector correction is then applied to calculate the similarity between the template image and data image. The vector component of images describes the gradient direction of each pixel. The vector correlation calculation is shown in Equation [5.2]:

$$C = \frac{Cov(t,f)}{\sigma_t\sigma_f}$$

[5.2]

where C is the similarity index, $Cov(t,f)$ is the covariance between template image $t(x,y)$ and data image $f(x,y)$, and σ is the standard deviation of f.

As the gradient pyramid focuses on filter edge vectors, it is more suitable for templates that have a clear structure and obvious edge. Even though it is insensitive to an intensity change, the gradient pyramid demands higher image resolution, because the strength and reliability of edges are reduced at very low resolutions. As discussed above (Chapter 4), for pattern recognition in B-scans, changes in void sizes lead to different GPR response patterns. These

patterns mainly differ in terms of their shapes and structures, and in this case, the gradient pyramid possesses better recognition performance.

5.1.2 Image segmentation with Otsu's method

As shown in Figure 4-4, void size is estimated from C-scans using the image segmentation technique in stage 1 of the workflow. Unlike traditional remote sensing images that are composed of multiple bands, GPR C-scans present only single band reflection intensities. In addition, due to the diffraction of GPR signals at the edges of an object, its boundary is not necessarily sharp in GPR C-scans. Histogram thresholding, therefore, is the most straightforward approach for object extraction from C-scan images. There has been much research conducted on image segmentation, including the following: Laplacian and gradient counts of greyscale values focused upon the identification of maximum degrees of difference (Gou et al., 2013); Gaussian determination of edges based on image frequency (Permuter et al., 2006); and K-means and Otsu's clustering-based threshold definition (Lee et al., 1990). Among these, the Otsu's method is adopted in this study for its computational efficiency. Besides, Otsu's method evaluates global image pixel value distributions, which requires no preliminary knowledge of the object reflectance, while, in contrast, some other methods take adjacent pixel values into consideration.

Otsu's method is clustering-based and is widely used to conduct image segmentation in an automatic and unsupervised manner (Sezgin & Sankur, 2004). The objective of image segmentation is to define the threshold at which pixels can be classified into two groups: foreground pixels and background pixels (Lee et al., 1990). The algorithm firstly computes an image's histogram and probabilities for each intensity level. When two initial classes are established, the algorithm iteratively computes the class mean and class probability. Then an optimum threshold can be obtained through minimizing the weighted sum of within-class variances in order to calculate the maximal inter-class variance (Otsu, 1979; Sezgin & Sankur, 2004). More details concerning the algorithm can be found in Otsu (1979).

In addition to the tail of the GPR response generated by a buried object, a coarser profile spacing and interpolation in the C-scan processing would also both lead to an imaged object appearing to be larger than its real size. Therefore, image erosion using a 6*6 structure element is also introduced during image segmentation. The size of a structure element is defined based upon the resolution of GPR C-scans: given that the spatial resolution of GPR C-scans is

normally within centimetres, the structure element should not be larger than the size of the smallest detectable objects, otherwise they might be removed from C-scans.

5.1.3 Inverse modelling: Cross validation and decision-support system

The interface of the designed workflow prototype is shown in Figure 5-4. In the designed LabVIEW interface, three stages of void identification workflow are separated into three sub-interfaces. Based upon the simulations and experimental results in Chapter 4, two databases of void patterns for C-scans and B-scans were constructed, as shown in Table 4-2.
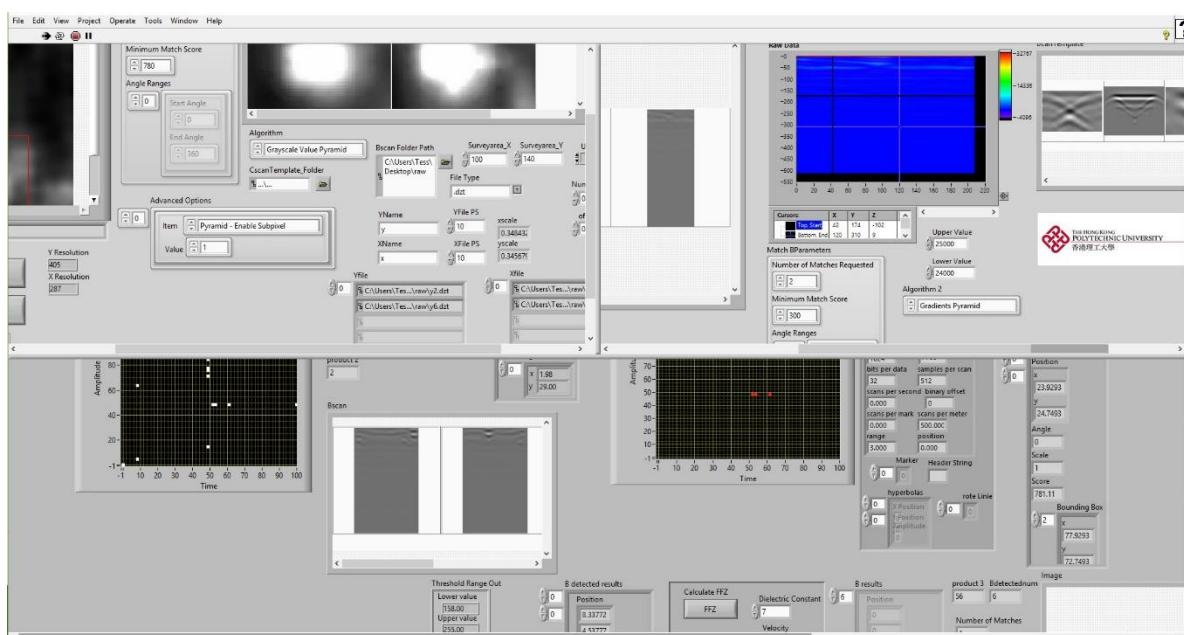
Figure 5-4 Illustration of the interface of designed workflow prototype

For stage 1, the C-scan surveyed corresponding to the suspected void's depth is the input, and the greyscale pyramid method is selected as the desired algorithm. The program retrieves void patterns from the C-scan database and searches for the optimal match. As discussed in Chapter 3.2, the similarity is computed between the template and the inputted data image. The matching score then filters out results with lower similarity. Through numerous experiments, it was possible to demonstrate that abnormal reflections in C-scans were easily detected with the higher similarity, so that a higher threshold – above 700 out of 1000 – on the matching score is preferred if an optimal matching result is desired. This is because in C-scans, reflection scatters may frequently occur, and they are very unlikely to present an identifiable structure.

Having input the survey grid information, as shown in Figure 5-5 (a), the C-scan image is georeferenced and the coordinates of pixels are transformed into a real world coordinate system.

The position of a void in terms of a real-world coordinate system is thus defined and can be displayed in a plan, and the estimated and void sizes in the real world should match. With the help of Otsu's method (inter-class variance), the void's edges are computed based on the histogram distribution. A bounding box depicts the whole area of the detected void and the centre of the bounding box refers to the centre of the void. The radargram profiles that are closest to the centre point are indexed. For each void, two radargram profiles are selected for a gridded survey using x and y direction GPR survey profiles. These selected radargrams are then read and transferred to pixel-image format for further B-scan pattern recognition.

a   b
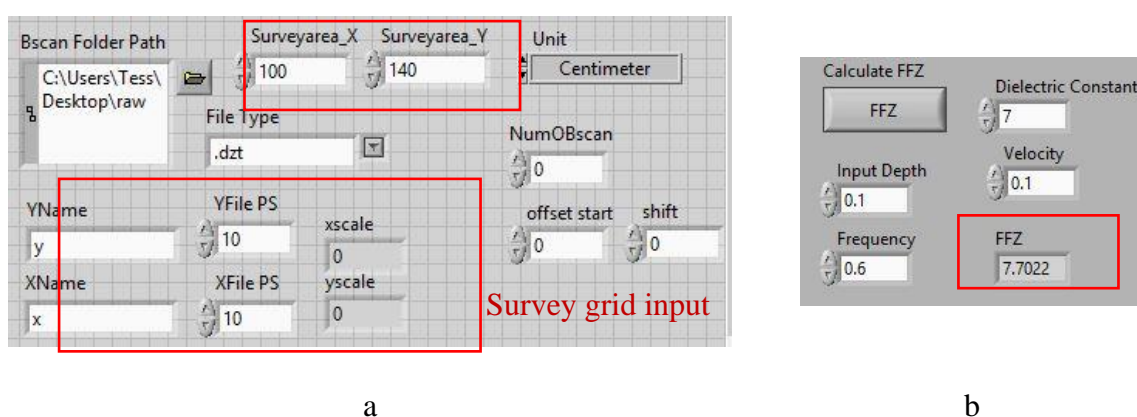
Figure 5-5 The input interface of the survey settings. (a) presents the survey grid information setting interface while (b) shows the interface of the radar footprint calculation

In the B-scan verification step (stage 2 in Figure 4-6), the approach is mainly the same as that adopted for identifying the void locations in C-scans, except the gradient pyramid method is adopted when matching patterns. For each selected B-scan, the B-scan patterns are matched in the database one by one in order to find a match. The GPR reflection is affected by various factors, such as adjacent reflectors, profile orientation, and material properties. It is therefore difficult to have templates that match with GPR responses. Therefore, a lower matching score – 200 out of 1000 for instance – is suggested to avoid missing patterns. For all detected patterns, only those falling within the bounding box defined by the C-scan pattern are considered valid. The detailed flow of this loop is shown in Figure 5-6. According to the regularity of the GPR response on air void, as discussed in Chapter 4, void spread along the direction of the radargram profile is estimated.
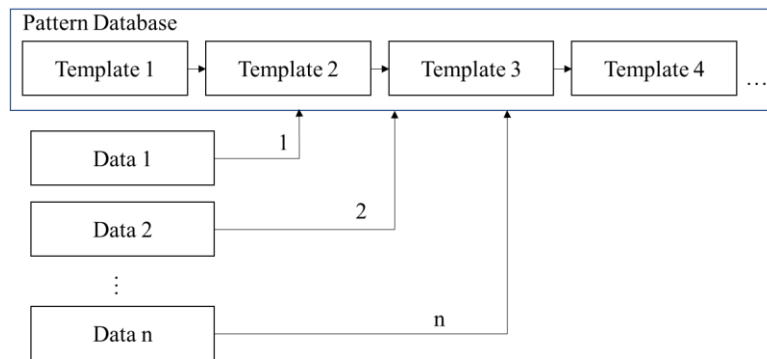
Figure 5-6 Illustration of the matching scheme of both C-scan and B-scan pattern recognition

By inputting GPR parameters as in Figure 5-5 (b), the FFZ is calculated according to Equation [2.19], and then the void size can be estimated based on the relationship between void response and void spread. With the estimations of void position and void spread from both C-scans and B-scans, the operator can then make preliminary decisions regarding the void. The whole program imitates the human judgement process, but leaves the heavy cross-checking work to the program once the GPR survey setting information has been input.

5.2 Case experiments

The matching score determines the sensitivity of the detection. Two experiments were conducted to test the workflow and find the optimum matching score: a laboratory experiment within a controlled environment and an outdoor site experiment. Then another two validation experiments were conducted to test the matching scores. There were 2 criteria used for evaluating the precision and accuracy of the void pattern recognition:

1) the pattern detected was generated by the air void;
2) the type of pattern matched with the void size.

For each criterion, the results can be categorized into 4 classes (Powers, 2011):

True Positive (TP):	False Positive (FP):
a void exists, and workflow claims it exists	void does not exist, but workflow claims it exists
False Negative (FN):	True Negative (TN):
a void exists, but workflow claims it does not exist	void does not exist, and workflow claims it does not exist

The recognition sensitivity was evaluated using a true positive rate (TPR) and a false positive rate (FPR), as described by Equations [5.3] and [5.4] respectively, and a higher TPR means a higher sensitivity (Fawcett, 2006).

$$\text{TPR} = \frac{TP}{(TP + FN)} \qquad [5.3]$$

$$\text{FPR} = \frac{FP}{(FP + TN)} \qquad [5.4]$$

The selection of a matching score is critical in recognition performance, especially for B-scan patterns. Multiple adjustments may be necessary before an optimal matching score is established. The use of a receiver operating characteristic curve (ROC) was used to find the best matching score. The ROC plots the TPR against FPR, and the data point – matching score – that is closest to the top left-hand corner (TPR =1, FPR = 0) denotes the perfect result; however, all results are correct, and none is left out. Then the distance of each value point from the perfect result point (0,1) was calculated using Equation [5.5] in order to find the smallest variance and thus the optimum matching score (Fawcett, 2006).

$$\text{Optimum} = \min_{i} \sqrt{(FPR_i^2 + (1 - TPR_i)^2} \qquad [5.5]$$

where i denotes each data point in the ROC plot.

5.2.1 A laboratory experiment (Void immediately underneath a paving glass fibre panel)

Similar to the experiments in the forward modelling (Chapter 4.2.1), another void was created in the soil tank of the Underground Utility Survey Laboratory in PolyU. The void spread was measured as 15*25*15cm in length, width and height respectively, and was surrounded by dry

garden soil whose relative permittivity was assumed as 7. A GPR survey was conducted using a 900MHz GSSI unit within an orthogonal grid. The void spread is therefore significantly larger than the GPR footprint, so that reverberations and cross-like response .could be observed The survey site measured 100*140cm and the profile spacing was 10cm. Having undergone basic signal processing, such as de-wow, gain, bandpass, time zero correction and velocity analysis, the GPR profiles were stacked together to construct C-scans based on the standard workflow (Figure 3-3) for C-scan generation. A surface void was imaged inthe C-scan images, as shown in Figure 5-7. The reflection intensity of the void is significantly higher than that of the background, and the edge of the void is blurred.
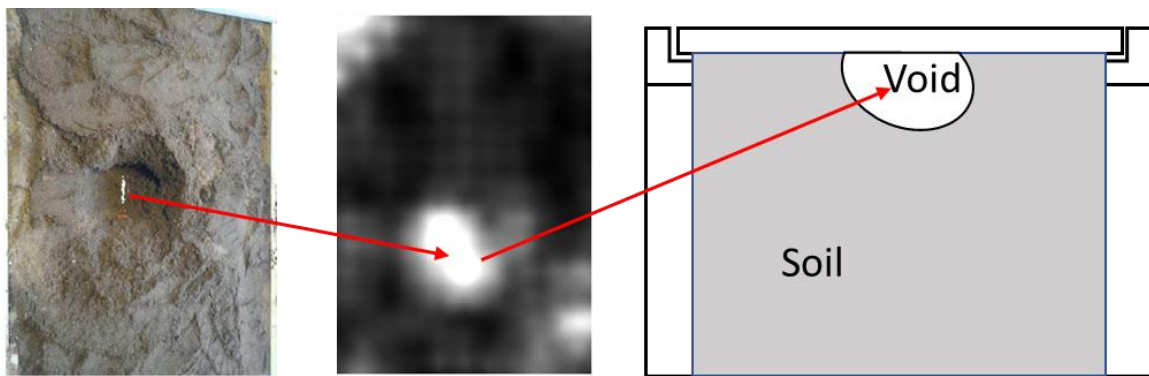
Figure 5-7 Illustration of the surface void dug in the laboratory and its C-scan

In the C-scan pattern recognition, 2 air voids were identified: one is the target void in the centre of the survey site (47, 48), and another is a manhole in the top left-hand corner (10, 130) of the survey site. They both present as strong local reflections in C-scans. The position of the void centre and void size estimation are displayed in Figure 5-8.

a   b
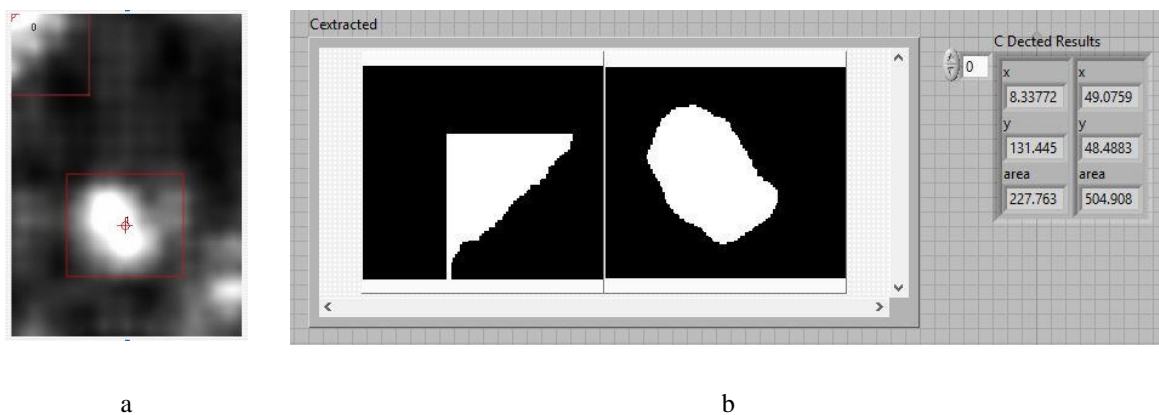
Figure 5-8 Stage 1: Results of void identification from C-scans in the laboratory experiment. (a) shows 2 identified voids in the laboratory experiment as in red rectangle and (b) presents the extracted voids with their size and position information. Remarks: column x and y present

the coordinates of the void centre, while 'area' shows the void size estimation (cm2) of each detected void.

Even though the void shape was not a regular circle like that of the template, it was successfully identified. The matching score was 780 in C-scan pattern recognition, only the 2 largest anomalies were extracted, and smaller scatters were excluded. When compared with the void's true size, the void size estimations were slightly bigger (33.3%). The inhomogeneous reflections surrounding the void contributed to imperfect boundary definition during void extraction, and some adjacent responses were also in error included, as indicated by the red rectangles in Figure 5-8(a).

For the 2 detected "voids" in the C-scan (stage 1 in Figure 5-1), 4 GPR radargrams were indexed (stage 2 in Figure 5-1). A total of 15 matching scores values were tested, ranging between 150-350. The performance results with the ROC are displayed in Figure 5-10. According to Equations [4.2], when the matching score was set to 200 (shown as a red dot in Figure 5-10), the workflow performed the best, which resulted in 8 events being recognized as void responses, among which 5 were true positive, as displayed in Figure 5-9. And the other 3 were false alarms (false positive). With the matching score set at 200, the TPR and FPR were 0.8 and 0.59 respectively.

a   b
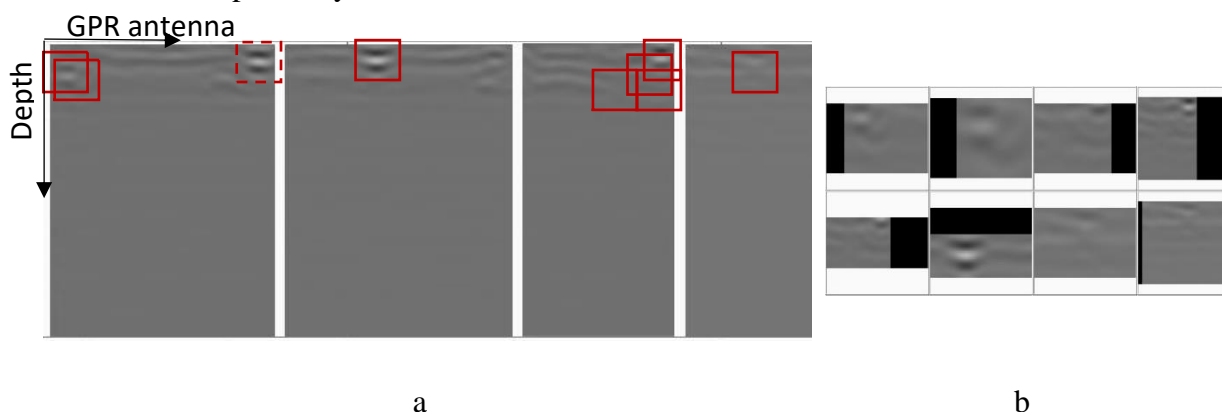
Figure 5-9 Stage 2: Results of void verification from B-scans of laboratory experiments (a) 4 indexed B-scans and (b) all recognition results in laboratory experiment. Remarks: solid red rectangles are TPs, dashed red rectangles are FNs, and dotted rectangles are FPs.
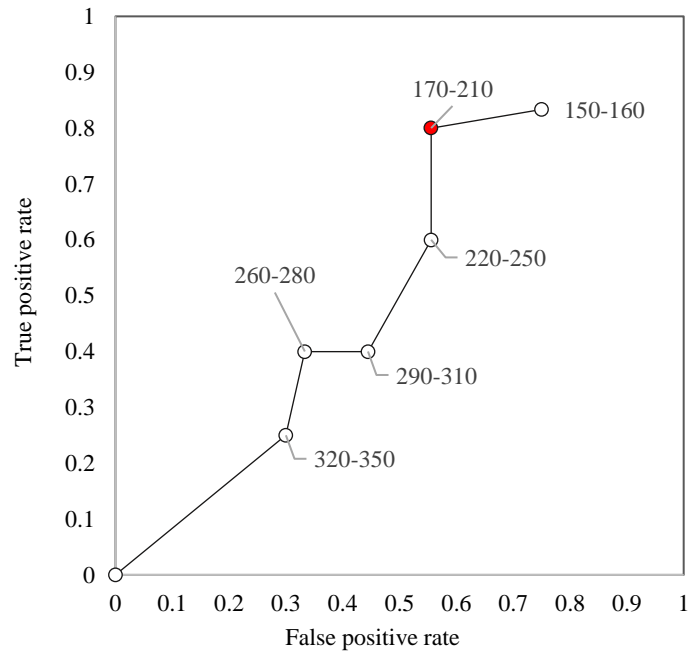
Figure 5-10 The receiver operating characteristic curve of void recognition from B-scan in the laboratory experiment. The optimal point is highlighted with red.

Figure 5-11 displays the positions of detected results from both C-scans and B-scans; they are closely distributed, which means the void positioning results were promising. Table 5-1 summarizes the size estimation results from both C-scans and B-scans. It is obvious that the size estimation from B-scans was not accurate enough: although the void was indeed highlighted, the identification was based on the incorrect types of pattern templates and led to an incorrect size estimation.
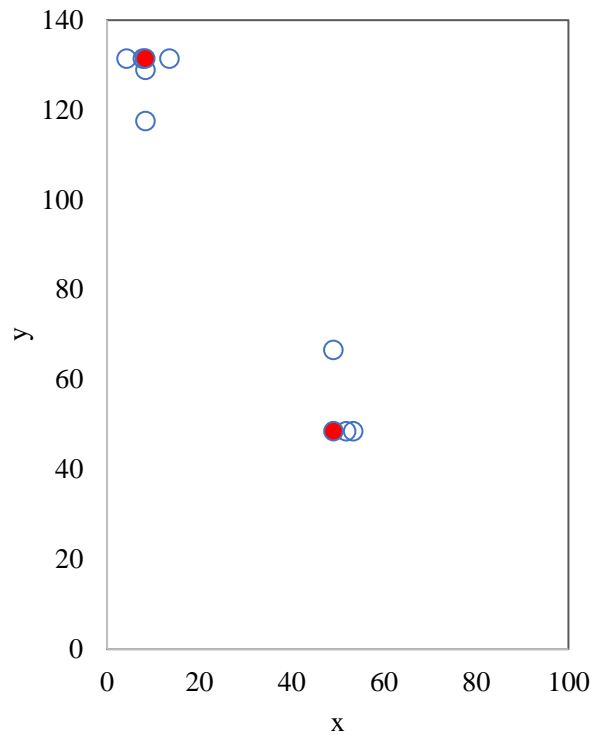
Figure 5-11 Summary of void size estimation in the laboratory experiment (cm)

Table 5-1 Summary of void size estimation in the laboratory experiment (cm)

Void	Area by C-scan	B-pattern	Spread by B-scan (cm)	Area by B-scan (cm^2)
V0	227.762	Hyperbola	7.7	46.6
		Bowl	23.1	419.3
		Hyperbola	7.7	46.6
		Cross	15.4	186.4
		Reverberation	46.2	1677.3
V1	504.908	Hyperbola	7.7	46.6
		Hyperbola	7.7	46.6
		Cross	15.4	186.4

5.2.2 A Site experiment (Void underneath concrete paving platform)

The tank in the laboratory was filled with homogenous soil, such that beyond the reflection from the void, there was hardly any signal disturbance. But in the real world, the subsurface environment is very complex and multiple types of objects in various shapes and materials are buried there. Real world site experience is therefore necessary to validate the workflow, and the survey of a seawall platform in Tai O, Hong Kong provided just such an opportunity.

Figure 5-12 Tai O site and its C-scan at 40cm deep

The site is near the seashore and subject to the threat of seawater infiltration. Voids are likely to have occurred and there were indeed voids found there, as shown in Figure 5-12. The site area measures 280*320cm in size. GPR data were collected by traversing the grid in both the x and y directions using a profile spacing of 20cm. A 400MHz GSSI antenna and RADAN SIR-4000 control unit were utilized in this survey.

Standard 2D and 3D processing were conducted on the GPR profiles. C-scans were generated as in Figure 5-12, and 2 voids were clearly imaged: one was already known, but the other was previously unknown. The shapes of the two voids were even more irregular than the void created in the lab. In this experiment, the matching score for C-scans was kept the same at 780. The recognition result illustrates that the object shape does have certain effects on the result of greyscale pyramid pattern recognition. Since the void template in C-scans is almost circular in shape, an area of high reflection in the Tai O site C-scan was incorrectly identified as two voids (void-0 and void-2). The scattering around the hypothetical voids was also recognized to exist within the void. According to previous research conducted at this site, 2 voids were confirmed: one was a visible and known surface void that was identified as void-3 in this study, while the other was an invisible but known shallow void that was detected as void-2 in this study (Lai et al., 2017a). According to a site record drawing, there was a group of vertical utilities located in the position where void 0 was identified, and they also generated a strong reflection in the C-scan. In contrast, void-1 was not found in any previous records. The C-scan recognition results and size estimations are displayed in Figure 5-13.

a   b
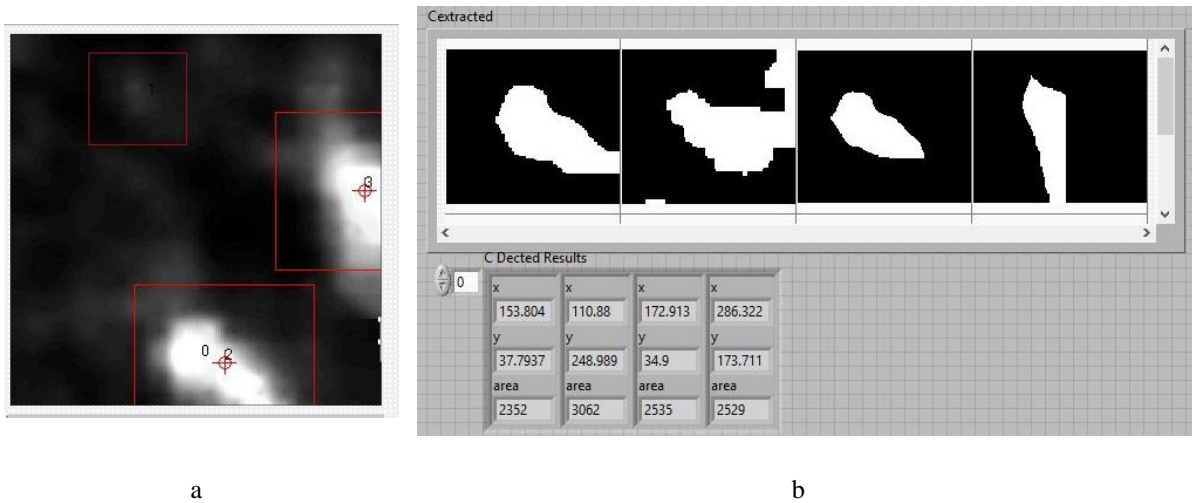
Figure 5-13 Results of void pattern recognition from B-scans of site experiments. (a) identified voids at Tai O site in red rectangles; (b) the extracted voids with their size and position information. Remarks: column x and y present the coordinate of the void centre, and column area shows the void size estimation of each detected void

There were 4 voids extracted from the C-scans, which led to 8 GPR profiles being indexed, as shown in Figure 5-14. In terms of B-scan recognition, the matching score was explored from 150 to 350, by an increasing step of 10. The ROCs demonstrating the performance of various matching score are displayed in Figure 5-15. It is obvious that the value of 180 yet again provided the optimal performance. As shown in Figure 5-15, 15 events were recognized as void patterns, and 10 of them were correctly identified. The TPR is 0.75, which is comparatively lower than that of the laboratory experiment.
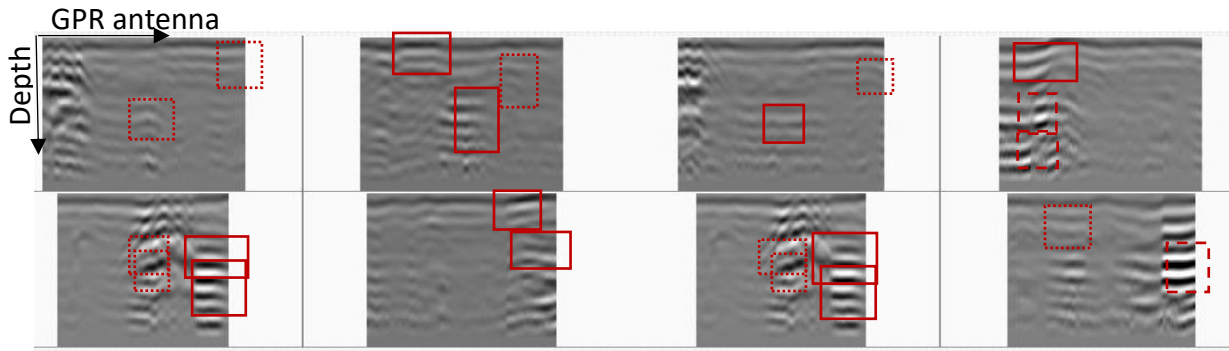
a
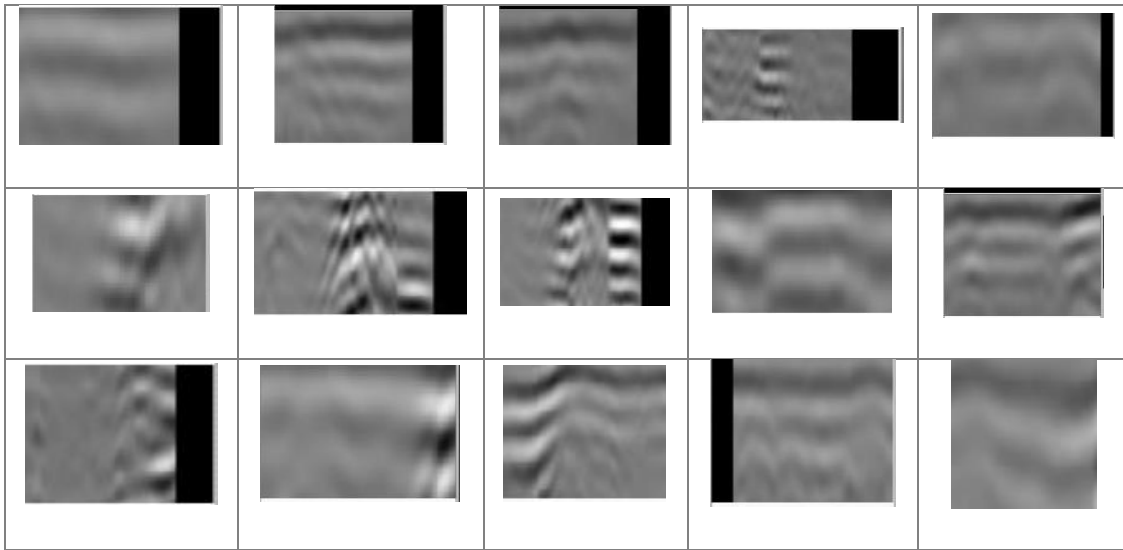
B

Figure 5-14 Result of void verification from B-scans of the site experiment. (a) are 8 indexed B-scans and (b) shows all recognition results in the Tai O experiment. Remarks: solid red rectangles are true positives, red dash rectangles are false negatives, and dotted rectangle are false positives.
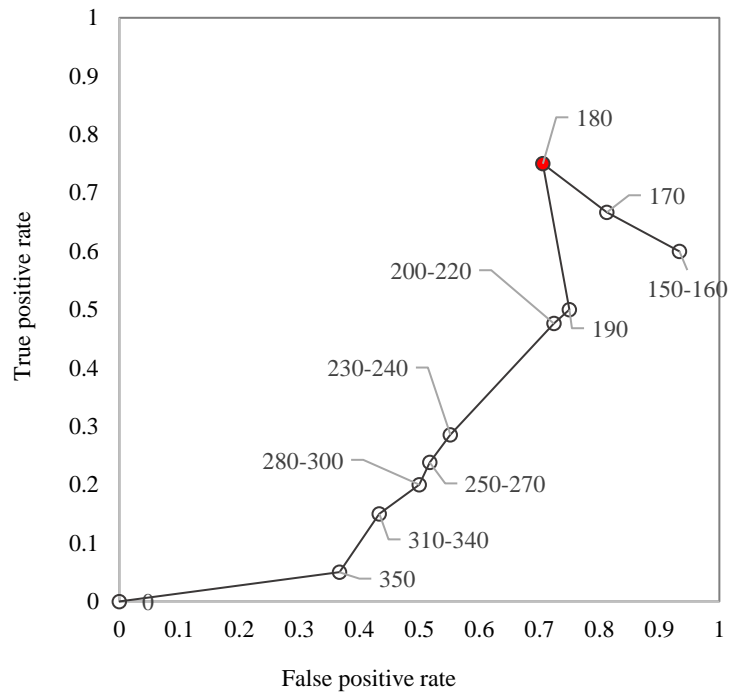
Figure 5-15 The receiver operating characteristic curve of void recognition from B-scans in the Tai O experiment. Remarks: the optimal point is highlighted in red

Figure 5-16 displays the positions of detected results from both C-scans and B-scans: they are rather sparsely distributed. Multiple patterns were identified along a traverse. The three clusters of points voted for the three suspected void areas. The void size estimations from both C-scans and B-scans are displayed in Table 5-2. Since excavation was not permitted within the historical site, it was not possible to ground truth the voids' existence, not to mention confirm their sizes. The results of the void extraction from C-scan and B-scan were found to be very similar comparing the extracted voids. The sizes estimated from B-scans were variable; however, the response of a single void was successfully matched with multiple templates,

which was similar to the results of the laboratory experiments. In conclusion, size estimation from B-scans is unreliable.
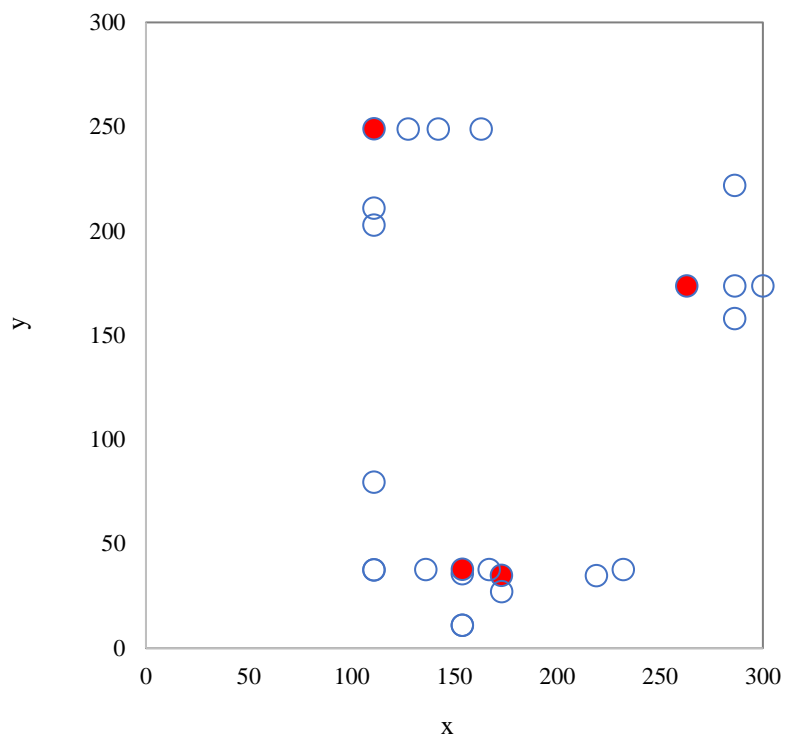
Figure 5-16 Position of the identified pattern from both C-scan (red) and B-scans (blue) in the Tai O experiment

Table 5-2 Summary of void size estimation in Tai O experiment (cm)

Void	Area by C-scan	B-pattern	Spread by B-scan (cm)	Area by B-scan (cm²)
V0	2352	Hyperbola	19.1	287.8
		Cross	38.3	1151.1
V1	3062	Hyperbola	19.1	287.8
		Reverberation	114.8	10360.3
		Hyperbola	19.1	287.8
		Cross	38.3	1151.1
		Bowl	57.4	2590.1
V2	2535	Hyperbola	19.1	287.8
		Cross	38.3	1151.1
		Cross	38.3	1151.1
		Bowl	57.4	2590.1
		Hyperbola	19.1	287.8
		Hyperbola	19.1	287.8
		Cross	38.3	1151.2
		Bowl	57.4	2590.1
		Hyperbola	19.1	287.8
V3	2529	Hyperbola	19.1	287.8
		Bowl	57.4	2590.1
		Hyperbola	19.1	287.8
		Reverberation	114.9	10360.3

5.2.3 The validation of workflow at the Lamma Island site

The matching score suggested in the laboratory and site tests is approximately 700 in the C-scan; and 200 in B-scans. The methods and the matching score were further validated with a real site case in a power plant in Lamma Island, Hong Kong. The validation site is 7m x 30 meshown in Figure 5-17(a). A GPR C-scan about 1 meter deep is shown as Figure 5-17(b).

a
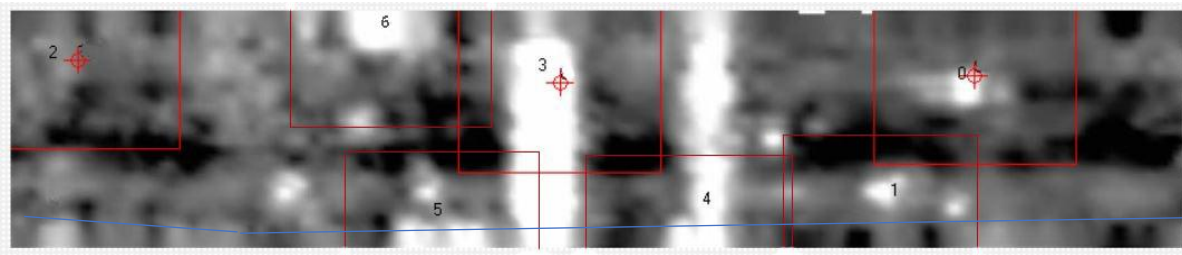
b

Figure 5-17 The validation experiment in Lamma island. (a). is the photo of the validation site; (b) shows the result of the void locating from the C-scan.

The analysis starts with the C-scan. With the use of a matching score value for the C-scan of 600, in total 7 areas were identified as suspected voids – they are presented as the local-high intensity in the C-scan. Among these 7 areas, features labelled as 0, 1 and 5 were identified as metallic utility pits after comparison with record drawings, features labelled as 3 and 4 were concrete utility pits, and they could be seen from the ground. Feature 2 was an unknown reflector, and its intensity of the reflection is small compared to another feature no. 6, thus it is manually disqualified as a suspected void.

The second step of the investigation is the pattern recognition of the B-scans with the established database. A section of the B-scan that cross both feature 3 and feature 6 was indexed (Figure 5-18). It can be seen that the GPR reflections at the two features (blue rectangles) were very similar to the pattern of large voids – the plain reverberation.
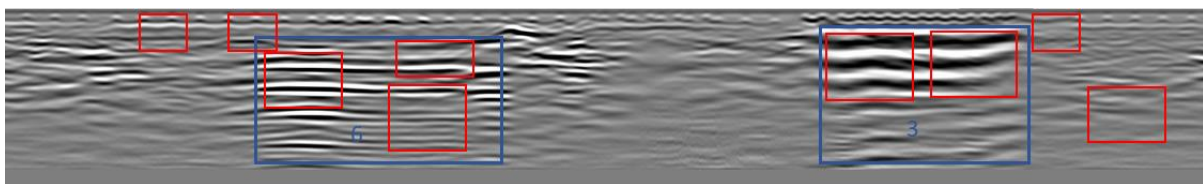
Figure 5-18 the result of the void pattern verification from B-scan, Remarks: blue rectangles indicating the areas of suspected void 3 and void 6 in Figure 16, and red rectangles circle the identified GPR responses.

When the matching score were relaxed to 250, the result of the void verification from B-scan was shown as red rectangles in Figure 5-18, and many of them fell outside the areas of blue rectangles. The additional number of features appears because they are small scatterers that fit the database of voids in the established database. However, they were given lower confidence because they were not in the location of feature 3 and feature 6. One can see that the suspected features as voids can be controlled by changing the matching score. Nevertheless, feature 3 and

feature 6 met the two criteria of the void identification workflow: present as the high reflection in C-scan and the reflection in B-scan match the specific pattern, and therefore are qualified .to be excavation A pit was therefore dug in the area of void 6. But after digging, a large piece of the concrete plinth was found and it wverified as a false alarm. The validation test in the Lamma shows the limitation of the proposed system: when the GPR reflection of the object is similar to that of voids, the system may not be able to distinguish them. But still, those areas apart from feature 3 and 6 are therefore concluded as void-free.

5.2.4 The site validation at the Shek Mun on the workflow

Another validation was conducted with the GPR data collected in the Shek Mun (Figure 5-19). The matching score suggested in the laboratory and site tests, around 700 in stage 1: void locating from the C-scan and 200 in stage 2: void verification from the B-scan, were also applied in this site case. The specification of the site was discussed in Chapter 4.4.2.
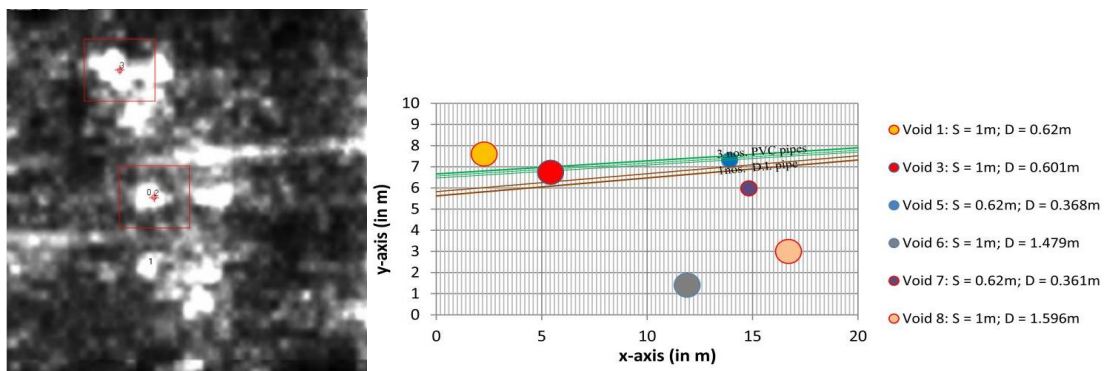
Figure 5-19 The C-scan detection result of the validation experiment in Shek Mun. Remarks: blue arrow refers to the indexed B-scan.

The Figure 5-19 shows that two voids were identified from the C-scan. A piece of radargram was indexed for the 2nd stage: B-scan recognition. Figure 5-20 presents the result of the B-scan recognition in the Shek Mun data: 6 areas were recognized as matching with void patterns, among which 2 were generated by void 1 and void 6. The remaining 4 false alarms (FP) were generated by the scattering.
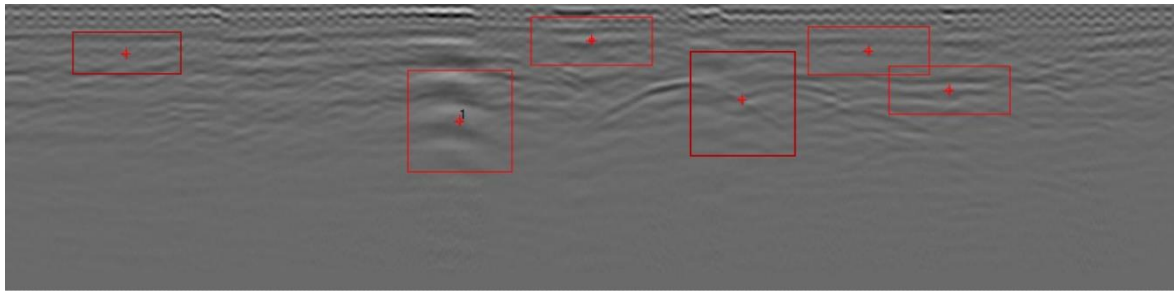
Figure 5-20 The result of the B-scan detection result of the validation experiment in Shek Mun

5.3 Discussion on void diagnosis

A database of four void patterns (hyperbola, cross, bowl, plain reverberation in Chapter 4) based on numerical models and laboratory experiments for both C-scans and B-scans was applied. The pyramid pattern recognition method – with pixel value or gradient used for object identification – was used to search for such GPR responses automatically with an in-house LabVIEW program. In this way,the preliminary knowledge of the void location and void size can be obtained without human intervention. In view of the demanding and heavy workload involved in subsurface health inspections, the workflow has proven to be efficient and effective. The study result raises the possibility of conducting city-scale and full-coverage subsurface health inspections.

5.3.1 Reasonable recognition workflow and promising void positioning

The four experiments in Chapter 5.2 demonstrate that the subsurface void positioning of the workflow is promising. Subsurface voids in 2 tests (the laboratory and Tai O) were successfully and precisely identified, and in the Lamma validation experiment, the matching scores were proved that only void-like patterns were identified even though the final identified feature 6 was a false alarm. Similar to seeing a medical doctor – comprehensive medical examinations are of vital importance before a diagnosis can be concluded. C-scans can deliver a comprehensive view of the subsurface world, and the position and shape of subsurface objects can be roughly delineated. For civil engineering applications, it is essential to conduct a 3D GPR survey in order to ensure important information concerning the underground situation is not omitted.

a. **Tolerances of void positioning and void spread estimation**

However, full coverage C-scans are generated using interpolation to fill in blank areas within survey profiles, which means that some pixel values in C-scans are a reflection of processed

values rather than true measurements. In addition, the indexed B-scans are not necessarily positioned to cut across the centre of the void, since this position may be located in gaps among the GPR survey profiles. The maximum deviation of B-scan positions from the void centre is half of a profile spacing. If the shape of a subsurface void is very irregular, then the patterns identified in B-scans may not describe the void's geometry. Besides, during the B-scan recognition stage, the void size is determined by predefined models multiplying the GPR footprint, and void size estimation is therefore not a continuous measurement and may only result in one of several predefined numbers. This further illustrates the point that estimations of void spread and area from B-scans are unreliable.

b. Conservative but efficient approach

The whole recognition process, from the initial stage of C-scan scanning, to the final void diagnosis stage, takes less than 10 minutes, which is significantly more convenient than the currently used visual interpretation approach. In view of the time-consuming nature of GPR data interpretation, the application of automatic pattern recognition in GPR survey deserves further investigation in order to improve its reliability. The pyramid method applied in this study possesses both strengths and weaknesses. In B-scan recognition, it efficiently identified most GPR responses from air-filled voids in both experiments when using a lower matching score, although the experimental data was significantly different from the void template. The weakness of using lower matching scores is that it may lead to not only higher TPRs but also higher FPRs. Considering the hazardous nature of subsurface voids, it is better to be conservative in order to avoid missing voids.

c. Using greyscale or gradient as image information

In this study, greyscale value and gradient were used for object recognition in C-scans and B-scans, respectively. This approach was proven to be suitable through experiments. On the contrary, if the gradient approach was used in the C-scan void recognition, some round shaped local anomalies with weak reflection intensities were incorrectly identified as voids, because the template used in C-scans is round shaped and the gradient method focuses on pattern structure. Similarly, if the greyscale approach was used in the B-scan void recognition, more reflections with strong intensities were in-correctly identified as voids, while actual void responses with weaker reflection intensities were overlooked. Such cases resulted in lower TPRs and higher FPRs.

5.3.2 Accuracy of the void recognition workflow

Both the designed workflow and case experiments illustrate that in a GPR survey, an air void can only be defined by satisfying two criteria. The first criterion is the existence of non-continuous strong reflections in C-scans, while the second is the presence of special patterns with decaying amplitude and later time windows in B-scans. These two criteria reflect the findings of previous research (Lai et al., 2017a). The accuracies of the experiments were evaluated by classifying the pixels of B-scans. Table 5-3 presents the accuracies of the 4 case experiments – 2 tests for the matching score value and 2 validations.

Table 5-3 Accuracies of the case experiments

	TP	FP	FN	TN	Accuracy
Test	11%	6.7%	1.9%	80.4%	91.4%
Validation	2.85%	22%	0	75.15%	78%

Notes: Accuracy = TP+TN

In the 2 tests, the FPs (false alarms) were mainly caused by three reasons.

1) In the real survey, the GPR reflection did not totally coincide with that in the pattern database. Many factors distorted the GPR reflections. Specifically, the void's extent inthe Tai O site was large enough to yield reverberation patterns, but very often some cross or hyperbola responses with weaker reflection intensities were found near to the targeted reverberation response. These cross or hyperbola like GPR responses were interference generated by the void's top and bottom edges. As these responses occur at the edges of voids instead of within them, they might be confused with void patterns and contribute to incorrect void positioning. The interfered response also results in a single void being identified by multiple templates, which in turn produced various void size estimations. With B-scans, it is difficult to describe a void's appearance using a series of templates. Obvious differences can be observed by comparing templates and experimental data. Many factors, including inhomogeneous background material, equipment specifications, survey settings such as PS and the time window, and interference from adjacent objects, contribute to a variety of GPR responses to voids.

2) Many objects may yield similar reflection patterns like voids. For instance, in the Tai O experiment, an underground structure was mistakenly identified as void-0 in the C-scan as it also presented as a local strong reflection. But in the B-scan recognition stage, no proper pattern was matched with this void, and it was therefore identified with reduced confidence. The workflow, which firstly locates void-like features using C-scans and secondly verified by B-

scans, is logically designed to enhance the confidence of void identification while some false alarm, like void 6 in Lamma Island case, requires further improvement.

In both the C-scan and B-scan recognition stages, the Tai O experiment has higher FPRs, which means more irrelevant responses were identified as voids. The laboratory experiment was conducted using a relatively homogenous background medium and, beyond the two identified voids, there were hardly any scatterers. In contrast, it can be observed from Figure 5-14(a) that diverse and complicated response events were present in the Tai O site radargrams. Some of these response events were generated by multiple unknown objects rather than voids. Having said that, the two validation experiments achieved a 78% accuracy, without any FN (omission). The underlying reasons were similar to that observed in the test experiments: objects may yield similar reflection patterns, which made them be mistaken as voids. The concrete plinth in the Lamma island was a clear example. Moreover, both the subsurface void and manhole in the Lamma experiment were filled with air and had an interface of significant dielectric contrast with the soil. They both, perhaps not surprisingly, presented quite similar patterns in both the C-scans and B-scans. In addition, another problem was observed in the validations as follow:

3) The scattering in the real site contributes to false alarms. In both Lamma and Shek Mun experiments, heavy scatterings presented in the radargrams – they were in Mie type scattering of the GPR signal. The effect ofthe Mie type was caused by the object size being of the same order as the wavelength (Annan, 2004). When the host media was not "clean" enough, the wave would be scattered and yield reverberation-like reflections. It can be improved by adjusting the matching score values as demonstrated in Chapter 5.2, where a only large void is recognized. The effects from the latter two problems: unknown subsurface structures and scatterers, can be eliminated if periodical time-lapse surveys are available. Since these subsurface structures and scattering are assumed to exist in the subsurface consistently, time-lapse surveys can help in excluding these reflections and stand out the real "changes" only.

5.4 Summary and contribution

In this study, a semi-automatic workflow that integrates the pattern recognition to detect voids from GPR data was developed and validated. It was proposed that, the sensitivity of the detection, which is controlled by the matching score, should be higher in the C-scan detection but lower in the B-scan recognition.

Through experiments and validations, three reasons for causing false alarms were found. And two of them may be eliminated by the time-lapse survey to be reported in the next Chapter. Beyond the flexible matching method used in this study, the use of intelligent searching and learning schemes deserves further exploration. In particular, the machine learning technique can be applied to continuously train the classifier using both simulation or real GPR measurements, so as to improve the precision and accuracy of void identification.

Chapter 6 Subsurface temporal diagnosis with time-lapse GPR data

Although different subsurface objects generate special GPR responses, as have been discussed in Table 4-1 and Chapter 5, some subsurface events do not yield GPR responses with a specific pattern structure in the B-scan: these events are hard to be identified from the GPR data. Also, some subsurface objects generate very similar reflections. In addition, due to the complex and unknown environment of the subsurface, biases from human perception are inevitable in generating GPR C-scans. It is suggested that a single measurement is not reliable enough for determining small changes. Establishing a "medical record" with a series of time-lapse GPR C-scans is an effective means to identify potential subsurface defects. Besides, if we have a baseline depicting how a healthy situation should present in GPR data, then by comparing this baseline with images obtained later, potential defects can be relatively easily located from GPR C-scans by techniques of change detection from images. This approach further facilitates the possibility of conducting subsurface surveys that have a city-scale coverage: if only changed areas need to be inspected, the workload will be reduced significantly.

This chapter explores the capability of applying time-lapse GPR data to investigate the health condition of subsurface utilities. A workflow integrating methods of change detection from an image is proposed in this chapter to extract changes from time-lapse GPR C-scans. The workflow is validated with a site test.

6.1 The workflow of temporal changes extraction from time-lapse GPR C-scans

A fast and robust method for change-detection from images is desired to extract dissimilarities among time-lapse GPR C-scans for further investigation. Given the complexity of GPR C-scans, a standardized 3D imaging workflow is required to make sure the time-lapse GPR C-scans are reliable for comparison, with as little as possible human judgments introduced. GPR C-scans are semantic images that variations among time-lapse C-scans based on Figure 3-2 are inevitable. Proper preprocessing for reducing the subjective discrepancies among time-lapse C-scans is the key to success in change detection. A workflow that integrates imaging pre-processing and image change-detection technique is proposed in this study. The workflow consists of two stages: image preparation and changes detection, as shown in Figure 6-1.
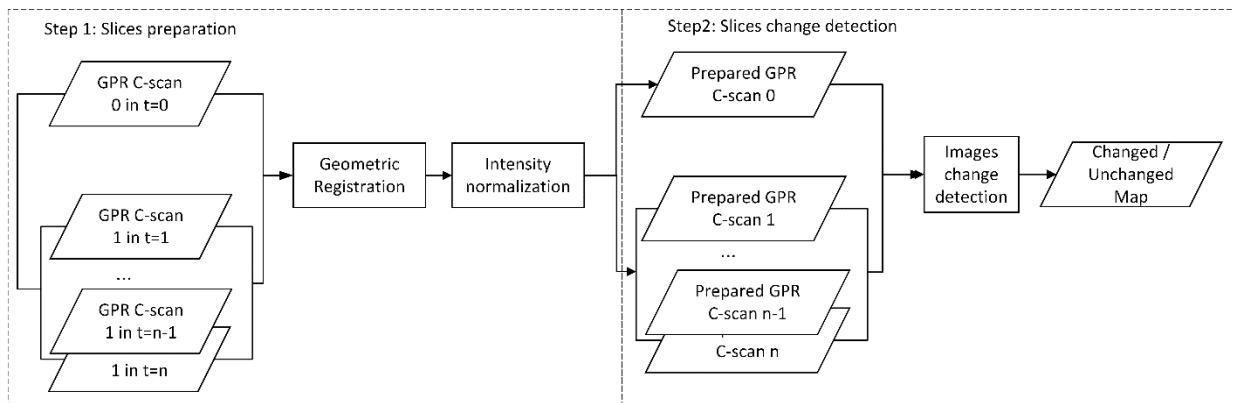
Figure 6-1 General workflow of temporal changes extraction from time-lapse GPR C-scans

6.1.1 GPR C-scans geometric and intensity rectification

GPR C-scan images are models for the subsurface environment, when images generated by similar criteria can be used for change detection. The reflection intensity and positions of the two images must be consistent (Townshend et al., 1992). Such that corresponding geo-referenced pixels in an image should describe the reflection of the same position. And the pixel values which depict the reflection intensity of the same position, should be within the same colour coding scale. Hence the first step is the image preparation: register the pixel position and normalize the reflection intensity of the temporal GPR C-scan pair.

For the gridding of the GPR survey, positioning errors are mainly caused by the offset between the GPR antenna and the predesigned grid. Then the actual GPR traverse grid may not coincide with the recorded grid. Thanks to the integration of a global positioning system and auto-track total station with a GPR system, under certain circumstance, a GPR survey is no longer needed to follow a predefined grid. But the real-time global positioning itself has errors.

When constructing GPR C-scans, recorded reflection intensities within the system's dynamic range (32, 64 bits) are transformed into digital values of pixels. Applying adjustment on this transform scale could result in different imaging results. Besides, GPR signals attenuate with an increasing depth of penetration. Time-vary gain is always applied (Figure 2-5) to artificially enhance the signal strength in the deeper area to make the GPR reflection "visible". However, the gain function is case-specific as the attenuation rate is determined by the dielectric properties and the conductivity of the host material. If the gain is not tailored properly, the survey target cannot be depicted clearly. Variation in the GPR C-scans process may bring artificial discrepancies into the time-lapse dataset. Therefore, proper amplitude or reflection intensity normalization is required to ensure the pixel values of time-lapse images are

correlated. When C-scans are prepared according to the workflow in Figure 3-2, they can serve as the input to extract the changes happened underneath the surface.

6.1.2 GPR C-scans change detection with K-means clustering

As discussed in Chapter 2.6, due to the lack of ground truth data, the approach of unsupervised change detection is preferred in time-lapse GPR surveys. Zheng et al. (2014) developed a simple and effective method for obtaining difference from images of temporal-sequential synthetic aperture radar (SAR): the method combined difference images and K-means clustering to classify pixels into the changed or unchanged group. The challenges of detecting temporal changes from GPR C-scan images and SAR images are similar: unknown speckle noises in images makes the change detection much more difficult than that of optical images. The method developed by Zheng et al. (2014) was adopted and adapted in this study.

In view of the nature of GPR C-scans – a lot of isolated reflections from clusters are recorded in images; the speckle-noise reduction is very important for the entire process. GPR C-scans deliver mainly two kinds of information: one is the reflection intensity which is shown as pixel values; another is the object structure – including object shape, size, manifested as either a continuous object or local object. This study makes use of these two kinds of information to distinguish changed areas from the unchanged ones. Therefore, the change detection method adopted in this study mainly composes of three steps: 1) produce maps of difference – a reflectance's change map and a structure's change map; 2) noise reduction by filtering – remove random scatterings; 3) label the changed area by K-means clustering. The general workflow of the change detection is as Figure 6-2.
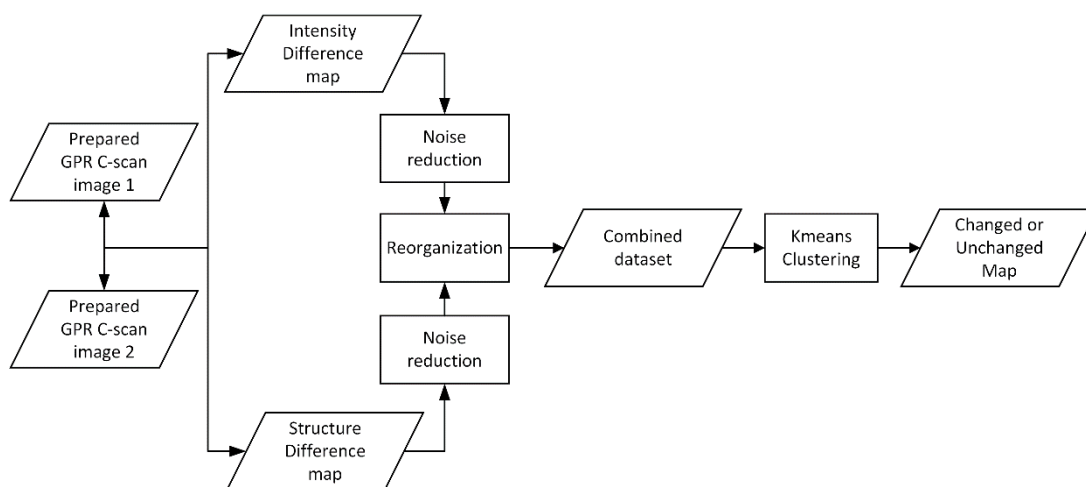
Figure 6-2 Workflow of changes detection from two GPR C-scan images

Among many unsupervised methods, K-means is selected because it is a simple but maturely developed algorithm: it partitions data into K clusters by repeatedly minimizing the within-cluster sum of squares. Originally proposed by MacQueen (1967), the general description of the K-means clustering method is given by Equation [6.1],

$$\arg\min_{S} \sum_{i=1}^{k} \sum_{x \in S_i} \|x - \mu_i\|^2 = \arg\min_{S} \sum_{i=1}^{k} |S_i| \text{Var}\, S_i \qquad [6.1]$$

where μ_{ii} is the mean of points in data S_i.

The algorithm starts with a random seed, and then partitions the data into clusters with the Voronoi diagram: assign the data point to a cluster whose mean has the least squared Euclidean distance. Afterwards, the centroid of each cluster is calculated. The algorithm repeats the process at another random seed until the sum distance of all data points to their cluster centroid is the minimum. The algorithm does not guarantee the optimum (Forgy, 1965; Hartigan & Wong, 1979; MacKay & Mac Kay, 2003). The proposed method is computationally efficient and requires limit ground truth information, which makes it suitable for working on low dimension GPR C-scans.

6.2 Workflow validation with a site experiment

6.2.1 Site specification

A case study was conducted in the Royal Palm to verify the proposed workflow. The Royal Palm is a large private residential area in Hong Kong. There are congested underground utilities buried underneath. If a utility bursts, residents' daily life would be affected seriously.

A section of the bituminous road in the Royal Palm is taken as a case (as Figure 6-3) to illustrate the feasibility of temporal observation with GPR. This section of the road was determined as old with needs of repair or replacement. Two GPR surveys were conducted at different times: the first survey served as the baseline survey, and then an evacuation was undertaken for the utility maintenance and serves as ground truth as well. The excavated area was 1.5*2 m large and 1.5 m deep, as shown in Figure 6-3(a). Then after backfilling the excavated area with the soil dugout, the second GPR survey was carried out a week later with the same survey setting as that of the first survey.

6.2.1 Survey specification

During the two surveys, two points were selected as benchmarks for adjusting the reflection intensity of the GPR data. The two points located within the survey area but were far away from the evacuation site. Also, the two benchmark points should be as far away from the utility as possible. In this way, the benchmark points were free from any changes between the two surveys, and the GPR reflections at these two points were supposed to be the same or at least very similar.

GPR data were collected by an IDS Hi-Mod 200/600MHz dual-frequency system equipped with an auto-track total station. Every single trace (A-scan) was related to coordinate measurements in the HK-80 projection coordinate system.
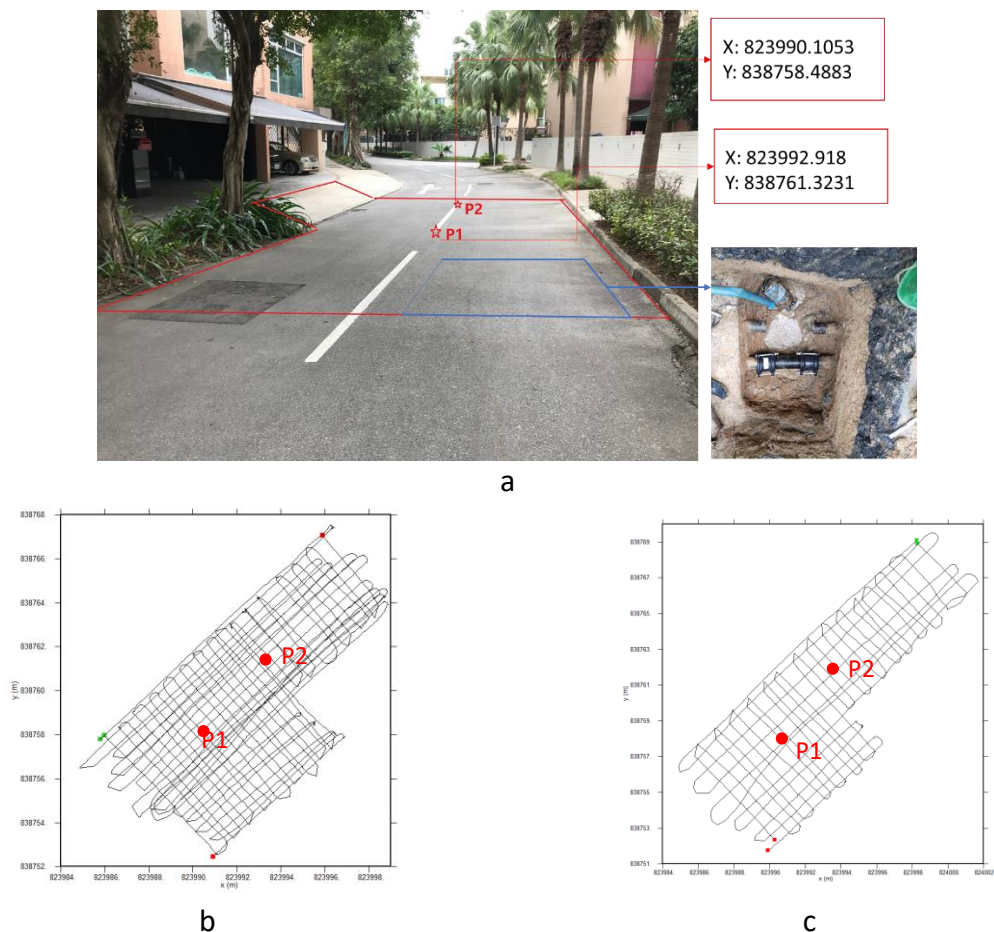
Figure 6-3 Illustration of the site area and survey paths. (a) is the photo of the case site: a piece of road in the Royal Palm. Two benchmarks are marked as P1 and P2 with stars. (b) and (c) show the survey paths tracked by the total station in the first and the second survey, respectively. The survey paths were approximately orthogonal cross grid, and green and red dots refer to the start point and the endpoint, respectively

Underground utilities are normally buried within a few meter deep; thus, in this case, only 600MHz data were investigated. The centre frequency of GPR data collected by 600MHz antenna was measured as 514 MHz with the wavelet transform (Lai et al., 2014).

6.3 Experimental results and analysis

6.3.1 The image preparation result

Standard signal processing, including de-wow, time-vary gain, frequency domain bandpass filtering, time-zero correction, velocity estimation and migration were applied with Reflexw on both GPR dataset (Jol, 2009). C-scans images were produced with GPR-SLICE from the processed radargram following a standard 3D imaging workflow, as shown in Figure 3-3. The criteria for both radargram processing and C-scan generation were maintained as much similar as possible. The produced C-scans at the utility depth (0.85 m) of two surveys are displayed in Figure 6-4. A connected higher reflection region can be clearly seen, and it is defined as a water pipe because of its connectivity. Both two images are speckle with blurry scatterings surrounding the utilities. The reflection intensity at the pipe depth of the first survey was digitized between 616 to 20048; while that of the second survey was in a similar yet slightly different dynamic range which was 313 to 20091. Even though the processing procedures were almost the same, there were many discrepancies exist between temporal GPR C-scans. These discrepancies may be raised by variations in either initial signals or electrical properties of the host materials.

a   b
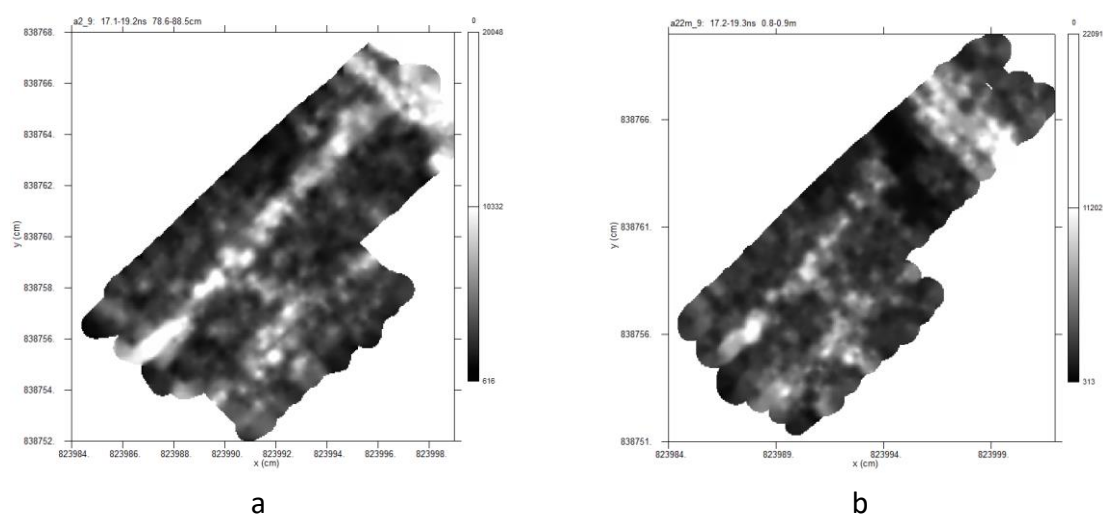
Figure 6-4 The GPR C-scans of the two surveys at 0.85m depth. (a): the first survey; (b): the second survey

The auto-track positioning system has been proven effective and efficient in many practices (Chang, 2016; Lai et al., 2018a). But the latency between the actual scan position and the measured position is unavoidable, due to the clock error between the GPR clock time and the total station's clock time. Since the latency happened along the survey path, and survey paths of the time-lapse dataset were not coincided (Figure 6-1(b) and (c)), obvious misalignments were observed in the time-lapse dataset. Because the image change-detection requires fully co-registration, which depends on correct positioning, the latency correction was introduced in this study.

As shown in Figure 6-4, without latency correction, the utilities are presented as a zig-zag shape, although utilities are made straight certainly. Along the survey path, the offset was calculated from the distance of the peak of zigzag to its centre: it was 0.1m and 0.14m in the two surveys. Given that the two surveys both used 220 scans/m, the latency was estimated as the radargram went 20- and 30-scan faster than the positioning measurement in the first survey and the second survey, respectively. Each GPR trace was moved back along the survey path. The GPR C-scans with corrected positioning are displayed as Figure 6-5.
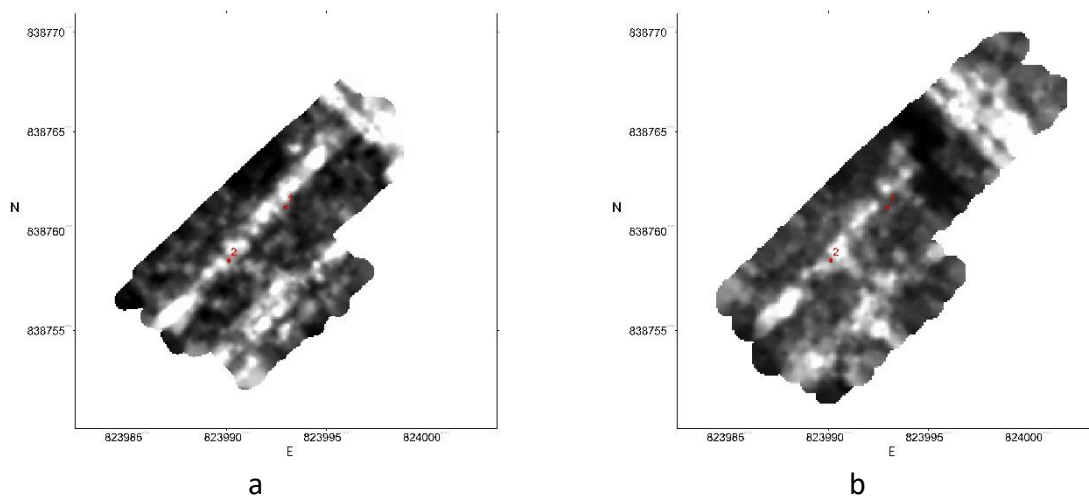
Figure 6-5 GPR C-scans after positioning correction of two surveys. (a) the first and (b) the second survey.

Another essential step in preparing images is correlating the reflection intensity of the two GPR C-scans. As it rained before the second survey, the moisture content of the soils was expected higher. It was not surprising that the global reflection intensities between these two surveys were different even though a constant gain was applied. In this study, the emphasis is laid on detecting the changes of utility groups, so the global reflection intensity change was normalized by adjusting the histograms of the two GPR C-scans. The process of intensity normalization

was: 1) project the reflection intensity to 8bit grey value; 2) identify the digital values of pixels at benchmark points; 3) align the histogram of the second survey with the first survey based on these two benchmark points, as these two benchmark points were supposed to generate similar GPR reflection intensity. After the amplitude adjustment, the discrepancies of pixel digital values at benchmark points of the two surveys were reduced, as shown in Figure 6-6. The common area that the two surveys cover was extracted, and this pair of C-scans were ready for further change detection (Figure 6-7).
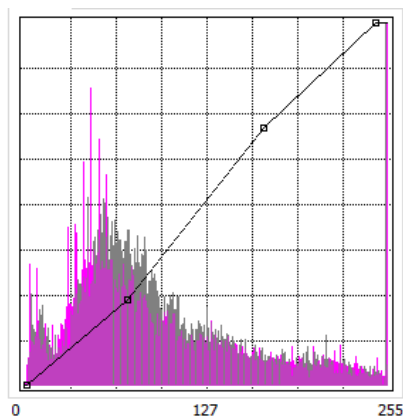
		Point 1	Point 2
2nd Survey	Original	80	132
	Adjusted	90	144
1st Survey	Original	93	143

Figure 6-6 Adjust the histogram of GPR slice of the second survey to align with that of the first survey
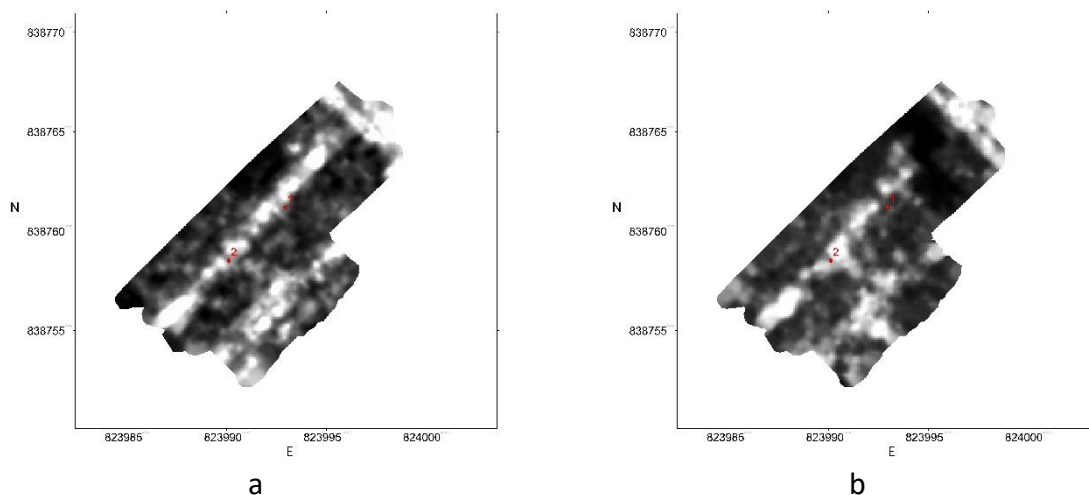
Figure 6-7 GPR C-scans with positioning and reflectance strength corrected for two surveys. (a) the first survey and (b) the second survey

6.3.2 The change extraction result

The process of change extraction was accomplished with MATLAB. The very first step was to produce maps of difference. The map of difference on reflectance intensity was produced by a subtracting operator, given in Equation [6.2], while the difference map of structure was produced by a log-ratio operator, given in Equation [6.3]. Log ratio can smoothen changes in

pixels with larger pixel value but enlarge tiny changes in pixel value smaller than 10. In this way, the edges of objects are enhanced.

$$Intensity\ difference =\ |S_1 - S_2| \qquad\qquad [6.2]$$

$$Structural\ difference =\ \left|\log\frac{S_1 + 1}{S_2 + 1}\right| \qquad\qquad [6.3]$$

where S_1 and S_2 are pixel values of the first and second GPR depth slice, respectively.

Figure 6-8 shows the result of the difference maps. There are dark boundaries surrounding the survey site, it is mainly due to the image positioning registration error. It further illustrates the importance of precise positioning registration in change detection from images, especially from very high-resolution GPR images. And both maps of difference compose of a lot of speckle of unwanted scattering of Mie type that wavelength is comparable to the object size or grain size of the soil. Hence filters were applied to eliminate these noises and reduce the interference information.

a b
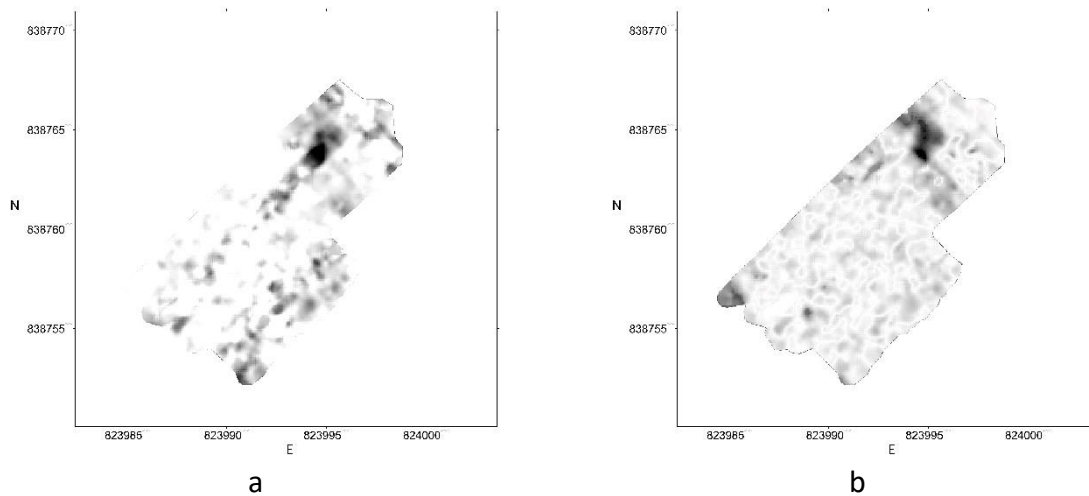
Figure 6-8 Difference maps (a) shows the intensity difference; (b) shows the structure difference of two GPR depth slice

A median filter with an 11*11 structure element was applied on the intensity difference map, while a median filter with a 3*3 structure element was used to smoothen the structure difference map. The structure element for the mean filter was larger so as to remove small and isolated differences, while comparatively a smaller structure element for the difference map of structure can preserve the edge information. Such arrangement emphasized the advantages of each difference map while reducing the bias information. The pixel values of two difference maps were normalized to 8bit (0-255), in order to lay equivalent weight on two kinds of information

– reflectance and structure. As shown in Figure 6-9, fake boundaries generated by misregistration were removed. And both difference maps still possess a large number of "false alarms", even though a significant discrepancy was highlighted as dark at the coordinate (823994E, 838763N) in both maps.
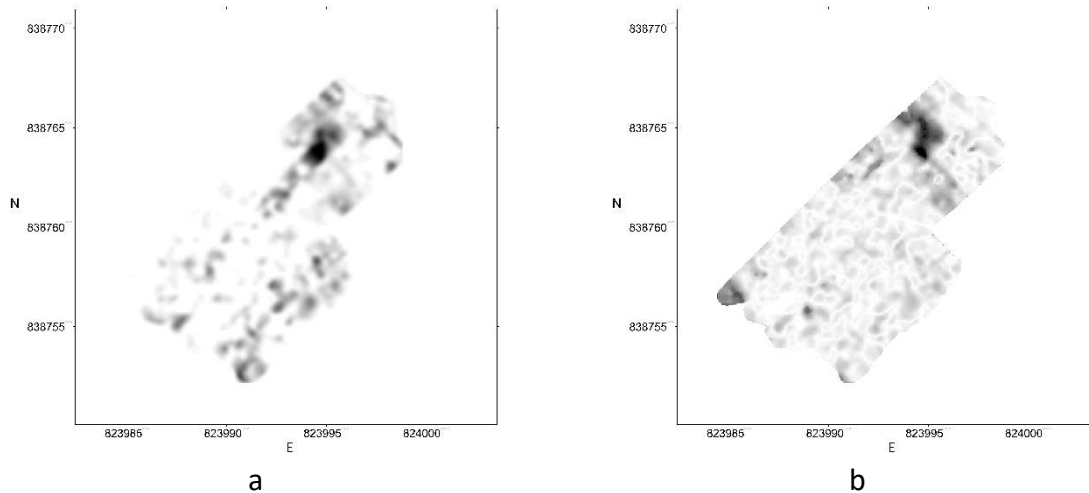
Figure 6-9 Filtered difference maps. (a) is the smoothen intensity difference map; (b) is the filtered structure difference map

The pixel values of two filtered maps were re-organized to construct a two-dimensional dataset for further K-means clustering. Two kinds of information were considered having the same importance in this study. The pixels were classified into 4 classes: 1) low intensity difference and low structure difference, 2) low intensity difference but high structure difference, 3) high intensity difference but low structure difference; and 4) high intensity difference and high structure difference, thus the K was 4 in this study. Only the area with high intensity difference and high structure difference was considered as changed area. Meanwhile, the pixel values of two filtered maps were added together to construct a combined map, and the combined map was normalized to 8-bit as well, as shown in Figure 6-10. Therefore, higher pixels value in the change map refers to areas that have more significant changes. The darkest area denotes the place that has the most remarkable changes: replaced pipe. The area labelled as change served as a mask: values of the combined map in this area were assigned to this mask, and the white areas are areas labelled as unchanged. Small and isolate discrepancies were excluded successfully.
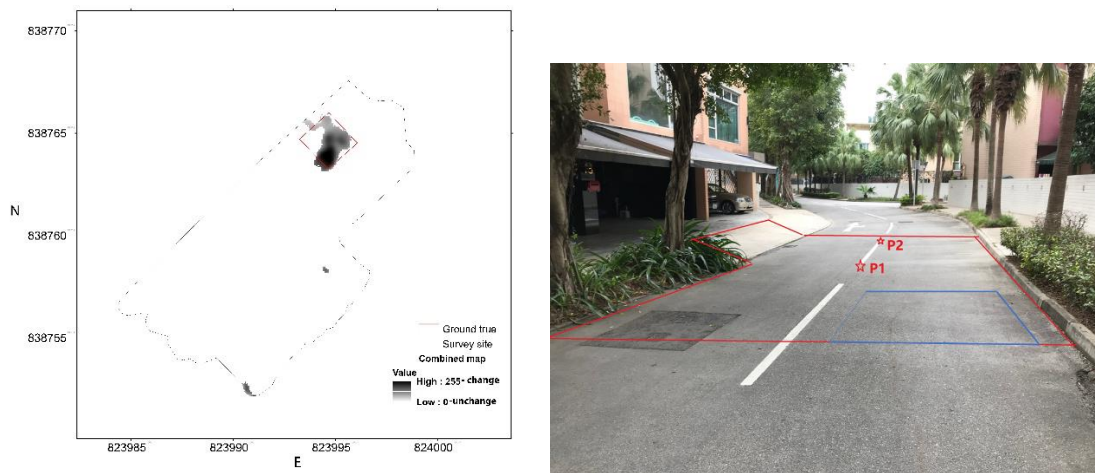
Figure 6-10 Temporal changed map that shows the detected evacuation area in the survey site

6.4 Discussion on the site experiment

The proposed temporal change detection method was proved to function well in the site experiment. Both feasibilities and challenges were observed during the experiment.

6.4.1 Performance of the proposed change detection method

The detection result was evaluated by comparing with the ground truth, i.e. the excavation area. Although there were two small areas (bottom of Figure 6-11(a)) wrongly labelled as changed, the majority were correctly classified. Since the proposed unsupervised method required no preliminary knowledge of the subsurface environment, it is particularly suitable for complex subsurface imaging. Furthermore, there was no human interaction included in the whole process, and subjective human error can be avoided.

A comparison of the proposed method with other unsupervised change-detection methods that are widely acknowledged is given as Figure 6-11. These methods were Otsu's auto-thresholding; Principal Component Analysis (PCA); and Markov Random Field (MRF) (Celik, 2009; Melgani et al., 2002; Wang, 2012): they were proved effective in change detection from noises and speckle images. The change detection method thatis proposed in this study performed better, as much less "false alarms" were produced.

| a | b | c | d |
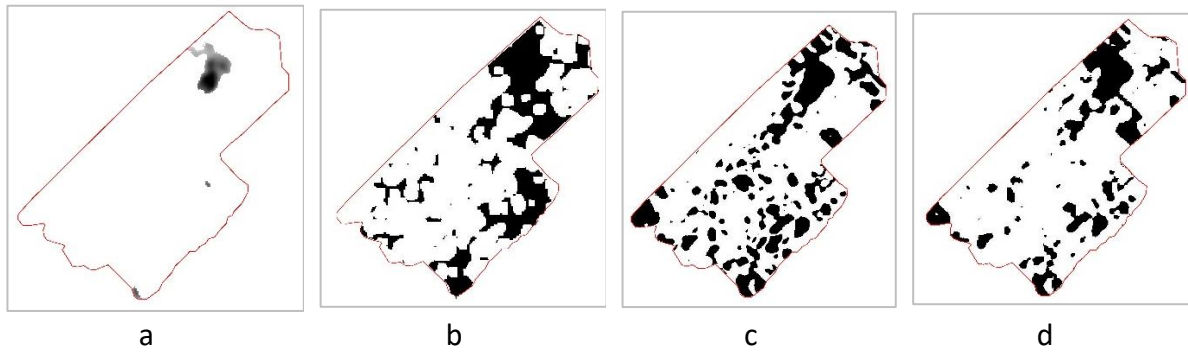
Figure 6-11 Comparison of different change detection methods. Results of the (a): proposed method, (b): Otsu's auto-thresholding, (c): PCA, and (d): MRF

The peak signal to noise ratio (PSNR) was applied to evaluate the performance of the proposed method. And the clustering accuracy was calculated with Equation [6.4]. The proposed method performs better than the others in terms of signal PSNR as well as accuracy.

$$Accuracy = \frac{TP}{(TP + FP)} \times 100\% \qquad [6.4]$$

Specifically, Table 6-1 also illustrates that the proposed method has less false positives (FP) compared with other methods. Even though more changed areas were missed (false negative – FN) with the proposed method, the position of the changed area was precisely located. The comparison in Table 6-1 shows that the proposed method provided higher PSNR – larger similarity with the ground truth, and the detection accuracy was much higher than other methods. With only reflectance strength presented, GPR C-scans were not informative enough to distinguish actual changes from random small discrepancies. It was believed that the clustering methods performed similarly, but the proposed method solved this problem by assigning meanings – either intensity or structure – to each pixel. The construction of difference maps contributed a lot to noise reduction and information extraction, illustrating that the importance of pre-processing in the change-detection from GPR C-scans.

Table 6-1 Comparison of the performance of difference change detection methods

Method	FP	TP	FN	PSNR	Accuracy
Proposed Method	958	3486	1997	20.25	78.0%
Otsu EM (Melgani et al., 2002)	23158	5132	351	10.09	18.14%
PCA (Celik, 2009)	25354	4372	636	9.30	14.71%
MRF (Wang, 2012)	17165	4669	814	10.94	21.38%

6.4.2 Preliminary diagnosis and locating potential defects

The process of change detection from time-series C-scans is the first examination of a diagnosis: similar to seeing a doctor, very often the patients are requested to take medical scans to check whether there is an unusual pattern. If anomalies are noticed, further investigations that are more specific will be conducted before a diagnosis can be given. Usually, the first medical scan does not necessarily give enough details on the course or status of the anomaly. The method proposed in this study can locate changes from GPR C-scans with a few seconds, and the preliminary knowledge about the anomaly, i.e., size and position, can be obtained. Afterwards, more investigation should be conducted on the detected locations: for instance, referring to radargrams or carrying out inversions.

This study illustrates the necessity of conducting temporal GPR surveys for subsurface diagnosis, therefore a practical workflow (Figure 6-12) of time-lapse surveys is proposed. The first step is comparing two C-scans – either a C-scan pair of t_0, and t_{n-1}, or a C-scans pair of t_{n-1}, and t_n, then major dissimilarities that indicate potential defects can be identified and extracted. If there is no significant change, that means the survey area is healthy and safe, if the previous image is assumed to be "safe". The second step is to verify the detection result with relevant personnel: whether there is any construction work was conducted in this area before. If yes, the change detection result is likely to be TP. Otherwise, further investigation should be implemented. In this way, the condition of the subsurface is tracked continually, and a "medical record" can be built along time. In conclusion, change detection from C-scans can narrow down the areas to be investigated and further facilitate the efficiency of subsurface diagnosis.
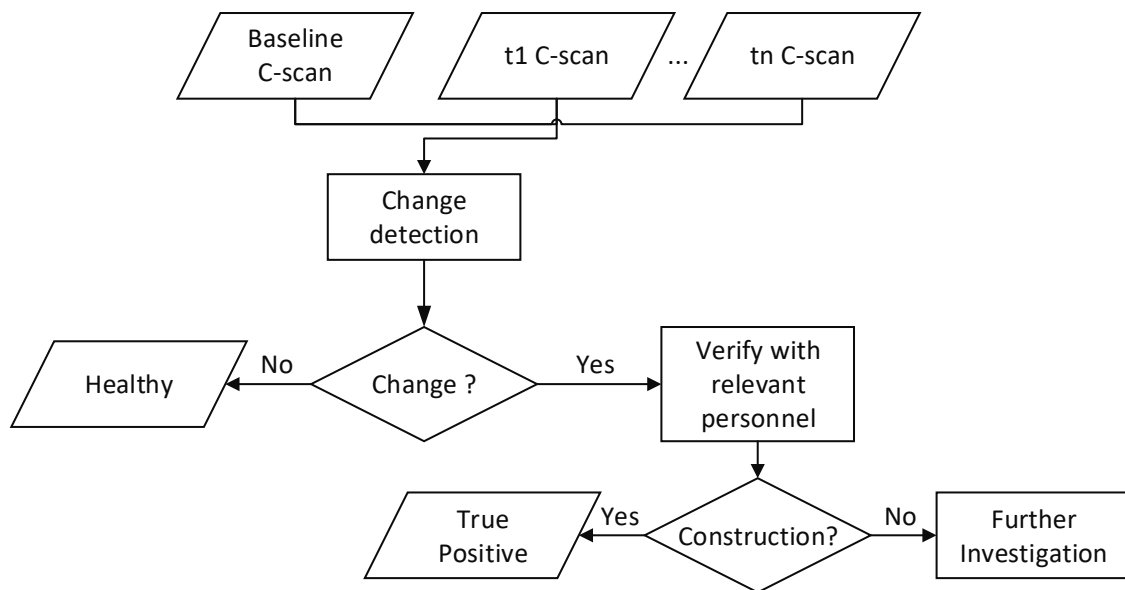
Figure 6-12 Proposed workflow for temporal diagnosis on the subsurface

6.4.3 Improve the reliability of time-lapse C-scans

Even though with the standardized workflow (Figure 3-3), and the subsurface correctly imaged, the variations among temporal GPR C-scans are still inevitable (Figure 6-4). Apart from the variation of the properties of the host material, the variation among time-lapse C-scans is mainly caused by the fact that the survey paths of every survey are very different, as shown in Figure 6-3 – which is always the case in real practices. Therefore, the survey orientation of a measurement point may vary among surveys of different times, and the polarization of the GPR signal changes accordingly. Moreover, the density of GPR measurements of the 2nd survey was much lower. The denser the GPR measurements, the closer the C-scan to reality. The lower sample density in the 2nd survey introduced more artificial interpretation in the interpolation step. As discussed in Chapter 3, the blank area is filled up by interpolation, and interpolation aggravates the discrepancy caused by different survey paths: if there is a contrast between true measurements of different survey times, the calculated measurements are unlikely to coincide, therefore, discrepancies are introduced into blank areas.

Currently, in large-scale surveys, the free-gridding survey guided by a positioning system is widely adopted, because it is not realistic to have a detail survey-grid drawn on the ground. A guiding system that can guarantee constant survey paths is beneficial for eliminating the unnecessary discrepancies among time-lapse C-scans. Ching (2019) developed a guiding system that can guide the GPR operators to walk along a pre-defined grid. With the geometry information as well as survey profile spacing of the survey site being inputted into the system,

the system automatically calculates the coordinates of each survey profile. During the GPR survey, the positioning system mounted on the antenna keeps delivering real-time positions to the guiding system. And the guiding system calculates the distance and shifting angle between the current operator's position and the pre-defined grid. Alarms and guidance on adjustments are given to the operator when a shift happens. Figure 6-13 illustrates that with the guiding system, the survey paths are much closer to the orthogonal desired grid. Therefore, the measurements are distributed evenly.

a

b
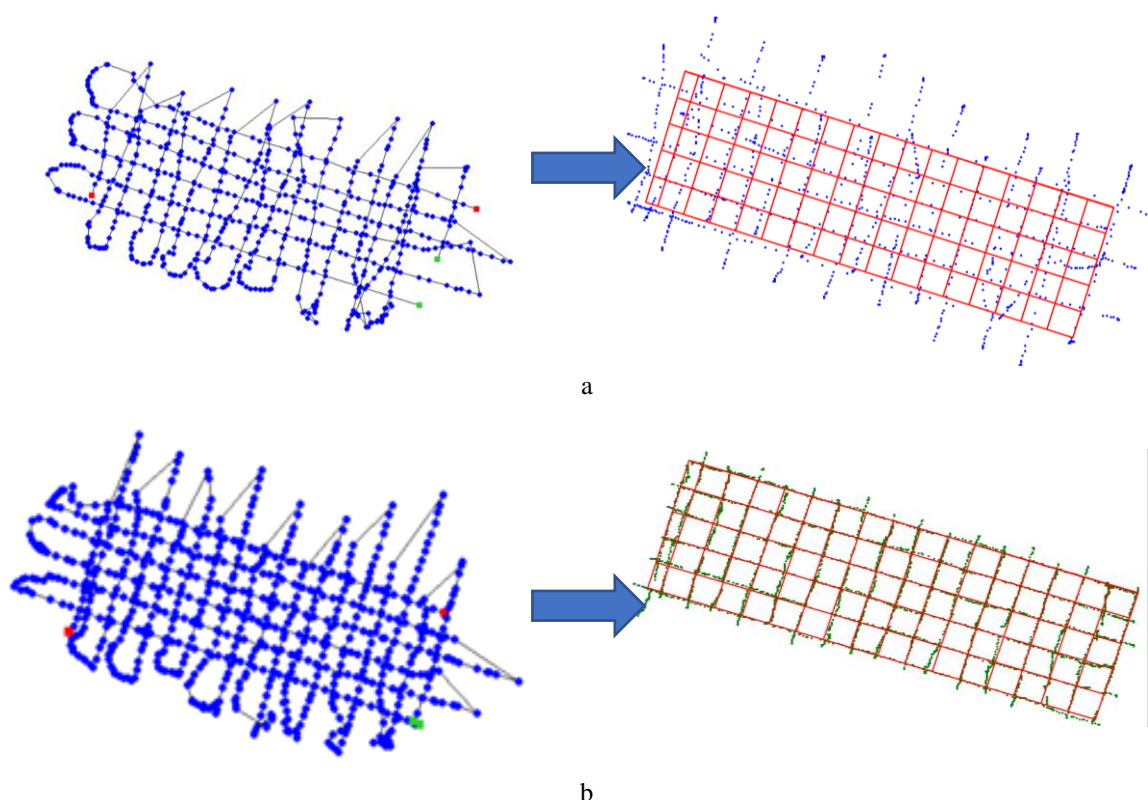
Figure 6-13 Comparison of survey paths without (a) and with (b) the guiding system (Ching, 2019)

A trial test was conducted for the field site area: survey the site with the guiding system. The utility presents a straight in C-scans produced with the guiding system (Figure 6-14), which means the error of the scan-lag is reduced significantly. How the accuracy and precision of change detection are affected by using guiding systems deserves further investigations. In short, in temporal change detection, it is of vital importance to control the random variations among time-lapse C-scans.

<center>a   b</center>
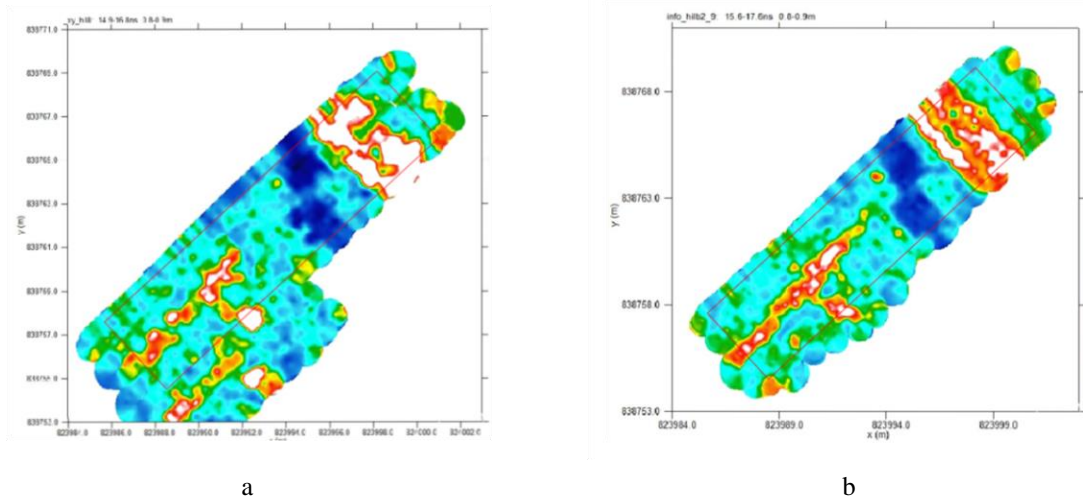
Figure 6-14 Comparison of C-scans of surveys without (a) or with (b) guiding system (Ching, 2019)

6.5 Summary and contribution

The GPR data of 2nd survey of the site case was tested with the program of void identification that was introduced in Chapter 5. Although some local high reflections were detected, they did not coincide with the changed area. The local anomalies detected by the void recognition from C-scan consistently existed – they were not newly added voids. Thus, the site in the Royal Palm was reported as void-free.
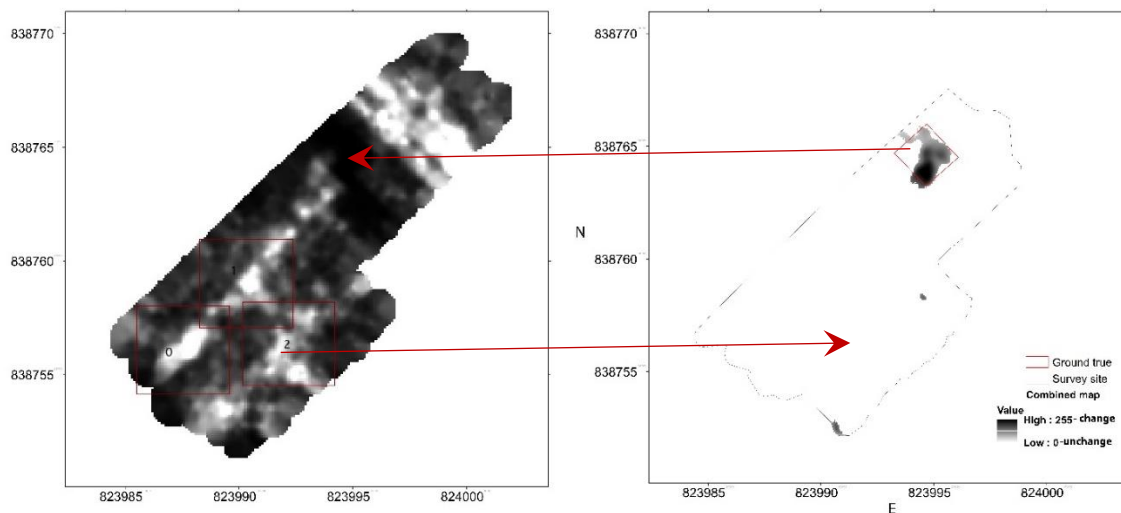
Figure 6-15 The result of the void identification from the C-scan of the Royal Palm

In the test, the TN (true negative – save) was 100%. This experiment proved that the false alarms caused by fixed structures or scatterings could be eliminated by time-lapse surveys. The

<center>117</center>

study served as a prototype and demonstrated the feasibility of conducting temporal diagnosis on the subsurface structure.

Change detection is a novel idea in the GPR world because 3D imaging by GPR is not popular and it is most often used when a problem on the surface becomes apparent and visual. So it is in general not perceived as a diagnostic tool requiring both a baseline survey and a change-detection survey. The content of this chapter, based on the 3D imaging criteria in Chapter. 3 and void identification in Chapter.5, paves the way for GPR change detection depending on the temporal comparison of GPR C-scans, thus turning GPR from merely an imaging tool to a diagnostic tool.

Chapter 7 Conclusions

The research systematically explored GPR imaging techniques and applications used in the diagnosis of subsurface defects. Computer vision and image processing techniques were introduced into GPR imaging, which made this the first study of its kind. Health medical records of urban subsurface can be established with time-lapse GPR measurements.

7.1 Main findings

(1) A standardized workflow on 3D GPR imaging criteria (Chapter 3)

The specific guidance provided in the workflow were summarized using 25 experiments, and it was demonstrated that the construction of GPR 3D images (C-scans) should be object-oriented and case-specific. This study reviewed GPR imaging theories as well as important parameters that affect GPR imaging quality, and identified the object characteristics that have a crucial influence on imaging quality. A relationship between object and imaging parameters was established so as to define a suitable range for each parameter. When reliable C-scans are produced using a standardized workflow, more meaningful interpretations can then be made using those images, thus bringing the unseen subsurface world into view. The standardized GPR imaging workflow produced by this research can produce convincing images with fewer human judgements, which is clearly beneficial to the survey industry.

(2) Specific GPR responses generated by subsurface voids.

Subsequent to generating reliable C-scans in (1) through the standardized workflow, the key GPR signatures obtained from some typical subsurface structures, with a specific focus on subsurface air voids. Air voids with different widths and sizes in soils were experimentally and numerically simulated in order to study the GPR responses that are free from scattering. It was found that when different ratios of void spread (s) to radar footprint (z) were applied, four main patterns would be produced, as follows: hyperbola ($s/z < 2$), cross ($2 < s/z < 4$), bowl-shape ($4 < s/z < 6$) and plain-reverberation ($s/z > 6$). A site experiment conducted on a section of road demonstrated that GPR responses would be distorted by the road structure and nearby utilities. Then, two types of typical road structures, a bituminous road and a concrete road, were modelled in order to observe the impact of void geometries. With knowledge of the effects of air voids on GPR signals, the efficiency of void identification can be improved in GPR data.

(3) Develop a workflow that integrates pattern recognition techniques in order to identify subsurface voids from GPR data (Chapter 5)

The workflow imitated the human judgment process, and integrated a pyramid pattern recognition technique in order to search for GPR responses generated by air-filled voids. The GPR responses of air-filled voids were investigated in advance. A void appeared as a local anomaly with high reflection intensity in C-scans. Different ratios of void size and GPR signal wavelength resulted in different patterns in B-scans. A database of void patterns for both C-scans and B-scans was established, and the pyramid pattern recognition method – with pixel value or gradient used for object identification – was used to search for such GPR responses automatically. In this way, preliminary knowledge of the void location and void size can be obtained without human intervention. Two validation experiments were conducted and produced promising results. Known voids were in general successfully identified: the true positive rate was 65%. Given the demanding and heavy workload involved in subsurface health inspections, the workflow has been proven to be efficient and effective. The study result raised the possibility of conducting city-scale and full-coverage subsurface health inspections.

(4) Develop a workflow that uses image change detection techniques to extract subsurface defects from time-lapse GPR depth slice images (Chapter 6)

The developed workflow consisted of two main steps, in which the first step was the image registration and intensity normalization. By analysing the causes of positioning errors, time-lapse GPR C-scans can be correctly georeferenced and co-registered. The workflow used benchmark points on the ground to normalize the global intensity of time-lapse GPR C-scans. The second step classified pixels into changed or unchanged. Two kinds of information were considered in order to construct two difference-maps: they were changes in the intensity and the object structure. Appropriate filters were applied to the difference map to remove the isolated elements while preserving edges. K-means clustering was responsible for extracting pixels that possess both intensity changes and object structure changes – i.e. in locations where potential subsurface defects most likely to have occurred. The workflow was verified using a real case study, and the area of excavation with pipe replacement and different types of soil backfill was successfully identified. The performance of the proposed workflow was promising in excluding small and random scattering noise, which was the main challenge in time-lapse

GPR image observation. The study served as a prototype and demonstrated the feasibility and necessity of conducting temporal diagnosis on the subsurface structure.

In summary, this study was a pilot study aimed at improving the GPR diagnosis efficiency and accuracy of the interpretation of large datasets, as well as eliminating the human biases as much as possible. It further proved the feasibility for the continuous health-check of the urban subsurface with GPR, paving the way for the city-scale underground diagnosis.

The study indicated the demand for dense measurements and consistent survey paths in the temporal observation. The novel multi-array system can solve the problem, as it can collect full-resolution measurements in a non-stop manner. In addition, this study applied the sensitivity evaluation, leading to evaluation of TP, TN, FP, and FN to calculate TPR and FPR as an important indicator of survey accuracy. Such application of the sensitivity evaluation is rare in the near-surface geophysical surveys, due to the limited quantity of ground truthing.

7.2 Challenges and recommendation on future work

This research focuses on processes and applications relating to these three typical GPR data visualizations, but there are many other types of visualizations in existence. Semantic presentations of GPR data that only display target content but neglect to consider insignificant signals deserve further investigation. In short, the effectiveness of diagnosis with GPR can be increased through three ways, they are:

1) enriching the fingerprint database through more ground truthing validations.

It is necessary to establish a comprehensive database that records the GPR signature of each type of subsurface defect/void with different types of overlaid materials. More quantitative forward models – both numerical simulation and empirical experiments – must be conducted to depict how these subsurface defects are presented in GPR data.

2) optimization of algorithms.

In both GPR pattern recognition and temporal GPR observation, special attention should be paid to the non-systematic variations among GPR data. Coincide survey paths (Chapter 6.4.3) and imaging criteria (Figure 3-2) should be applied in temporal surveys to avoid random dissimilarities among time-lapse C-scans. Algorithms should be robust enough to exclude speckles and mild pattern geometry variations. Apart from the K-means attempted in this thesis,

it would be worthwhile to improve methods or algorithms that are specifically tailored to GPR imaging.

3) adopting the approaches of machine learning.

The subsurface environment is complicated, and the GPR reflections are affected by various factors. When the comprehensive fingerprint database is established, the involvement of machine learning is expected. The approach of machine learning can sort the signal features, process the representation models, as well as extract the meaningful information from the large dataset of the subsurface survey with GPR, in a fully automatic manner. It can improve the efficiency of the diagnosis significantly.

In conclusion, this PhD research establishes a health diagnosis system for the urban subsurface using spatial and temporal GPR C-scans and B-scans. And the system was validated with experiments. The standardized workflow for C-scan generation is the foundation for reliable GPR survey. With a series time-lapse C-scans, the changed area can be detected with change detection method. Then the suspected area needs further investigation, such as match with patterns in defect database. With the system, the GPR survey and the data interpretation can be conducted in a semi-automatic manner. Human subjective interventions and high labour costs of interpretation are also reduced via the suggested approach. The system adopts and customizes image processing and computer visualisation techniques, facilitates the efficiency and effectiveness of GPR survey in localized areas, and paves the way for upscaling the GPR surveys to city scale.

References

Adelson, E. H., Anderson, C. H., Bergen, J. R., Burt, P. J., & Ogden, J. M. (1984). Pyramid methods in image processing. RCA engineer, 29(6), 33-41.

Al-Nuaimy, W., Huang, Y., Nakhkash, M., Eriksen, A., Fang, M. T. C., & Nguyen, V. T. (2000). Automatic detection of buried utilities and solid objects with GPR using neural networks and pattern recognition. Journal of Applied Geophysics, 43, 157-165. doi:S0926-9851 99 00055-5

Al-Qadi, I., & Lahouar, S. (2005). Measuring layer thicknesses with GPR–Theory to practice. Construction and Building Materials, 19(10), 763-772.

Alani, A. M., Aboutalebi, M., & Kilic, G. (2013). Applications of ground penetrating radar (GPR) in bridge deck monitoring and assessment. Journal of Applied Geophysics, 97, 45-54.

Allroggen, N., van Schaik, N. L. M. B., & Tronicke, J. (2015). 4D ground-penetrating radar during a plot scale dye tracer experiment. Journal of Applied Geophysics, 118, 139-144. doi:10.1016/j.jappgeo.2015.04.016

Annan, A., & Cosway, S. (1992). Simplified GPR beam model for survey design *SEG Technical Program Expanded Abstracts 1992* (pp. 356-359): Society of Exploration Geophysicists.

Annan, A. P. (2002). GPR—History, Trends, and Future Developments. Subsurface Sensing Technologies and Applications, 3(4).

Annan, A. P. (2004). Ground Penetrating Radar Applications, Principles, Procedures. Mississauga, Canada: Sensors and Software.

ASTM D6432 (2011) Standard Guide for Using the Surface Ground Penetrating Radar Method for Subsurface Investigation

ASTM D6432-11 (2011) Standard Guide for Using the Surface Ground Penetrating Radar Method for Subsurface Investigation

ASTM D6432-11. (2011). Standard Guide for Using the Surface Ground Penetrating Radar Method for Subsurface Investigation. ASTM International, West Conshohocken, PA, 2011, www.astm.org. doi:10.1520/d6432-11

Ayala-Cabrera, D., Herrera, M., Izquierdo, J., & Pérez-García, R. (2011). Location of buried plastic pipes using multi-agent support based on GPR images. Journal of Applied Geophysics, 75(4), 679-686. doi:10.1016/j.jappgeo.2011.09.024

Baker, J. A., Anderson, N. L., & Pilles, P. J. (1997). Ground-penetrating radar surveying in support of archeological site investigations. Computers & Geosciences, 23(10), 1093-1099.

Barraca, N., Almeida, M., Varum, H., Almeida, F., & Matias, M. S. (2016). A case study of the use of GPR for rehabilitation of a classified Art Deco building: The InovaDomus house. Journal of Applied Geophysics, 127, 1-13. doi:10.1016/j.jappgeo.2016.02.002

Bernabini, M., Pettinelli, E., Pierdicca, N., Piro, S., & Versino, L. (1995). Field experiments for characterization of GPR antenna and pulse propagation. Journal of Applied Geophysics, 33(1-3), 63-76.

Birken, R., Miller, D. E., Burns, M., Albats, P., Casadonte, R., Deming, R., . . . Oristaglio, M. (2002). Efficient large-scale underground utility mapping in New York City using a multichannel ground-penetrating imaging radar system. Paper presented at the Ninth International Conference on Ground Penetrating Radar (GPR2002).

Bishop, C. M. (2012). Pattern recognition and machine learning, 2006. 대한토목학회지, 60(1), 78-78.

Blaschke, T. (2010). Object based image analysis for remote sensing. ISPRS Journal of photogrammetry and remote sensing, 65(1), 2-16.

Boashash, B. (2015). Time-frequency signal analysis and processing: a comprehensive reference: Academic Press.

Böniger, U., & Tronicke, J. (2010a). Improving the interpretability of 3D GPR data using target–specific attributes: application to tomb detection. Journal of Archaeological Science, 37(4), 672-679. doi:10.1016/j.jas.2010.01.013

Böniger, U., & Tronicke, J. (2010b). Symmetry based 3D GPR feature enhancement and extraction. Paper presented at the Ground Penetrating Radar (GPR), 2010 13th International Conference on.

Bovolo, F., & Bruzzone, L. (2007). A theoretical framework for unsupervised change detection based on change vector analysis in the polar domain. IEEE Transactions on Geoscience and Remote Sensing, 45(1), 218-236.

Broughton, S., & Bryan, K. Discrete Fourier Analysis and Wavelets: Application to Signal and Image Processing. 2009: J. Wiley & Sons, Hoboken, NJ.

Bungey, J. H. (2004). Sub-surface radar testing of concrete: a review. Construction and Building Materials, 18(1), 1-8. doi:10.1016/s0950-0618(03)00093-x

Canty, M. J. (2014). Image analysis, classification and change detection in remote sensing: with algorithms for ENVI/IDL and Python: Crc Press.

Casas, A., Lazaro, R., Vilas, M., & Busquet, E. (1996). Detecting karstic cavities with ground penetrating radar at different geological environments in Spain. Paper presented at the Proceedings of the 6th International Conference of Ground Penetrating Radar.

Cassidy, N. J., Eddies, R., & Dods, S. (2011). Void detection beneath reinforced concrete sections: The practical application of ground-penetrating radar and ultrasonic techniques. Journal of Applied Geophysics, 74(4), 263-276. doi:10.1016/j.jappgeo.2011.06.003

Celik, T. (2009). Unsupervised change detection in satellite images using principal component analysis and k-means clustering. IEEE Geoscience and Remote Sensing Letters, 6(4), 772-776.

Cerveny, V. (2005). Seismic ray theory: Cambridge university press.

Chan, C. Y., & Knight, R. J. (2001). Laboratory measurements of electromagnetic wave velocity in layered sands. Water resources research, 37(4), 1099-1105.

Chang, K. W. R. (2016). Real-time Tracking and Error Analysis of Ground Penetrating Radar Position by Auto-tracking total station. (MSc), The Hong Kong Polytechnic University.

Ching, G. P. H. (2019). Development and Validation of a Ground Penetrating Radar (GPR) Virtual guiding system for subsurface 3D imaging. (BsC of Geomatics), The Hong Kong Polytechnie University.

Coppin, P., Jonckheere, I., Nackaerts, K., Muys, B., & Lambin, E. (2004). Review ArticleDigital change detection methods in ecosystem monitoring: a review. International Journal of Remote Sensing, 25(9), 1565-1596.

Cullity, B. D., & Graham, C. D. (2008). Introduction to Magnetic Materials (Vol. 2).

Daniels, D. J. (1996). Surface-penetrating radar. Electronics & Communication Engineering Journal, 8(4), 165-182.

Daniels, J. J., Grumman, D. L., & Vendl, M. A. (1997). Coincident antenna three-dimensional GPR. Journal of Environmental and Engineering Geophysics, 2(1), 1-9.

Davidson, D. B. (2010). Computational electromagnetics for RF and microwave engineering: Cambridge University Press.

Davis, J., & Annan, A. (1989). Ground-penetrating radar for high resolution mapping of soil and rock stratigraphy: Geophysical Prospecting. Geophysical prospecting, 37(5), 531-551.

De Souza, T., Annan, A., Redman, J., & Hu, N. (2004). Monitoring the GPR response of curing concrete. Paper presented at the 16th World conference on NDT, Montreal. Canada.

Farley, M., Water, S., Supply, W., Council, S. C., & Organization, W. H. (2001). Leakage management and control: a best practice training manual.

Fawcett, T. (2006). An introduction to ROC analysis. Pattern recognition letters, 27(8), 861-874.

Forgy, E. W. (1965). Cluster analysis of multivariate data: efficiency versus interpretability of classifications. biometrics, 21, 768-769.

Gamba, P., & Lossani, S. (2000). Neural detection of pipe signatures in ground penetrating radar images. IEEE Transactions on Geoscience and Remote Sensing, 38(2), 790-797.

Gerber, R., Salat, C., Junge, A., & Felix-Henningsen, P. (2007). GPR-based detection of Pleistocene periglacial slope deposits at a shallow-depth test site. Geoderma, 139(3-4), 346-356. doi:10.1016/j.geoderma.2007.02.014

Ghasemi, F. S. A., & Abrishamian, M. (2007). A novel method for FDTD numerical GPR imaging of arbitrary shapes based on Fourier transform. NDT & E International, 40(2), 140-146.

Giannopoulos, A. (2005). Modelling ground penetrating radar by GprMax. Construction and Building Materials, 19(10), 755-762. doi:10.1016/j.conbuildmat.2005.06.007

Gong, P., & Howarth, P. (1992). Land-use classification of SPOT HRV data using a cover-frequency method. International Journal of Remote Sensing, 13(8), 1459-1471.

Goodman, D. (2017). GPR-SLICE Software Manual.

Goodman, D., Nishimura, Y., & Rogers, J. D. (1995). GPR (Ground Penetrating Radar) Time Slices in Archaeological Prospection. Archaeological Prospection, 2(January), 85-89.

Goodman, D., & Piro, S. (2013). GPR remote sensing in archaeology (Vol. 9): Springer.

Gopal, S., & Woodcock, C. (1996). Remote sensing of forest change using artificial neural networks. IEEE Transactions on Geoscience and Remote Sensing, 34(2), 398-404.

Gou, S., Zhuang, X., Zhu, H., & Yu, T. (2013). Parallel sparse spectral clustering for SAR image segmentation. IEEE Journal of Selected Topics in Applied Earth Observations and Remote Sensing, 6(4), 1949-1963.

Grasmueck, M., Quintà, M. C., Pomar, K., & Eberli, G. P. (2013). Diffraction imaging of sub-vertical fractures and karst with full-resolution 3D Ground-Penetrating Radar. Geophysical prospecting, 61(5), 907-918. doi:10.1111/1365-2478.12004

Grasmueck, M., Weger, R., & Horstmeyer, H. (2005). Full-resolution 3D GPR imaging. Geophysics, 70(1), K12-K19.

Hao, T., Rogers, C. D. F., Metje, N., Chapman, D. N., Muggleton, J. M., Foo, K. Y., . . . Saul, A. J. (2012). Condition assessment of the buried utility service infrastructure. Tunnelling and Underground Space Technology, 28, 331-344. doi:10.1016/j.tust.2011.10.011

Harrington, R. F. (1993). Field computation by moment methods: Wiley-IEEE Press.

Hartigan, J. A., & Wong, M. A. (1979). Algorithm AS 136: A k-means clustering algorithm. Journal of the Royal Statistical Society. Series C (Applied Statistics), 28(1), 100-108.

Hastings, F. D., Schneider, J. B., & Broschat, S. L. (1995). A Monte-Carlo FDTD technique for rough surface scattering. IEEE transactions on antennas and propagation, 43(11), 1183-1191.

Hastings, F. D., Schneider, J. B., & Broschat, S. L. (1996). Application of the perfectly matched layer (PML) absorbing boundary condition to elastic wave propagation. The Journal of the Acoustical Society of America, 100(5), 3061-3069.

Hong, S., Wiggenhauser, H., Helmerich, R., Dong, B., Dong, P., & Xing, F. (2017). Long-term monitoring of reinforcement corrosion in concrete using ground penetrating radar. Corrosion Science, 114, 123-132. doi:10.1016/j.corsci.2016.11.003

Huang, C., Song, K., Kim, S., Townshend, J. R., Davis, P., Masek, J. G., & Goward, S. N. (2008). Use of a dark object concept and support vector machines to automate forest cover change analysis. Remote Sensing of Environment, 112(3), 970-985.

Hugenschmidt, J., & Kalogeropoulos, A. (2009). The inspection of retaining walls using GPR. Journal of Applied Geophysics, 67(4), 335-344. doi:10.1016/j.jappgeo.2008.09.001

Hussain, M., Chen, D., Cheng, A., Wei, H., & Stanley, D. (2013). Change detection from remotely sensed images: From pixel-based to object-based approaches. ISPRS Journal of photogrammetry and remote sensing, 80, 91-106.

HyD. (2017a). Typical Bituminous Pavement Construction. Retrieved from https://www.hyd.gov.hk/en/publications_and_publicity/publications/technical_document/hyd_standard_drawings/doc/section_1/pdf/H1101C.pdf

HyD. (2017b). Typical Concrete Pavement Construction. Retrieved from https://www.hyd.gov.hk/en/publications_and_publicity/publications/technical_document/hyd_standard_drawings/doc/section_1/pdf/H1102B.pdf

Jensen, J. R., & Lulla, K. (1987). Introductory digital image processing: a remote sensing perspective.

Jiao, Y., McMechan, G. A., & Pettinell, E. i. (2000). In situ 2-D and 3-D measurements of radiation patterns of half-wave diphole GPR antennas. Journal of Applied Geophysics, 43, 69-89. doi:S0926-9851 99 00048-8

Johansen, K., Arroyo, L. A., Phinn, S., & Witte, C. (2010). Comparison of geo-object based and pixel-based change detection of riparian environments using high spatial resolution multi-spectral imagery. Photogrammetric Engineering & Remote Sensing, 76(2), 123-136.

Jol, H. M. (2009). Ground Penetrating Radar Theory and Applications: Oxford: Elsevier.

Kofman, L. (1994). Use of ground penetrating radar in geotechnical applications. Paper presented at the Proceedings of the 12th Conference of the Israel Association for the Advancement of Mineral Engineering, Eilat.

Kofman, L., Ronen, A., & Frydman, S. (2006). Detection of model voids by identifying reverberation phenomena in GPR records. Journal of Applied Geophysics, 59(4), 284-299.

Kowalsky, M. B., Finsterle, S., Peterson, J., Hubbard, S., Rubin, Y., Majer, E., . . . Gee, G. (2005). Estimation of field-scale soil hydraulic and dielectric parameters through joint inversion of GPR and hydrological data. Water resources research, 41(11).

LabVIEW – See it. Solve it.s. (2018). Retrieved from http://www.ni.com/en-us.html

Lai, W.-L. W., Kind, T., Kruschwitz, S., Wöstmann, J., & Wiggenhauser, H. (2014). Spectral absorption of spatial and temporal ground penetrating radar signals by water in construction materials. NDT & E International, 67, 55-63. doi:10.1016/j.ndteint.2014.06.009

Lai, W., Tsang, W., Fang, H., & Xiao, D. (2006). Experimental determination of bulk dielectric properties and porosity of porous asphalt and soils using GPR and a cyclic moisture variation technique. Geophysics, 71(4), K93-K102.

Lai, W. L., Kind, T., Stoppel, M., & Wiggenhauser, H. (2013). Measurement of Accelerated Steel Corrosion in Concrete Using Ground-Penetrating Radar and a Modified Half-Cell Potential Method. Journal of infrastructure systems, 19(2), 205-220. doi:10.1061/(asce)is.1943-555x.0000083

Lai, W. L., & Poon, C. S. (2012). Applications of Nondestructive Evaluation Techniques in Concrete Inspection. HKIE Transactions, 19(4), 34-41. doi:10.1080/1023697X.2012.10669003

Lai, W. W.-L., Dérobert, X., & Annan, P. (2018a). A review of Ground Penetrating Radar application in civil engineering: A 30-year journey from Locating and Testing to Imaging and Diagnosis. NDT & E International.

Lai, W. W.-L., Kind, T., Sham, J. F.-C., & Wiggenhauser, H. (2016a). Correction of GPR wave velocity at different oblique angles between traverses and alignment of line objects in a common offset antenna setting. NDT & E International, 82, 36-43.

Lai, W. W.-L., Kind, T., Sham, J. F.-C., & Wiggenhauser, H. (2016b). Correction of GPR wave velocity at different oblique angles between traverses and alignment of line objects in a common offset antenna setting. NDT and E International, 82, 36-43. doi:10.1016/j.ndteint.2016.03.003

Lai, W. W., Chang, R. K., & Sham, J. F. (2017a). Detection and imaging of city's underground void by GPR. Paper presented at the Advanced Ground Penetrating Radar (IWAGPR), 2017 9th International Workshop on.

Lai, W. W., Chang, R. K., & Sham, J. F. (2018b). A blind test of nondestructive underground void detection by ground penetrating radar (GPR). Journal of Applied Geophysics, 149, 10-17.

Lai, W. W., Ho, M. L.-Y., Chang, R. K., Sham, J. F., & Poon, C.-S. (2017b). Tracing and imaging minor water seepage of concealed PVC pipe in a reinforced concrete wall by high-frequency ground penetrating radar. Construction and Building Materials, 151, 840-847.

Lai, W. W. L., Chang, R. K. W., Sham, J. F. C., & Pang, K. (2016c). Perturbation mapping of water leak in buried water pipes via laboratory validation experiments with high-frequency ground penetrating radar (GPR). Tunnelling and Underground Space Technology, 52, 157-167. doi:10.1016/j.tust.2015.10.017

Lambot, S., Slob, E. C., van den Bosch, I., Stockbroeckx, B., & Vanclooster, M. (2004). Modeling of ground-penetrating radar for accurate characterization of subsurface electric properties. IEEE Transactions on Geoscience and Remote Sensing, 42(11), 2555-2568.

Leckebusch, J. (2003). Ground-penetrating radar: a modern three-dimensional prospection method. Archaeological Prospection, 10(4), 213-240.

Leckebusch, J., & Peikert, R. (2001). Investigating the true resolution and three-dimensional capabilities of ground-penetrating radar data in archaeological surveys: measurements in a sand box. Archaeological Prospection, 8(1), 29-40.

Lee, S. U., Chung, S. Y., & Park, R. H. (1990). A comparative performance study of several global thresholding techniques for segmentation. Computer Vision, Graphics, and Image Processing, 52(2), 171-190.

Léger, E., Saintenoy, A., & Coquet, Y. (2014). Hydrodynamic parameters of a sandy soil determined by ground-penetrating radar inside a single ring infiltrometer. Water resources research, 50(7), 5459-5474. doi:10.1002/2013wr014226

Leucci, G., & Negri, S. (2006). Use of ground penetrating radar to map subsurface archaeological features in an urban area. Journal of Archaeological Science, 33(4), 502-512. doi:10.1016/j.jas.2005.09.006

Leucci, G., Negri, S., & Carrozzo, M. T. (2003). Ground Penetrating Radar (GPR): an application for evaluating the state of maintenance of the building coating. Annals of Geophysics, 46(3).

Lillesand, T., Kiefer, R. W., & Chipman, J. (2014). Remote sensing and image interpretation: John Wiley & Sons.

Liu, J. G., & Mason, P. J. (2013). Essential image processing and GIS for remote sensing: John Wiley & Sons.

Lu, D., Mausel, P., Brondizio, E., & Moran, E. (2004). Change detection techniques. International Journal of Remote Sensing, 25(12), 2365-2401.

Lualdi, M., Zanzi, L., & Binda, L. (2003). Acquisition and processing requirements for high quality 3D reconstructions from GPR investigations. Paper presented at the Proceedings, International Symposium Non-Destructive Testing in Civil Engineering (NDT-CE), Berlin, Germany.

Lunetta, R. S., Knight, J. F., Ediriwickrema, J., Lyon, J. G., & Worthy, L. D. (2006). Land-cover change detection using multi-temporal MODIS NDVI data. Remote Sensing of Environment, 105(2), 142-154.

Maas, C., & Schmalzl, J. (2013). Using pattern recognition to automatically localize reflection hyperbolas in data from ground penetrating radar. Computers & Geosciences, 58, 116-125. doi:https://doi.org/10.1016/j.cageo.2013.04.012

MacKay, D. J., & Mac Kay, D. J. (2003). Information theory, inference and learning algorithms: Cambridge university press.

MacLean, W. J., & Tsotsos, J. K. (2008). Fast pattern recognition using normalized grey-scale correlation in a pyramid image representation. Machine Vision and Applications, 19(3), 163-179.

MacQueen, J. (1967). Some methods for classification and analysis of multivariate observations. Paper presented at the Proceedings of the fifth Berkeley symposium on mathematical statistics and probability.

Malagodi, S., Orlando, L., Piro, S., & Rosso, F. (1996). Location of archaeological structures using GPR method: three-dimensional data acquisition and radar signal processing. Archaeological Prospection, 3(1), 13-23.

Marchesini, P., & Grasmueck, M. (2015). The impact of high-density spatial sampling versus antenna orientation on 3D GPR fracture imaging. Near Surface Geophysics, 13(2061). doi:10.3997/1873-0604.2015007

Melgani, F., Moser, G., & Serpico, S. B. (2002). Unsupervised change-detection methods for remote-sensing images. Optical Engineering, 41(12), 3288-3298.

Metwaly, M. (2015). Application of GPR technique for subsurface utility mapping: A case study from urban area of Holy Mecca, Saudi Arabia. Measurement, 60, 139-145. doi:10.1016/j.measurement.2014.09.064

Millington, T. M., & Cassidy, N. J. (2010). Optimising GPR modelling: A practical, multi-threaded approach to 3D FDTD numerical modelling. Computers & Geosciences, 36(9), 1135-1144.

NDT.net. (2011). Determination of dielectric properties of insitu concrete at radar frequencies. Retrieved from https://www.ndt.net/index.php

NI Vision - Pattern Matching Techniques. (2018). Retrieved from http://zone.ni.com/reference/en-XX/help/372916P-01/nivisionconcepts/pattern_matching_techniques/

Nojavan, S., & Yuan, F.-G. (2006). Damage imaging of reinforced concrete structures using electromagnetic migration algorithm. International Journal of Solids and Structures, 43(18-19), 5886-5908. doi:10.1016/j.ijsolstr.2005.08.017

Nuzzo, L., Leucci, G., Negri, S., Teresa Carrozzo, M., & Quarta, T. (2002). Application of 3D Visualization Techniques in the Analysis of GPR data for Archaeology. Annals of Geophysics, 45(2).

Orlando, L., & Slob, E. (2009). Using multicomponent GPR to monitor cracks in a historical building. Journal of Applied Geophysics, 67(4), 327-334. doi:10.1016/j.jappgeo.2008.09.003

Otsu, N. (1979). A threshold selection method from gray-level histograms. IEEE transactions on systems, man, and cybernetics, 9(1), 62-66.

Panisova, J., Murín, I., Pašteka, R., Haličková, J., Brunčák, P., Pohánka, V., . . . Milo, P. (2016). Geophysical fingerprints of shallow cultural structures from microgravity and GPR measurements in the Church of St. George, Svätý Jur, Slovakia. Journal of Applied Geophysics, 127, 102-111. doi:10.1016/j.jappgeo.2016.02.009

Pasolli, E., Melgani, F., & Donelli, M. (2009). Automatic analysis of GPR images: A pattern-recognition approach. IEEE Transactions on Geoscience and Remote Sensing, 47(7), 2206-2217.

Pavlidis, T. (2013). Structural pattern recognition (Vol. 1): Springer.

Pérez-Gracia, V., Di Capua, D., González-Drigo, R., Caselles, O., Pujades, L., & Salinas, V. (2010). GPR resolution in Cultural Heritage applications. Paper presented at the Ground Penetrating Radar (GPR), 2010 13th International Conference on.

Pérez-Gracia, V., Di Capua, D., González-Drigo, R., & Pujades, L. (2009). Laboratory characterization of a GPR antenna for high-resolution testing: Radiation pattern and vertical resolution. NDT & E International, 42(4), 336-344.

Pérez-Gracia, V., González-Drigo, R., & Di Capua, D. (2008). Horizontal resolution in a non-destructive shallow GPR survey: An experimental evaluation. NDT & E International, 41(8), 611-620.

Permuter, H., Francos, J., & Jermyn, I. (2006). A study of Gaussian mixture models of color and texture features for image classification and segmentation. Pattern Recognition, 39(4), 695-706.

Porsani, J. L., Ruy, Y. B., Ramos, F. P., & Yamanouth, G. R. B. (2012). GPR applied to mapping utilities along the route of the Line 4 (yellow) subway tunnel construction in São Paulo City, Brazil. Journal of Applied Geophysics, 80, 25-31. doi:10.1016/j.jappgeo.2012.01.001

Powers, D. M. (2011). Evaluation: from precision, recall and F-measure to ROC, informedness, markedness and correlation.

Ristic, A. V., Petrovacki, D., & Govedarica, M. (2009). A new method to simultaneously estimate the radius of a cylindrical object and the wave propagation velocity from GPR data. Computers & Geosciences, 35(8), 1620-1630.

Rowell, C. R., Pidlisecky, A., Irving, J. D., & Ferguson, R. J. (2010). Characterization of lava tubes using ground penetrating radar at Craters of the Moon National Monument, USA. Tech. rep. CREWES Research Report, 22, 1-18.

Sagnard, F., Norgeot, C., Derobert, X., Baltazart, V., Merliot, E., Derkx, F., & Lebental, B. (2016). Utility detection and positioning on the urban site Sense-City using Ground-Penetrating Radar systems. Measurement, 88, 318-330. doi:10.1016/j.measurement.2016.03.044

Schalkoff, R. J. (2007). Pattern recognition. Wiley Encyclopedia of Computer Science and Engineering.

Schneider, J. B. (2010). Understanding the Finite-Difference Time-Domain Method. Retrieved from www.eecs.wsu.edu/~schneidj/ufdtds

Sezgin, M., & Sankur, B. (2004). Survey over image thresholding techniques and quantitative performance evaluation. Journal of Electronic imaging, 13(1), 146-166.

Sham, J. F. C., & Lai, W. W. L. (2016). Development of a new algorithm for accurate estimation of GPR's wave propagation velocity by common-offset survey method. NDT and E International, 83, 104-113. doi:10.1016/j.ndteint.2016.05.002

Simi, A., Bracciali, S., & Manacorda, G. (2008). Hough transform based automatic pipe detection for array GPR: Algorithm development and on-site tests. Paper presented at the Radar Conference, 2008. RADAR'08. IEEE.

Singh, A. (1989). Review article digital change detection techniques using remotely-sensed data. International Journal of Remote Sensing, 10(6), 989-1003.

Solla, M., Lagüela, S., González-Jorge, H., & Arias, P. (2014). Approach to identify cracking in asphalt pavement using GPR and infrared thermographic methods: Preliminary findings. NDT & E International, 62, 55-65. doi:10.1016/j.ndteint.2013.11.006

Tanaka, T., O'Neill, A., & Goodman, D. (2009). Geophysics in archaeology: a scrapbook of worldwide data. Aust Soc Explor Geophys, 141, 25-29.

Topczewski, L., Fernandes, F. M., Cruz, P. J., & Lourenço, P. B. (2007). Practical implications of GPR investigation using 3D data reconstruction and transmission tomography. Journal of Building Appraisal, 3(1), 59-76.

Tou, J. T., & Gonzalez, R. C. (1974). Pattern recognition principles.

Townshend, J. R., Justice, C. O., Gurney, C., & McManus, J. (1992). The impact of misregistration on change detection. IEEE Transactions on Geoscience and Remote Sensing, 30(5), 1054-1060.

UUS-SPEC (2019) Specification for Non-destructive testing, surveying, imaging ad diagnosis for Underground Utilities 1,2 Ground Penetrating Radar. UUS-SPEC

Vidal, T., Castel, A., & François, R. (2004). Analyzing crack width to predict corrosion in reinforced concrete. Cement and Concrete Research, 34(1), 165-174. doi:10.1016/s0008-8846(03)00246-1

Volpi, M., Tuia, D., Bovolo, F., Kanevski, M., & Bruzzone, L. (2013). Supervised change detection in VHR images using contextual information and support vector machines. International Journal of Applied Earth Observation and Geoinformation, 20, 77-85.

Wang, Q. (2012). HMRF-EM-image: implementation of the hidden markov random field model and its expectation-maximization algorithm. arXiv preprint arXiv:1207.3510.

Warren, C., Giannopoulos, A., & Giannakis, I. (2016). gprMax: Open source software to simulate electromagnetic wave propagation for Ground Penetrating Radar. Computer Physics Communications, 209, 163-170.

Wu, H.-Y. (2015). Characterization of Shallow Subsurface Air-filled Voids by Ground Penetrating Radar. (Bachelor of Science), The Hong Kong Polytechnic University, Hong Kong.

Xie, F., Wu, C. G.-W., Lai, W. W.-L., & Sham, J. F.-C. (2018). Correction of multi-frequency GPR wave velocity with distorted hyperbolic reflections from GPR surveys of underground utilities. Tunnelling and Underground Space Technology, 76, 76-91.

Xie, X., Qin, H., Yu, C., & Liu, L. (2013). An automatic recognition algorithm for GPR images of RC structure voids. Journal of Applied Geophysics, 99, 125-134. doi:10.1016/j.jappgeo.2013.02.016

Xu, X., Zeng, Q., Li, D., Wu, J., Wu, X., & Shen, J. (2010). GPR detection of several common subsurface voids inside dikes and dams. Engineering Geology, 111(1-4), 31-42. doi:10.1016/j.enggeo.2009.12.001

Yee, K. (1966). Numerical solution of initial boundary value problems involving Maxwell's equations in isotropic media. IEEE transactions on antennas and propagation, 14(3), 302-307.

Yelf, R. (2004). Where is true time zero? Paper presented at the Ground Penetrating Radar, 2004. GPR 2004. Proceedings of the Tenth International Conference on.

Zheng, Y., Zhang, X., Hou, B., & Liu, G. (2014). Using combined difference image and k-means clustering for SAR image change detection. IEEE Geoscience and Remote Sensing Letters, 11(3), 691-695.